Search for Gauge Mediated Supersymmetry in the $\gamma\,\gamma\,\not\!\!E_T$ Channel

by

Stilianos Isaak Kesisoglou

B.Sc., University of Patras, Greece 1993
Sc.M., Brown University, 1997

Thesis

Submitted in partial fulfillment of the requirements for
the Degree of Doctor of Philosophy
in the Department of Physics at Brown University

Providence, Rhode Island
May 2005

Abstract of " Search for Gauge Mediated Supersymmetry in the $\gamma\,\gamma\ \not\!\!E_T$ Channel ", by Stilianos Isaak Kesisoglou, Ph.D., Brown University, May 2005.

We present results on a search for Gauge Mediated Supersymmetry in the di-photon final state using Run II data collected by the DØ Experiment at the Fermilab Tevatron Collider. We discuss event selection, Standard Model backgrounds, and the lower limits on the lightest neutralino and chargino masses resulted from this analysis.

This dissertation by Stilianos Isaak Kesisoglou is accepted in its present form by
the Department of Physics as satisfying the
dissertation requirement for the degree of
Doctor of Philosophy

Date..... .....
Greg Landsberg, Advisor

Recommended to the Graduate Council

Date..... .....
Antal Jevicki, reader

Date..... .....
Dave Cutts, reader

Approved by the Graduate Council

Date..... .....
Karen Newman
Dean of the Graduate School

The Vita of Stilianos Isaak Kesisoglou

Stilianos Isaak Kesisoglou was born on January 1^{st} 1970 in the ancient city of Athens, Greece. He graduated with B.Sc in Physics (first in his class and year) from the University of Patras in 1993. After finishing his 2 year military service he enrolled in the Brown University's Sc.M / Ph.D program were he obtained the M.Sc degree in Physics in 1997. Before moving to Fermilab to work on his Ph.D thesis, he was appointed Research Assistant (1997-1998) and Teaching Assistant (1998-1999) at the Brown University's Department of Physics.

I Preface and Acknowledgements

Traditionally, this is the place where one reflects back on the long and winding path that leads to a Ph.D. Indeed, I find that what I have achieved would certainly not have been possible without the help of many many people:

I wish to express my gratitude to my advisor Greg Landsberg for his support and guidance throughout my graduate career. Greg always gave me the freedom to pursue my interests, and was always present when I needed any advice, but most importantly was always patient and understanding during the time that personal problems send me out of course.

This analysis, though, would have never finished if not for the help and guidance of Yuri Gershtein. Not only is he an excellent physicist and teacher, but the kindest and most patient person I have met. I will always remain indebted to him for leading me to the light at the end of the tunnel. Putting up with someone like me must have been quite a challenge!

I also wish to thank all my professors at Brown University for teaching me the basics of particle physics, and especially Antal Jevicki and Dave Cutts, for serving as readers on my doctoral committee. I would like to thank Brendan Casey, Doug Chapin, Ryan Hooper and Sean Mattingly for proof-reading my thesis.

I am grateful to all my DØ collaborators at Fermilab: they designed, constructed and operated one of the best experiments in the world. I appreciated a lot the company of Petros Rapidis, Eric Kajfasz, Jim Fast, Ron Lipton, Marcel Demarteau, Gordie Gillespie, Ryan Hickey, Wayne Schmitt and other people when working on the Silicon Detector assembly.

I have been fortunate to meet many new friends, and I would like to express my gratitude to all of them. They are too numerous to list, but I would like to single out Alex Melnitchouk. The two of us shared the same path during our years at DØ, from our first visit at Fermilab to attend the Strong Dynamics Workshop, through the Silicon Detector assembly and beyond.

Perhaps my greatest gratitude goes to my family: my parents Ioannis and Marina, and my sister Xenia. Their love and support during my 18 years that I was away from home studying have been unyielding. I can only hope to give back to them as much as they have given me.

Dedication

To our parents we owe our life,

To our teachers we owe the good life

Old Greek Proverb

This work is dedicated to all of the above.

Contents

Preface and Acknowledgments **iv**

I Preface and Acknowledgements iv

Dedication **vi**

1 Introduction **1**

2 Theoretical Overview **5**

2.0.1 Local Gauge Invariance 6

2.0.2 Strong Interaction 9

2.0.3 Weak and Electroweak Interactions 10

2.0.4 Higgs and Electroweak Symmetry Breaking 11

2.0.5 The Standard Model Lagrangian 13

2.1 Extensions of the Standard Model 14

2.1.1 Supersymmetry 14

2.1.2 Gauge Mediation of Supersymmetry Breaking 16

3 Detector Description **20**

3.1 Overview of the Tevatron Collider 20

3.1.1 Cockroft-Walton pre-accelerator 21

3.1.2 The LINAC 22

3.1.3 The Booster Synchrotron 22

3.1.4 The Main Injector . . . 23
3.1.5 The Anti-proton Source . . . 23
3.1.6 The Debuncher and the Accumulator . . . 23
3.1.7 The Recycler . . . 24
3.1.8 The Tevatron Ring Synchrotron . . . 24
3.2 Overview of the DØDetector for Run II. . . . 25
3.3 Coordinate System and Other Conventions at DØ . . . 27
3.4 The DØDetector Components . . . 29
3.4.1 Tracking System . . . 30
3.4.2 Silicon Microstrip Tracker . . . 31
3.4.3 Central Fiber Tracker . . . 40
3.4.4 Central and Forward Preshower Detectors . . . 42
3.5 Calorimeter System . . . 43
3.5.1 DØCalorimeter . . . 46
3.5.2 Intercryostat and Massless Gap Detectors . . . 52
3.5.3 Luminosity and the Luminosity Monitor . . . 53
3.5.4 Muon System . . . 55
3.6 Forward Proton Detector . . . 58
3.7 Trigger and Data Acquisition Systems (DAQ) . . . 60
3.7.1 DØLevel 1 Trigger . . . 62
3.7.2 DØLevel 2 Trigger . . . 63
3.7.3 DØLevel 3 Trigger and DAQ . . . 64

4 Reconstruction and Particle ID **66**

4.1 Showers . . . 66
4.1.1 Electromagnetic Showers . . . 66
4.1.2 Hadronic Showers . . . 71
4.2 EM Reconstruction and Identification . . . 71

4.2.1 Electromagnetic Isolation . . . 73
4.2.2 Electromagnetic Fraction . . . 75
4.2.3 H-Matrix Variable . . . 76
4.2.4 Track Match and Track Veto . . . 77
4.2.5 EM Energy Scale . . . 78
4.2.6 Photon Pointing . . . 79
4.3 Jet Reconstruction . . . 86
4.4 Track and Vertex Reconstruction . . . 90
4.5 Missing Energy - $\not\!\!E_T$ . . . 92
4.5.1 $\not\!\!E_T$ Significance . . . 93

5 Data Sample Selection **96**
5.1 Trigger Requirements . . . 96
5.2 Luminosity Calculation . . . 99
5.3 Offline Event Selection . . . 100
5.3.1 Electromagnetic Objects . . . 100
5.3.2 Jets and $\not\!\!E_T$ . . . 109

6 Signal Generation **110**
6.1 Event Generation and Simulation . . . 110
6.1.1 Event Generation . . . 111
6.1.2 Detector Response Simulation . . . 111
6.1.3 Reconstruction and Trigger Simulation . . . 112
6.2 Generated Monte Carlo . . . 113
6.2.1 Signal Efficiency . . . 113

7 Standard Model Backgrounds **116**
7.1 Di-photon Events . . . 119
7.2 QCD Background Events . . . 122

7.3 Electoweak Background Events 123

8 Optimization and Limits **128**

8.1 Cut Optimization 128

8.2 Limits Setting 130

8.2.1 Bayes' Theorem 131

8.2.2 Limits Calculation 132

9 Conclusions **137**

List of Tables

3.1 The depth of the calorimeter layers. 48

4.1 Geometry and average resolutions in the central region for the Preshower detectors and the EM calorimeter floors for Run II, compared to Run I (inside parenthesis). . 86

5.1 Event yields, statistical and systematic errors for events with exactly one (N1) and two (N2) track matches. 101

6.1 Points on the GMSB model slopes: their cross-sections, efficiencies and cross-section limits. All points correspond to $\mu > 0$. Points 8-14 correspond to the Snowmass model line E. 114

7.1 The event counts in the $\gamma\gamma$, $e\gamma$ and QCD samples, and determination of the total background to diphoton sample. 120

List of Figures

2.1 The Standard Model. 7

2.2 An example of a decay mode. 19

3.1 Schematics of the Run II Fermilab accelerator complex. 21

3.2 3D view of the DØDetector. 26

3.3 View of the DØcoordinates. 27

3.4 Distribution of the interactions point's z-axis position. 28

3.5 The $r - z$ view of the DØDetector. 30

3.6 DØtracking system (the quadrant $r - z$ view) (Adapted from [25]). 31

3.7 The SMT design structure. 32

3.8 Displased vertex originating from b or c quarks. 33

3.9 Illustration of a 3-chip ladder. Features measured with OGP probe are four Be structures (AB, C, D EF) and six fiducials on the sensor surface (1-6). 34

3.10 The $x - y$ view of the bulkhead. 35

3.11 A bulkhead with two ladders installed. 35

3.12 Placement of the Be support structures with respect to the ladder plane at the measured point AB of 3.9, for a set of installed 3-chip ladders. Ladder plane is defined by the six points (1-6) shown in 3.9. 37

3.13 Slope of the sensor plane for free (magenta) vs. mounted (cyan) optical measurements for a set of 3-chip ladders. Be support structures on the two sides of the ladder are shown as points (red-blue). 37

3.14 Measured fiducials (green) and points (red-blue) on the surface of a 9-chip sensor. Active sensor is the one on which later will be attached the HDI with the SVXII readout chips. 38
3.15 Profile of a measured set of points (red-blue) on the Be support structure surface. The slope of the 3-chip sensor is shown in magenta. 39
3.16 3D Flatness profile of a 6-chip ladder. Various measured features are shown as sensor points (red-blue), fiducials (green) and Be support structures (magenta). 39
3.17 a) Position resolution distribution measured in the CFT cosmic ray test stand. b) End view of the interlocking doublet ribbon configuration. 41
3.18 The $r-z$ view of the scintillating fiber tracker with the end view of the fibers. . . . 42
3.19 $x-y$ and $r-z$ views of the Central Preshower Detector. 43
3.20 Location of Forward Preshower Detector in the DØDetector 44
3.21 DØCalorimeter. 47
3.22 Pseudo-projective geometry of the DØCalorimeter. 49
3.23 Calorimeter unit cell. 50
3.24 Simplified calorimeter data flow diagram. 50
3.25 Full calorimeter data flow diagram. 51
3.26 Segmentation of the DØcalorimeter towers in terms of depth and η. 52
3.27 DØLuminosity Monitor. 54
3.28 Collider Integrated Luminosity delivered to DØin Run II [49]. 55
3.29 DØmuon detection system. 57
3.30 Shown here is the $\rho-\phi$ view of one plane of the MDT's. The insert shows the cross section of a single Iarocci tube 58
3.31 An $\rho-\phi$ view of the scintillator pixel counters. 59
3.32 DØtrigger scheme layout and typical trigger rates. 61
3.33 The L1 and L2 trigger data flow path. 62
3.34 The L2 configuration. 63

3.35 The L3/DAQ system layout. 64

4.1 Fractional energy loss per radiation length in lead as a function of the electron or positron energy. At high energies bremsstrahlung dominates. 68

4.2 Total photon cross sections as a function of energy in carbon and lead, showing contributions of different processes. At high energies pair production dominates ($\mathcal{K}_{nuc}$ and $\mathcal{K}_e$ denote pair production in nuclear and electron fields, respectively). 69

4.3 30 GeV electron cascade induced in iron (EGS4 simulation). The histogram shows fractional energy deposition per radiation length, and the curve is a gamma-function fit to the distribution. Circles indicate the number of electrons with total energy greater than 1.5 MeV crossing planes at $X_0/2$ intervals (scale on the right) and the squares are the number of photons with $E \geq 1.5$ MeV crossing the planes (scaled down to have the same area as the electron distribution). 70

4.4 Shower simulation with DØGSTAR of particles with $p_T = 50$ GeV. Particles simulated include γ, e^-, μ^+, π^+, K_L^0, K_S^0, n^0, $\overline{p}$. 72

4.5 Cluster reconstruction windows in $\eta - \phi$. 74

4.6 Representation of the EM object reconstruction cones. 74

4.7 Representation of total (E_{total}), hadronic ($FH1$), and electromagnetic energy (EM) of a cluster used for the determination of the electromagnetic energy fraction (EM_{fract}). 76

4.8 Pointing and non-pointing photons in shower simulation with DØGSTAR. 81

4.9 Residuals in the $r - z$ plane versus z for the Central Calorimeter. 83

4.10 Residuals in the $r - \phi$ plane versus z for the Central Calorimeter. 83

4.11 Profile of the residuals in the $r - z$ plane versus z for the Central Calorimeter. . . . 84

4.12 Profile of the residuals in the $r - z$ plane versus z for the Central Calorimeter. . . . 85

4.13 Pointing resolutions for the $r - z$ and $r - \phi$ planes for the Central Calorimeter for Monte Carlo. 87

4.14 Pointing resolutions for the $r - z$ and $r - \phi$ planes for the Central Calorimeter for Data. 88

4.15 χ^2 probability for the fits in $r - z$ and $r - \phi$ planes for the Central Calorimeter. . . 89

4.16 Example of $p\left(\not\!\!E_T; \vec{\alpha}\right)$ in two events with large $\not\!\!E_T$. 95

5.1 DiEM mass spectra for the events with exactly one (left) and exactly two EM clusters with track match. 102

5.2 Efficiency for H-matrix cut $\chi^2 < 15$ for $Z \to e^-e^+$ events in Data (red) and in MC (blue) vs. the number of JCCB jets in the event. 103

5.3 Efficiency for H-matrix cut $\chi^2 < 15$ for $Z \to e^-e^+$ events in Data (red) and in MC (blue) vs. the distance $\Delta R = \sqrt{\Delta\phi^2 + \Delta\eta^2}$ to the closest JCCB jet in the event. . . 104

5.4 Ratio of Data to MC efficiency for H-matrix cut $\chi^2 < 15$ for $Z \to e^-e^+$ events vs. the number of JCCB jets in the event. 104

5.5 Ratio of Data to MC efficiency for H-matrix cut $\chi^2 < 15$ for $Z \to e^-e^+$ events vs. the distance $\Delta R = \sqrt{\Delta\phi^2 + \Delta\eta^2}$ to the closest JCCB jet in the event. 105

5.6 Ratio of Data to MC efficiency for H-matrix cut $\chi^2 < 10$ for $Z \to e^-e^+$ events vs. the number of JCCB jets in the event. 105

5.7 Ratio of Data to MC efficiency for H-matrix cut $\chi^2 < 10$ for $Z \to e^-e^+$ events vs. the distance $\Delta R = \sqrt{\Delta\phi^2 + \Delta\eta^2}$ to the closest JCCB jet in the event. 106

5.8 Track isolation efficiency for $Z \to e^-e^+$ events in Data (red) and in MC (blue) vs. the number of JCCB jets in the event. 107

5.9 Track isolation efficiency for $Z \to e^-e^+$ events in Data (red) and in MC (blue) vs. the distance $\Delta R = \sqrt{\Delta\phi^2 + \Delta\eta^2}$ to the closest JCCB jet in the event. 107

5.10 Ratio of Data to MC efficiency for H-matrix cut $\chi^2 < 15$ and track isolation cut for $Z \to e^-e^+$ events vs. the number of JCCB jets in the event. 108

5.11 Ratio of Data to MC efficiency for H-matrix cut $\chi^2 < 15$ and track isolation cut for $Z \to e^-e^+$ events vs. the distance $\Delta R = \sqrt{\Delta\phi^2 + \Delta\eta^2}$ to the closest JCCB jet in the event. 108

7.1 Photon E_T for model point close to the exclusion limit obtained in the analysis ($\Lambda = 0.8 \cdot 10^5$, $M_5 = 0.16 \cdot 10^6$, $N_5 = 1$, $tan\beta = 5.0$, $\mu > 0$). 117

7.2 Azimuthal opening angle between the direction of $\not\!\!E_T$ and the leading jet for events with $\not\!\!E_T > 25$ GeV and $\not\!\!E_T > 35$ GeV (QCD sample). 120

7.3 $\not\!\!E_T$ distribution in the diphoton sample after all cuts (points). Red histogram is QCD background, blue histogram is the total estimated background. Purple histrogram shows ten times the contribution expected from the SUSY point #13 of Table 6.1. . 121

7.4 $\not\!\!E_T$ distribution in the electron-photon sample after all cuts (points). 124

7.5 $\not\!\!E_T$ distribution in the electron plus EM object sample after all cuts (points). 126

7.6 Probability for a jet reconstructed as an EM object to pass photon ID cuts for events passing single EM (triangles), tight di-EM (squares) and loose di-EM (circles) triggers.127

8.1 Expected limit on Λ vs. cut on $\not\!\!E_T$. 130

8.2 Snowmass model line E cross section vs. Λ in LO (blue solid line), multiplied by K-factor (blue dashed line) and the 95% C.L. limits (brown solid line). 134

8.3 GMSB SUSY cross section vs. Λ in LO (blue solid line), multiplied by K-factor (blue dashed line) and the 95% C.L. limits (brown solid line). 135

8.4 GMSB SUSY cross section vs. Λ in LO (blue solid line), multiplied by K-factor (blue dashed line) and the 95% C.L. limits (brown solid line). 136

Chapter 1

Introduction

Symmetry, however we define it's meaning, is a concept that throughout the centuries has been used by humans as a means to explore and understand the world. This effort is evident in the full range of human activities, art, music, science and theology. The influence of symmetry in every aspect of life is not accidental; nature itself exhibits symmetry from inorganic objects to the organic kingdom and from small to grand scale. It is only natural, therefore, that from the birth of Physics as science, symmetry played and continues to play a vital role in its development. In mechanics, the principle of relativity for the inertial frames imposed by Galileo, and the acceptance of the Euler-Lagrange and Hamilton's formalisms were both influenced by it. In electromagnetism, the invariance of the field under gauge transformations was an important tool for both the theoretical treatment and for practical considerations. But it wasn't until the beginning of the last century, after the development of the mathematical framework behind symmetries, that physicists started to take notice of the concept when it was revealed that symmetry can literally define the form of the equations we construct to describe physical phenomena. The best known example that demonstrates this far reaching power of symmetry is a theory proposed by Albert Einstein called Special Relativity. This theory is based essentially upon a single symmetry argument, that of Galileo's principle of relativity, as it was enlarged by Einstein, to include not only the laws of mechanics but every law of nature. This new theory not only proved very successful in explaining new phenomena, but also

shed new light on some already known properties of the "old" physics. Newton's and Langrange's alternative descriptions of the force (based on the change respect to time or space respectively) were understood. The apparent "asymmetry" of the electromagnetic equations observed by Maxwell was also understood, leading also to the first known example of force unification (electricity and magnetism). At about the same time, the emergence of a new description of the physical world, named Quantum Mechanics, required a completely different mathematical formulation (Hamilton's formulation). This formulation was, for the most part, already in place, gaining acceptance despite its non-empirical content simply because of its symmetric form. The following years (1930 and later) saw an explosive usage of symmetry in all branches and applications of Physics (Solid State and Quantum Physics are among the first) but most importantly in the emerging area of Particle (High Energy) Physics. In the first attempts at formulating a relativistic quantum theory, the importance of Lorentz invariance was demonstrated in classifying physical particles based on their mass and spin. The realization that gauge invariance is not just accidental, but is the heart of the electromagnetic theory, lead gradually to the acceptance that it must be at the heart of every known interaction. To explain and classify the new experimental data, new symmetries were proposed and a consistent framework of describing the reality had emerged. The Standard Model (SM) of electroweak and strong interactions developed in the 1960s by Glashow, Salam, and Weinberg [1], serves as our current model for the interactions between particles of the physical world down to the distances $\sim 10^{-16}$ cm. The discovery of the W and Z bosons in 1983 by the UA1 and UA2 collaborations [2, 3, 4] at the CERN $p\bar{p}$-collider and the discovery in 1995 of the the top quark by the CDF and DØ collaborations at the Tevatron $p\bar{p}$-collider at Fermilab [5, 6] are examples of important experimental confirmation of the Standard Model predictions. Although the SM agrees with experimental measurements to a very high degree, there are several theoretical problems which cannot be solved without introduction of new physics. One key aspect for the completeness of the Standard Model is the introduction of a scalar field called the Higgs field. Although this field is essential for explaining of the origin of mass, it has some implications which are very difficult to deal with. When trying to calculate its mass, quadratically divergent terms appear. In addition, the inclusion of gravity into the same

unifying framework with the other three interactions seems to be very difficult. The above problems are two of the driving motivations behind the introduction of yet another form of symmetry into our understanding of nature called Supersymmetry. This is a symmetry which relates particles of different spin; a symmetry that is proven to suppress the quadratic growth of the Higgs boson mass (in every perturbation order), and that provides a vehicle for incorporating gravity into a single framework. But the inclusion of this new "enlarged" symmetry doesn't come without a cost; as it leads to a prediction of doubling the number of all known particles, something that clearly is not supported by experimental data thus far. It is clear then that this must be a broken symmetry, and although the mechanism of supersymmetry breaking is not well understood, some theoretical models have been proposed over the years. Gauge Mediated supersymmetry breaking is one of these models. Since none of the above hypotheses has been confirmed or ruled out yet, an experimental search for the existence of supersymmetry via its resulting signatures is very important.

On a personal level, my interest in symmetries in Physics started during my years in the high school. It was at that time, that I first came in contact with the theory of Special Relativity. What I can still remember is how beautiful it seemed, a theory based on two simple axioms: that all observers are equivalent in describing the physical world, and that all physical phenomena are equivalent; nature doesn't hold some of them in higher regard than it does the others. Over the years, I was exposed not only to the above mentioned evolutions in Physics, but also to evolutions in Mathematics and Music. I was always fascinated by the fact that some of the most important contributions in these fields were just the recognition of an underlying hidden symmetry. When this symmetry came up to light, things looked much more connected and clear. It was only natural for me to focus my attention on the subject of symmetries in Physics, a topic that I chose for my Bachelor thesis and of course, my Ph.D thesis. I believe that symmetries hold the key to understanding how nature works, because they have an invaluable property: they reduce the number of free parameters without eliminating them. Nature's appearance is complex but we desire simple fundamental descriptions. So, what we are looking for in Physics, is a tool to allow us to reduce theoretical complexity while at the same time preserving the observed complexity. Symmetries have been proven in the past

to do exactly that. It is my belief that if we use them correctly, we can eventually reduce all the fundamental complexity to nothing, leaving only structure, but no parameters. In order to do that, we have to correctly understand the real symmetries involved, and not some "symmetries" which are simply results of our imagination. This is a difficult task, and it's precisely the combination of those two challenges that draws my interest to the subject.

The work described in this dissertation is a contribution to the search for supersymmetry signatures performed with the DØ detector in Run II of the Fermilab Tevatron. The dissertation contains eight additional chapters. Chapter 2 gives an overview of the Standard Model and its Supersymmetric extensions. Chapter 3 provides a short description of the Fermilab Tevatron proton-antiproton collider and the DØ detector which was used to collect data for this analysis. Chapter 4 describes the methods used in DØ for reconstructing and identifying physics objects constructed from data collected by the detector. Chapter 5 explains specifics of the event selection, as well as efficiencies for object reconstruction. Chapter 6 contains the a brief description of the Monte Carlo generators used for this analysis along with a description of the generated signal. Chapter 7 deals with the specific backgrounds that enter this analysis along with their estimation. Finally Chapter 8 discusses the optimization of the cuts used in this analysis, and since no evidence for new physics was found, limits are set on the masses of the lightest particles in the class of model under study.

Chapter 2

Theoretical Overview

A number of theoretical insights along with experimental discoveries over the last century have significantly advanced our understanding of elementary particles in nature and their interactions. A theory relating electroweak and strong interactions (but not gravity), called "The Standard Model" (SM) has become the prototype for particle physics. A wealth of experimental data collected around the world has tested the model with precision measurements. All the data collected so far satisfy SM predictions with a high degree of accuracy.

A complete review of the Standard Model and it's proposed extensions is beyond the scope of this thesis. Here only a brief overview of the model will be made, followed by the presentation of one of its extensions, the supersymmetric model.

The Standard Model (SM) incorporates strong and electroweak interactions of elementary particles. Currently it doesn't incorporate gravity, which at large scale is described by the theory of General Relativity. It is a Quantum Field Theory (incorporates the requirements of the theory of Special Relativity along with Quantum Mechanics), and its equations are obtained based on the principle of least action and local gauge symmetry [7, 8]. The local gauge invariance imposed by the theory is described mathematically by the group $SU(3)_C \otimes SU(2)_L \otimes U(1)_Y$. In the above combined group, $SU(3)_C$ is the underlying symmetry group of the strong (color) interactions, collectively described by the theory of Quantum Chromodynamics (QCD). The $SU(2)_L \otimes U(1)_Y$ part represents

the underlying symmetry group describing the unified weak and electromagnetic interactions. In this model (as with any Quantum Field Theory) particles are described as field excitations above the ground state (vacuum), and they are classified in two main groups: a) fundamental massive fermions with intrinsic spin 1/2 and b) gauge vector bosons with intrinsic spin of 1 or 0. The fermions are further divided into quarks (colored particles) and leptons (non-colored). The particles are arranged into families and generations with similar properties and increasing mass. According to the model there is no prediction of how many generations of fermions exist; so far only three generations have been observed. The gauge bosons are further divided into eight massless gluons which mediate strong interaction, three massive bosons mediating weak interaction, and massless photon that mediates electromagnetic interaction. Figure 2.1 illustrates the model of elementary particles. In the next few sections some of the aspects of the SM will be discussed in more detail.

2.0.1 Local Gauge Invariance

The origins of local gauge invariance can be traced back in electromagnetism, where even in Maxwell's time it was known that in Maxwell's equations the transformation of the field potential $A_\mu \rightarrow A_\mu + \partial_\mu \lambda(x)$ (gauge transformation) left unchanged not only the electromagnetic field itself but also the interaction of the charged particles with the field. The last property could be traced (using Noether's theorem) to the conservation of electric charge:

$$\partial_\mu j^\mu = 0 \tag{2.1}$$

This connection between a conserved physical quantity and the form of the underlying equations under gauge transformation lead to some very important results when attempting to describe the electromagnetic field and its interaction with charged particles at the quantum level. It uniquely determines both the form of the Lagrangian and the transformation properties of the wave function describing charged particles. If a gauge transformation is to be applied (and we know that it can be done since the charge is conserved) the Lagrangian that describes a charged particle interacting

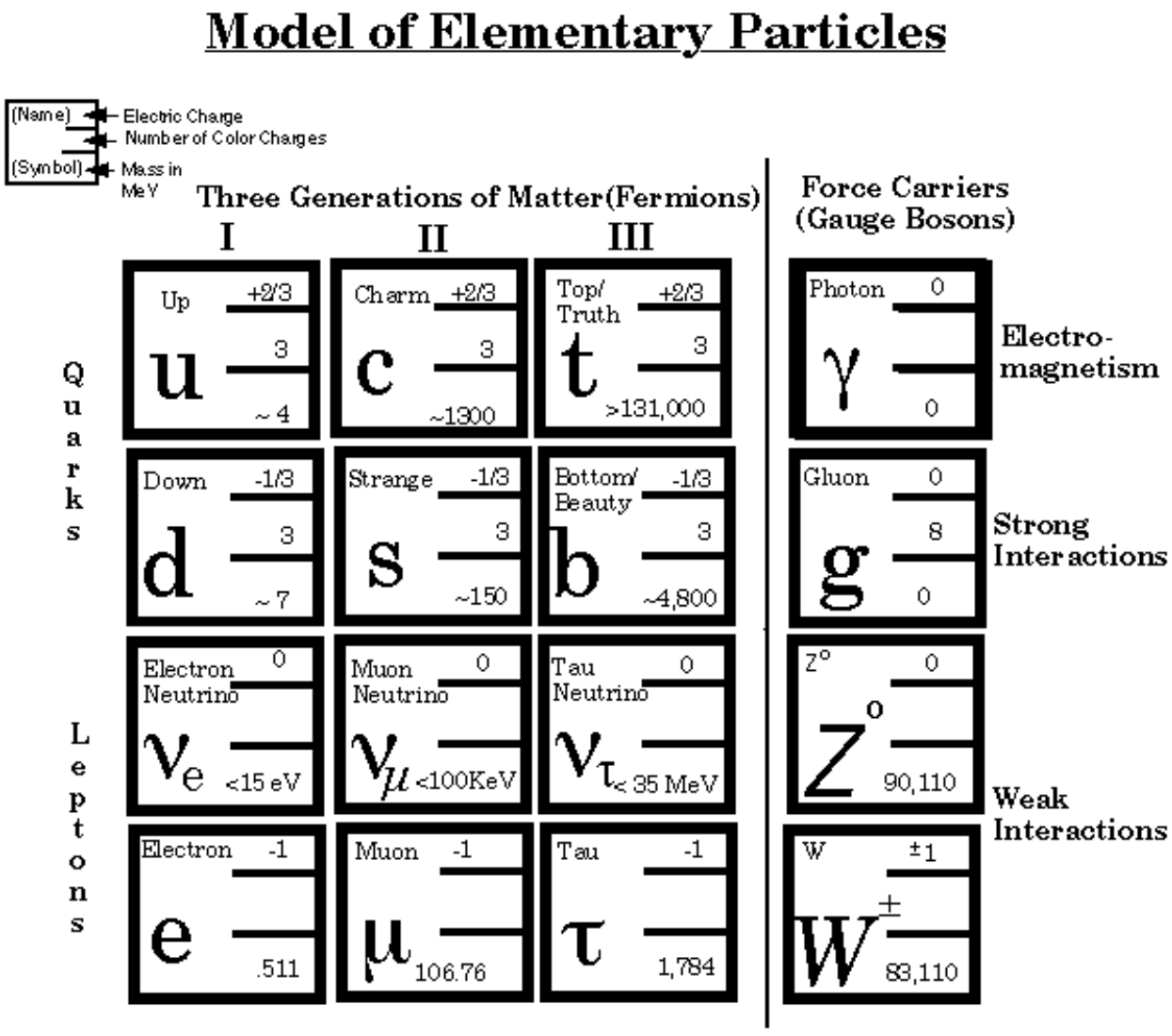

Figure 2.1: The Standard Model.

with the field has to have the form:

$$\mathcal{L} = i\bar{\psi}\gamma^{\mu}\partial_{\mu}\psi - m\bar{\psi}\psi - (q\bar{\psi}\gamma^{\mu}\psi)A_{\mu} \,, \tag{2.2}$$

while the wave function of the charged particle has to transform under the U(1) gauge transformation:

$$\psi \rightarrow e^{-iq\lambda(x)}\psi \,. \tag{2.3}$$

The above transformation of the wave function can be experimentally tested (Bohm-Aharonov effect) for the electromagnetic field, which leads to the conclusion that the field A_{μ} is a real physical quantity. As such it has to have a gauge-invariant term in the Lagrangian, and the only available form comes from the EM field itself:

$$F_{\mu\nu} = \partial_{\mu}j_{\nu} - \partial_{\nu}j_{\mu} \,. \tag{2.4}$$

This leads to the full Lagrangian for the interaction between charged particles and electromagnetic field:

$$\mathcal{L}_{QED} = i\bar{\psi}\gamma^{\mu}\partial_{\mu}\psi - m\bar{\psi}\psi - (q\bar{\psi}\gamma^{\mu}\psi)A_{\mu} - \frac{1}{4}F_{\mu\nu}F^{\mu\nu} \,. \tag{2.5}$$

From the above it's clear that by imposing local gauge invariance in the wave function we almost uniquely determine the form of the interaction, plus we extract a conserved physical quantity, the above three characteristics going together as a triangle. It was this property that lead to the acceptance of the local gauge invariance as a key tool in modeling then unknown strong and weak forces. Gauge transformations form mathematical groups and by choosing a particular gauge group, we can make a model for a specific type of interaction. For example, by requiring the transformation group SU(2) for the fermion doublet, the local gauge invariance requires three massless vector bosons; the mediators of the weak force.

2.0.2 Strong Interaction

Strong interaction is essentially modeled in the above scenario of local gauge invariance. The descriptive model of the strong interactions, called Quantum Chromodynamics (QCD), is a gauge field theory based on the $SU(3)_C$ mathematical group (C stands for color). In this model the particles influenced by this force (quarks and gluons) are characterized by a new internal "charge", called color, which is the origin of strong force and which appears in three different varieties usually named red, green, and blue. A quark of a specific type (such as a strange quark) therefore can come in three colors. The development of the model closely resembles the one of QED, in this case assuming that the Lagrangian is invariant under the local $SU(3)$ gauge transformation:

$$\psi \rightarrow e^{-iT^{\alpha}\lambda_{\alpha}(x)}\psi \,, \tag{2.6}$$

where T^{α} is a set of operators forming a representation of the $SU(3)$ group. As with the case of electromagnetism, this requirement leads to the introduction of eight gauge fields (the mediators or carriers of the force) A^{α}_{μ} transforming as:

$$A^{\alpha}_{\mu} \rightarrow A^{\alpha}_{\mu} + \partial_{\mu}\lambda^{\alpha}(x) - f_{\alpha\beta\gamma}\lambda^{\beta}(x)A^{\gamma}_{\mu} \,. \tag{2.7}$$

In the above expression, $f_{\alpha\beta\gamma}$ are the structure constants of the $SU(3)$ group, originating from it's non-Abelian nature. Again as in the case of the electromagnetic field the gauge fields A^{α}_{μ} give rise to the gauge-invariant fields:

$$F^{(a)}_{\mu\nu} = \partial_{\mu}A^{a}_{\nu} - \partial_{\nu}A^{a}_{\mu} - g_s f_{abc}A^{b}_{\mu}A^{c}_{\nu} \,, \tag{2.8}$$

where g_s is the QCD coupling constant. The presence of the terms $-f_{\alpha\beta\gamma}\lambda^{\beta}(x)A^{\gamma}_{\mu}$ and $g_s f_{abc}A^{b}_{\mu}A^{c}_{\nu}$ in the above expressions has a profound effect on the behavior of strong interaction, since they correspond to the gluon self-interactions. Including the above term, the full Lagrangian for the

interaction between colored particles and gauge fields is obtained:

$$\begin{aligned}\mathcal{L}_{\mathcal{QCD}} &= -\frac{1}{4}F^{(a)}_{\mu\nu}F^{(a)\mu\nu} \\ &+ i\sum_q \bar{\psi}^i_q \gamma^\mu (D_\mu)_{ij}\psi^j_q \\ &- \sum_q m_q \bar{\psi}^i_q \psi_{qi}\,, \end{aligned} \tag{2.9}$$

where

$$(D_\mu)_{ij} = \delta_{ij}\partial_\mu + ig_s \sum_a \frac{\lambda^a_{i,j}}{2} A^a_\mu\,. \tag{2.10}$$

2.0.3 Weak and Electroweak Interactions

The historical development of a theory describing the weak interactions (and the more complete electroweak form) followed a more complicated road than the one for the strong force. Initially for the interpretation of the weak force, Enrico Fermi introduced a theory based on the interaction of "weak" currents, an analog taken from the interaction of electromagnetic currents. This initial theory evolved by incorporating the observance of parity violation by Lee and Yang in 1956 (V-A theory of charged weak currents). Later, in 1963, Cabibbo introduced the idea of mixing between the d and s quarks (Cabibbo's mixing angle θ_C) to explain the weak decay of the strange particles, and to complete his hypothesis Glashow, Illiopoulos and Maiani (GIM) proposed the existence of a new quark (c or charm quark), expanding the hadronic sector. Further expansion of the Cabibbo-GIM model with the introduction of the t and b quarks, (and the generalization of the Cabibbo's mixing angle with the Kobayashi-Maskawa matrix), along with the detection of weak neutral currents in 1973 brought the model of weak forces to relative completion. But this picture of weak interactions was only satisfactory at a superficial level. Theory described reality well only when lowest-order terms were considered (small momentum exchange). For calculations of anything other than the lowest-order low-energy amplitudes, very serious problems emerged. Therefore for many years the current-current interaction was regarded merely as a phenomenological description rather than a

proper theory. Gauge invariant character for example, of the electromagnetic and strong interactions, that was used to determine the form of those interactions, was absent in this model of the weak interaction and a necessary step in this direction had to be done. Working along this line of thought, Glashow in 1961 introduced a model designed to arrange the charged weak currents in an $SU(2)$ symmetry structure. His model had far-reaching implications than not only provided a symmetry structure for the weak forces, it also predicted the existence of a greater symmetry modeled upon the group $SU(2)_L \otimes U(1)_Y$. This new "enlarged" group incorporated the charged weak currents and the weak neutral currents (discovered later) as well as the electromagnetic currents, providing at least from an aesthetic viewpoint a unification of the two interactions.

2.0.4 Higgs and Electroweak Symmetry Breaking

Although the above model of the electroweak interactions was a great step forward is understanding of weak and electromagnetic forces, it had a serious inherent problem. It predicted that the gauge fields have no mass; in fact there is no way to add externally a term for the mass of the fields. This property posses no problem for the electromagnetic force, since it's mediator (photon) has no mass, but it's a serious problem for the weak force since we know that its mediators must be massive due to the limited range of the force. Giving masses to the mediator fields by hand fails, since severe divergencies appear in every order with no way to suppress them without adding an infinite number of external parameters. Therefore, since the gauge invariance forbids the existence of massive fields in the fundamental Lagrangian, masses for these fields must be generated dynamically, through a mechanism that respects the gauge invariant character of the Lagrangian, but assigns masses to the observable particles by breaking the underlying symmetry in the observable sector. A proposed mechanism for doing that (inspired by the field of solid state physics) is by incorporating into the theory an extra spin 0 complex doublet, the Higgs field [9]:

$$\phi \equiv \begin{pmatrix} \phi^+ \\ \\ \phi^0 \end{pmatrix} .$$

The field is something that is put into the theory by hand. It's neither a matter field nor a gauge-mediator field and it's sole purpose it's to generate the appropriate mass terms in the perturbative form of the Lagrangian (i.e when we calculate excitations above the ground state). The Lagrangian of the Higgs field (using $c \equiv 1$, $\hbar \equiv 1$),

$$\mathcal{L} = (\partial_\mu \phi)^\dagger (\partial^\mu \phi) - \mu^2 \phi^\dagger \phi - \lambda (\phi^\dagger \phi)^2 \,, \tag{2.11}$$

respects local gauge invariance and so does the complete set of its ground states. However, during the perturbative approach where a particular ground state is chosen and the fields are rewritten in terms of v and H, v being the vacuum expectation value (vev) of the Higgs field and H the real field with zero vev [10], the Higgs field becomes

$$\phi \equiv \begin{pmatrix} \phi^+ \\ \phi^0 \end{pmatrix} \rightarrow \frac{1}{\sqrt{2}} \begin{pmatrix} 0 \\ v + H \end{pmatrix}$$

and breaks the $SU(2)_L \otimes U(1)_Y$ symmetry. It has to be noted here that this breaking happens only on the surface. The nature of the theory remains unchanged; it still possess the local gauge invariant property in the fundamental level, but the specific solutions chosen above the ground state do not posses this property. This symmetry breaking leads to an extra three degrees of freedom that correspond to the zero-energy excitations along the ground state surface of the unbroken theory. Because of the local character of the symmetry these extra degrees of freedom appear as additional (longitudinal) polarizations of the original W^i_μ bosons, i.e. weak gauge bosons acquire mass. One interesting result of the Higgs mechanism is that it not only explains the mass of $W^\pm$ and Z^0 bosons, but also the fermion masses and predicts a weakly interacting spin-0 massive particle – the Higgs boson. Parameters v, μ and λ of the Higgs field are related via $v^2 = \frac{-\mu 2}{\lambda}$ [11]. The parameter v can be expressed in terms of the Fermi coupling constant (which is determined in muon lifetime measurements) [10]:

$$v = \left(\sqrt{2} G_F\right)^{-1/2} = 246\,\text{GeV} \,. \tag{2.12}$$

This leaves a single independent parameter, which can not be determined indirectly without having experimental information about the Higgs boson. This unknown parameter can be rewritten as the Higgs boson mass $m_H = \sqrt{-2\mu^2}$.

2.0.5 The Standard Model Lagrangian

Incorporating the strong and electroweak interactions into a single framework produces the final Standard Model Lagrangian. We already have seen the part for the strong interaction (QCD):

$$\begin{aligned} \mathcal{L}_{\mathcal{QCD}} &= -\frac{1}{4}F^{(a)}_{\mu\nu}F^{(a)\mu\nu} \\ &+ i\sum_q \bar{\psi}^i_q \gamma^\mu (D_\mu)_{ij}\psi^j_q \\ &- \sum_q m_q \bar{\psi}^i_q \psi_{qi}\,. \end{aligned} \tag{2.13}$$

After the above analysis of the electroweak interactions the relevant part is (before the symmetry is spontaneously broken):

$$\begin{aligned} \mathcal{L}_{\mathcal{EW}} &= -\frac{1}{4}W_{\mu\nu}\cdot W^{\mu\nu} - \frac{1}{4}B_{\mu\nu}B^{\mu\nu} \\ &+ \overline{L}\gamma^\mu\left(i\partial_\mu - g\frac{1}{2}\tau\cdot W_\mu - g'\frac{Y}{2}B_\mu\right)L \\ &+ \overline{R}\gamma^\mu\left(i\partial_\mu - g'\frac{Y}{2}B_\mu\right)R \\ &+ \left|\left(i\partial_\mu - g\frac{1}{2}\tau\cdot W_\mu - g'\frac{Y}{2}B_\mu\right)\phi\right|^2 - V(\phi) \\ &- \left(G_1\overline{L}\phi R + G_2\overline{L}\phi_c R + hermitian\,conjugate\right)\,, \end{aligned} \tag{2.14}$$

where L denotes a left-handed fermion (lepton or quark) doublet, and R denotes a right-handed fermion singlet. In the above electroweak Lagrangian the first line describes the $W^\pm, Z$ and γ kinetic energies and self-interactions, the second and third lines are the lepton and quark kinetic energies and their interactions with $W^\pm, Z, \gamma$, the fourth line describes the $W^\pm, Z, \gamma$ and Higgs masses and couplings, and the last line describes the lepton and quark masses and couplings to the Higgs field.

2.1 Extensions of the Standard Model

Although more crucial tests remain to be done, the above described theory (Weinberg-Salam model) is widely believed to be an accurate description of matter and interactions. All matter is composed from spin-1/2 particles (quarks and leptons) whose interactions are a consequence of exact local gauge symmetries. The gauge fields mediating these color (gluons), and electroweak (photon and W, Z) interactions have spin 1 (bosons). Through spontaneous symmetry breaking, the weak bosons and the fermions acquire mass and the theory remains "renormalizable" (i.e only tuning of the parameters is needed to avoid divergencies and not the addition of new parameters). But beyond the successes of the above model many things still remain uncertain, requiring a new step to go beyond the current knowledge. The possible unification of the gauge fields leads us to the question if there is a principle that relates matter fields with gauge fields so that they can be unified too. Also the exclusion of gravity from our current understanding leads us to believe that there must be a more fundamental description of nature, one that encompasses all the above. There are two main approaches to these questions. The first idea is to start with gravity, a well understood force classically originating from the curvature of the four-dimensional spacetime and ask what is the corresponding geometry associated with color, electromagnetism etc. The other approach starts with Grand Unified Theories (GUT's) and attempts to incorporate gravity into the scheme. One of these approaches to GUT is to directly link the matter fields (spin-1/2 Dirac fields) with the gauge fields (spin-1 boson fields) through a symmetry. Such a symmetry is necessarily very different from any symmetry previously encountered and as such is called "supersymmetry".

2.1.1 Supersymmetry

Supersymmetry is a symmetry that connects particles of different spin, with all other characteristics like mass, charge etc. being the same [12]. The particles are combined into a "superfield" which contains fields differing by one-half unit of spin [13]. The strongest theoretical motivation for supersymmetry is that it offers hope for solving the hierarchy problem. The Standard Model is today usually understood as a low-energy approximation to an unknown fundamental theory in

which all interactions appear unified at an energy somewhere in the range of 10^{12} to 10^{18} GeV. This raises the hierarchy problem: what accounts for the enormous ratio of this fundamental energy scale and the energy scale ≈ 200 GeV that characterizes the standard model? Fermions and gauge bosons are required by the $SU(3)_C \otimes SU(2)_L \otimes U(1)_Y$ gauge symmetry to appear with zero mass in the Lagrangian of the Standard Model. As a result, the physical masses of these particles are proportional to the electroweak braking scale, which in turn is proportional to the mass of the scalar fields responsible for the electroweak symmetry breaking. But here lies a problem: the scalar fields themselves are not bounded from acquiring large bare masses, so there is no logical argument why they cannot be in the neighborhood of 10^{12} to 10^{18} GeV. It has been hoped that this problem could be solved by embedding the standard model into a supersymmetric theory. If the scalar fields appear in super-multiplets along with the known particles in a representation of some gauge group, then the problem is solved since that will require zero bare masses for the scalars along with the fermions. In this case all the masses of the standard model would be tied to the energy scale at which supersymmetry is broken.

Another motivation for supersymmetry is that it provides a mean for canceling the quadratically divergent contribution to the Higgs boson mass in perturbation theory. For example suppose we consider the one loop contributions to the Higgs boson mass in a theory which contains both massive scalars, ϕ, and fermions, ψ in addition to the Higgs field h. For this type of theory the Lagrangian is given by:

$$\mathcal{L} \sim g_F \bar{\psi}\psi h - g_S^2 h^2 \phi^2 \,, \tag{2.15}$$

Calculating the one-loop contribution to M_h^2 yields

$$M_h^2 \sim M_{h0}^2 + \frac{g_F^2}{4\pi^2}(\Lambda^2 + m_F^2) - \frac{g_S^2}{4\pi^2}(\Lambda^2 + m_S^2) + \text{log. divergences} + \text{other terms.} \tag{2.16}$$

where Λ is a dimensioned parameter with units of mass that determines the effective scale of SUSY breaking.

We can see from the above that if $g_F = g_S$ the terms which grow as Λ^2 cancel and we are left

with a well-behaved contribution to the Higgs boson mass, as long as the fermion and scalar masses are not too different.

$$M_h^2 \sim M_{h0}^2 + \frac{g_F^2}{4\pi^2}(m_F^2 - m_S^2)\,. \tag{2.17}$$

As we described before a supersymmetric theory can provide the required "near-equality" of fermion and boson masses, since in the context of this theory both masses are tied by the structure of the theory. However if supersymmetry is valid at all is certainly not apparent in the zoo of known particles, so any consideration of the implications of supersymmetry at ordinary energies requires us to make some assumption about the mechanism of supersymmetry breaking. Although the exact mechanism of the supersymmetry breaking is not yet well understood, it is believed that supersymmetry breaking occurs in a "hidden sector" of the supersymmetric particles (i.e not the known ones). The remaining question then, is what is the mechanism by which supersymmetry breaking in the hidden sector is communicated to the known particles of the standard model. It is interesting that most of our expectations for the phenomenological implications of supersymmetry depend on the answer to this question, rather than on the details of the breaking of supersymmetry itself. Of course the mechanism for communicating supersymmetry breaking to observed particles must be some sort of interaction that is felt by these particles. Two leading candidates exist for the above scenario. The first is a class of theories of Gravity Mediated SUSY breaking (SUGRA), were the mechanism is provided by gravity (more precisely the auxiliary fields that are superpartners of the gravitational field). The second candidate is a class of theories of Gauge Mediated SUSY breaking (GMSB), were the mechanism is provided by the $SU(3)_C \otimes SU(2)_L \otimes U(1)_Y$ gauge interactions themselves. This dissertation is a search for new physics predicted in the second class of theories.

2.1.2 Gauge Mediation of Supersymmetry Breaking

In this class of theories we consider the possibility that the breaking of supersymmetry is transmitted to the known particles through interactions of the known $SU(3)_C \otimes SU(2)_L \otimes U(1)_Y$ gauge bosons and their superpartners [14]. It is assumed here that supersymmetry is dynamically broken in a sector of the superfields, not including the superfields of the known quarks and leptons, and that some of

the superfields in the symmetry-breaking sector, known as the *messenger superfields*, transmit this breaking due to their interactions with both the remaining superfields in the symmetry-breaking sector and the gauge superfields of the $SU(3)_C \otimes SU(2)_L \otimes U(1)_Y$. Although most treatments of the gauge-mediated supersymmetry breaking also make specific assumptions about the interaction of the messenger superfields with the other superfields responsible for supersymmetry breaking, the most important experimental predictions of this class of theories, in fact do not depend on these assumptions. We will briefly discuss this matter in the following paragraphs, along with the predictions of the experimental signatures involved.

Gauge Mediated Supersymmetry Breaking (GMSB) models are a special case of the so-called Minimal Supersymmetric Standard Model (MSSM), a model that incorporates supersymmetry into the Standard Model by making the absolutely necessary additions in order to change Standard Model into a Supersymmetric theory. These "minimal" additions involve:

- The superpartners to the gauge field bosons (*gauginos*);
- The superpartners to the fermion fields;
- The superpartners to the the Higgs field (more than one usually);
- Some soft-symmetry breaking terms;
- A second Higgs doublet.

In the MSSM model the soft-symmetry breaking terms are placed by hand, while in the variations of this model (Gravity Mediated SUSY breaking (mSUGRA); Gauge Mediated SUSY Breaking (GMSB); and Anomaly Mediated SUSY Breaking (AMSB)), the soft symmetry-breaking terms are provided by the model. One of the features of the MSSM is that all interactions predicted by it are consistent with the global conservation of the difference of the baryon and lepton number (B-L global invariance).

As a result the MSSM possesses a multiplicative R-parity invariance [15], defined as:

$$\mathcal{R} = (-1)^{3(B-L)+2S} \tag{2.18}$$

where S is the spin of the particle, B is the baryon number and L is the lepton number.

The above conservation implies that all ordinary Standard Model particles have even R parity, while the corresponding supersymmetric partners have odd R parity. This conservation of R parity, is reflected in supersymmetric phenomenology. For example, if the initial state involves ordinary (R-even) particles, it follows that supersymmetric particles can only be produced in pairs. Generally these particles are highly unstable and eventually decay into lighter states. However, R-parity invariance also implies that the lightest supersymmetric particle (LSP), which in GMSB models is the gravitino $\tilde{G}$, has to be absolutely stable, and must be produced eventually at the end of a decay chain of a heavy unstable supersymmetric particle. For the LSP, constraints imposed from cosmology suggest that if it is stable it's almost certainly electrically and color neutral [16]. As a result, the LSP in an R-parity-conserving theory is weakly interacting with ordinary matter. In other words, it behaves like a stable heavy neutrino and will escape collider detectors without being directly observed. Therefore the expected signature for conventional R-parity-conserving supersymmetric theories is missing energy due to the escape of the LSP. Also, in GMSB models the next-to-lightest supersymmetric particle (NLSP) plays a crucial role in the phenomenology of supersymmetric particle production and decay. The most likely candidate for the NLSP in GMSB models is the neutralino $\tilde{\chi}_1^0$, which eventually decays into its superpartner γ plus a gravitino $\tilde{G}$, with a lifetime and branching fraction that depends on the model parameters. Depending on it's decay rate, a variety of distinctive supersymmetric phenomenologies [17, 18] appear. For example, if $\tilde{\chi}_1^0 \rightarrow \gamma\,\tilde{G}$ is the dominant decay mode and the decay occurs inside the detector, then nearly all supersymmetric particle decay chains would contain a photon. Figure 2.2 shows an example of a decay mode.

Another feature of the GMSB models, is that they resolve the problem of *flavor changing neutral currents (FCNC)* in a universal way, since the soft-supersymmetry-breaking is communicated to the

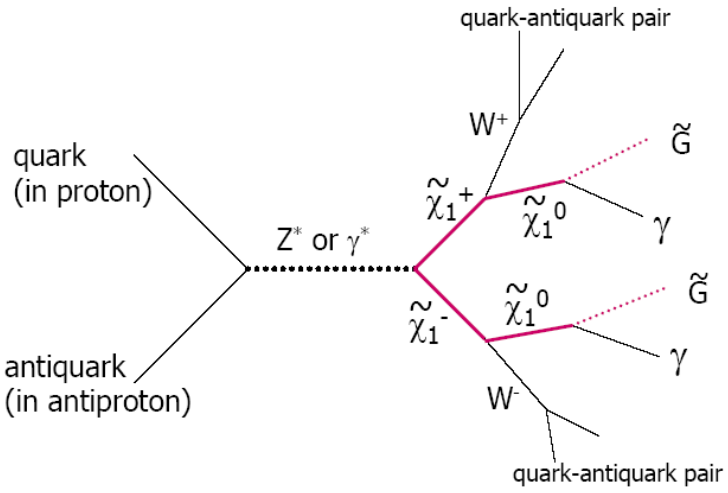

Figure 2.2: An example of a decay mode.

visible sector via gauge interactions. In contrast to other models (that involve a large number of parameters) there is also one effective mass scale Λ that determines all low-energy scalar and gaugino mass parameters through loop-effects. In order for the resulting superpartner masses to be of order 1 TeV or less, one must have $\Lambda \approx 100$ TeV.

A feature of the phenomenology of GMSB models is that involve only a handful of parameters that define the model:

- The SUSY breaking scale in the messenger sector $\sqrt{F}$;
- The number of messenger pairs N_5;
- The SUSY messenger mass scale M;
- The universal effective mass scale of SUSY particles Λ;
- The ratio of Higgs vacuum expectation values $\tan\beta$;
- The sign of the Higgs sector mixing parameter $sign(\mu)$.

This dissertation is a search for the R-parity conserved GMSB model with the dominant decay mode being $\tilde{\chi}_1^0 \rightarrow \gamma\,\tilde{G}$. Since R-parity is conserved in this model, pair-production of supersymmetric particles would occur, and these supersymmetric particles, after decaying inside the detector, will result in a final state with two photons γ and large missing transverse energy $\not{E}_T$.

Chapter 3

Detector Description

This chapter describes the Fermilab Tevatron Collider and the DØ Detector and its subsystems during it's second operational period, Run II. We focus on the subsystems used by this analysis, such as calorimeter, preshower and tracking systems. Also we discuss the trigger and data acquisition (DAQ) systems, and the luminosity measurement.

3.1 Overview of the Tevatron Collider

The Tevatron Collider is a $p\bar{p}$ collider with a center-of-mass energy of 1.96 TeV located at Fermilab. Its operation started in 1987 [19] and by the year 1988, 1.8 TeV collision energies were achieved. Its main mission was to provide the highest possible center-of-mass energy proton-antiproton collisions for its two main collider detectors, the DØ and CDF detectors. During the Run I physics program (1992-1996), the Tevatron ran with 1.8 TeV collision energy and delivered luminosity to each of the two collider detectors of nearly 130 pb^{-1}. Currently the Run II physics program is underway, with the collider being upgraded to deliver both a higher center-of-mass energy (1.96 TeV) and much higher luminosity. This is the highest energy collider program operating currently in the world, and will remain the energy frontier until the completion of the Large Hadron Collider (LHC) at CERN that will start its operation some time at the end of this decade. As with most high energy accelerators, the Tevatron complex is a chain of increasing energy accelerators, as shown in Figure 3.1. This

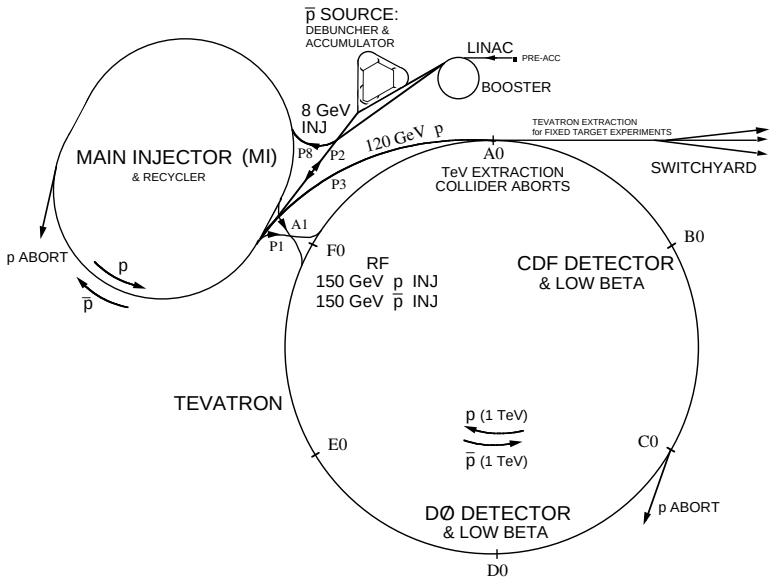

Figure 3.1: Schematics of the Run II Fermilab accelerator complex.

accelerator chain consists of the following basic components:

- Pre-accelerator: A Cockroft-Walton;
- Linear Accelerator: The LINAC;
- The Booster Synchrotron;
- The Main Injector;
- The Anti-proton Source;
- The Debuncher, Accumulator;
- The Recycler;
- The Tevatron Ring Synchrotron.

All of these components are necessary in order to produce and accelerate the beam to the desired energy and luminosity and therefore provide the physics signals for study.

3.1.1 Cockroft-Walton pre-accelerator

The process of creating the beam begins with hydrogen gas released into a magnetron surface-plasma source. An electric field produced between the magnetron's anode and cathode strips off the electron from the hydrogen atom. Some of these free protons then become attached to the cathode's

surface where they collect electrons, and some of them happen to capture two electrons and they become H^- ions. These negatively charged H^- ions are then guided outside the magnetron using a magnetic field and accelerated initially to a kinetic energy of 18 keV. After that they are released to an electrostatic Cockroft-Walton accelerator which further boosts their kinetic energy to about 750 keV.

3.1.2 The LINAC

After leaving the Cockroft-Walton pre-accelerator the next stage for the H^- ions is the the LINAC. LINAC is a 500-foot-long ($\approx$ 152 m) linear accelerator that uses a set of oscillating electric fields (along the direction of the ion stream) to further boost the H^- ions to a kinetic energy of 400 MeV. Just before entering the next stage of the acceleration, a debuncher is used to remove the 805 MHz structure of the ion stream due to the oscillating electric fields of LINAC. After debunching the H^- ions are then passed through a carbon foil which strips the two electrons from each ion, leaving a stream of protons.

3.1.3 The Booster Synchrotron

The protons exiting the LINAC are guided into the Booster, a 1570-foot-circumference ($\approx$ 478 m), fast-cycling synchrotron ring, which is also the first synchrotron accelerator that the beam encounters. Here the protons are constrained to a closed circular orbit using a series of bending magnets while at the same time quadrupole focusing fields prevent the beam from diverging. At each revolution around the ring, protons pass through a set of radio frequency (RF) cavities that steadily increases their energy. As the particles energy is increased both the magnetic field strength and the RF frequency must increase in a synchronous manner in order to continue the protons to stay in the same orbit (hence the term "synchrotron"). After about 20,000 revolutions around the Booster ring the proton beam reaches an energy of about 8 GeV, while at the same time it is bunched again into a train of about 5 to 7 bunches, each containing about $5 - 6 \times 10^{10}$ protons.

3.1.4 The Main Injector

The next stage of the acceleration is the Main Injector, a 120-150 GeV, 2 mile in circumference (3 Km) synchrotron ring, located tangentially next to the Tevatron ring at the FØ straight section. This ring is a new addition for the Run II upgrade at the Fermilab facility and it replaces the Main Ring, which operated during Run I. The Main Injector is capable of delivering up to 3 times as many protons as the Main Ring. Being located outside of the enclosure of the Tevatron ring (in contrast the Run I Main Ring was inside the same tunnel), reduces beam halos and backgrounds seen in the colliding detectors during Run I. There are two functions that the Main Injector performs. The first is to coalesce the proton bunches injected from the Booster into a single high-intensity bunch of $\approx 5 \times 10^{12}$ protons and further boost their energy up to 150 GeV, before the proton beam is delivered to the Tevatron ring. The second function is to extract proton bunches at 120 GeV and them deliver them to the anti-proton facility.

3.1.5 The Anti-proton Source

While protons are relatively easy to produce, anti-protons are much more difficult especially in large quantities; in fact the main limiting factor for the Tevatron is the intensity of the anti-proton beam. There is a dedicated facility that produces the anti-proton beam by using the 120 GeV proton bunches delivered by the Main Injector. This proton beam is directed to impact on an external 10 cm diameter, 2 cm thick, nickel/copper target disk. Secondary particles produced after the impact include anti-protons that have a range of momenta and production angles and for that reason a lithium collector lens is used to focus them. The emerging anti-protons are collected into the first of two anti-proton storage rings.

3.1.6 The Debuncher and the Accumulator

The first storage ring on which the anti-protons are delivered is the Debuncher, a ring housed in the same 1700-foot-circumference ($\approx$ 518 m) tunnel along with the Accumulator. The purpose of the debuncher is to reduce the momentum spread of the anti-protons and also by applying stochastic

cooling to restrict their transverse oscillations. Once a coherent beam of 8 GeV anti-protons is achieved it is transferred to the second ring, the Accumulator. Here anti-protons are cooled further (using RF and stochastic cooling techniques), stacked with rates up to 10^{12} anti-protons per hour, and also arranged into bunches similar to the proton ones already in the Main Injector. Once the stack reaches the desired amount of anti-protons it is transferred to the Main Injector through the Recycler.

3.1.7 The Recycler

The main purpose of the Recycler (a 8 GeV permanent magnet storage ring), is to operate as a recovery channel for anti-protons left at the end of the previous store. The Recycler accumulates and re-cools dilute anti-protons and once they reach an energy of 8 GeV they are transferred to the Main Injector where their energy is boosted to 150 GeV.

3.1.8 The Tevatron Ring Synchrotron

The final stage of the acceleration process is the Tevatron ring. The Tevatron is a 4-mile-circumference ($\approx$ 6 km) synchrotron ring. Within it's tunnel, superconductive magnets produce fields of 4 Tesla, allowing the proton and anti-proton beams delivered by the Main Injector to reach a maximum energy of 0.98 TeV each. Once this energy is reached, the beams are squeezed to small transverse dimensions (through the usage of low-beta quadrupole magnets), at two different locations of the ring named BØ (location of the CDF particle detector) and DØ (location of the DØ particle detector). As mentioned before, the final beams are not continuous, in reality they are just groups (bunches) of protons and anti-protons moving in the opposite direction inside the Tevatron ring, and having a certain time structure. In Run II the Tevatron is operating with 36×36 $p\overline{p}$ bunches with a 396 ns bunch spacing interval.

3.2 Overview of the DØ Detector for Run II.

The DØ Detector is a general purpose nearly-hermetic particle detector, designed and constructed to study interactions originating from $p\overline{p}$ collisions at $\sqrt{s} = 1.96$ TeV at the Fermilab Tevatron Collider [20]. The experiment was first provisionally approved in 1983 and the full conceptual design report was prepared a year later [21]. It has been in successful operation since 1992 with the beginning of the Run I physics program. The entire assembly approximates to about 13 m-high $\times$ 12 m-wide $\times$ 20-m long and weighs roughly 5500 tons. The detector and it's platform are mounted on mechanical rollers that allow the detector to move from the assembly area (*i.e.,* construction and installation stage) to the collision hall (*i.e.,* operation and data acquisition stage).

The detector is optimized to measure final states that contain photons, electrons, muons, jets, and missing transverse momentum from a number of processes originating from $p\overline{p}$ collisions. It is particularly suited to study high-mass states and large transverse momenta (high-p_T) phenomena. After the completion of the Run II upgrade program, the new detector continues to detect these important physics signatures, while at the same time its physics reach has been extended to lower-p_T final states, as well as to vigorous B-physics. In Run I, DØ played a crucial role in the experimental high energy physics program at Fermilab and indeed was a major world facility. For example, in 1995 the top quark was discovered by the DØ Collaboration together with CDF [5, 6].

The prime physics focus of the DØ experiment in Run II are both detailed study of known physics and searches for new physics. The detailed study of high-mass states, high-p_T phenomena, B-physics, and precision study of the top quark and the W and Z bosons to provide sensitive tests of the Standard Model, play a key role in Run II. Also, searches for the Higgs boson and new phenomena searches beyond the Standard Model such as searches for supersymmetry and extra dimensions, are at the heart of the DØ experiment in Run II.

A 3D cut-away view of the DØ detector [22] is shown in Figure 3.2.

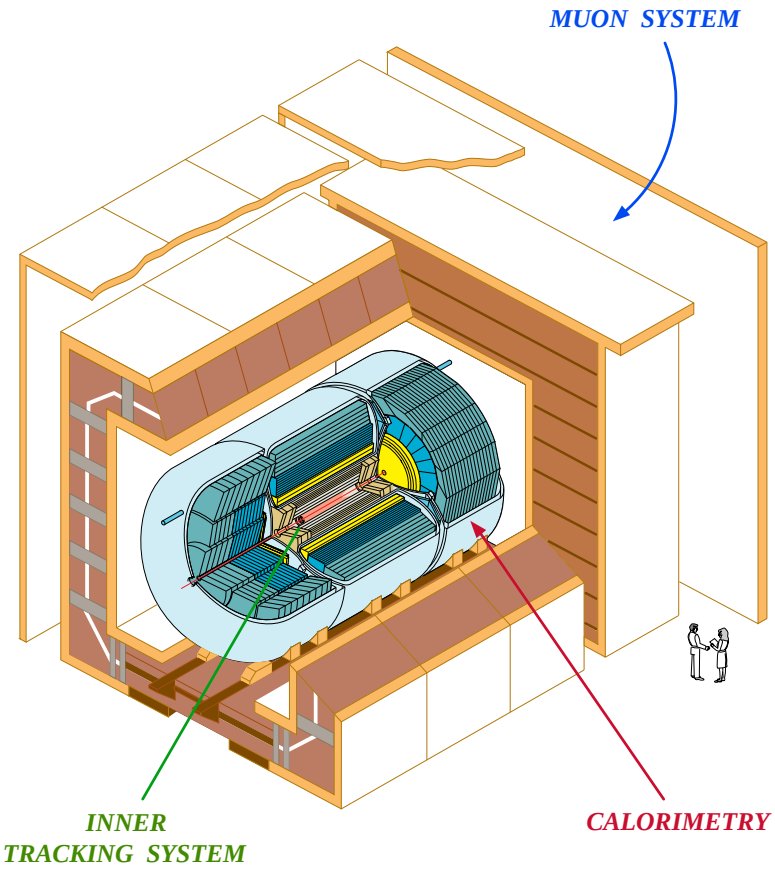

Figure 3.2: 3D view of the DØ Detector.

3.3 Coordinate System and Other Conventions at DØ

Before discussing the DØ detector, it is useful to define the DØ coordinate system and some basic concepts used. DØ uses a standard right-handed coordinate system. In this system the direction of the +x axis is a vector pointing radially outwards from the center of the Tevatron ring, the +y axis direction is vertically upwards and the +z axis direction is along the proton direction [4]. Since some of the detectors have a cylindrical symmetry it is also convenient to use a combination of cylindrical and spherical coordinates (z, ϕ, θ) along with the cartesian ones. The angles ϕ and θ are the azimuthal and polar angles, respectively (θ=0 along the proton beam direction). Figure 3.3 shows these variables used in the DØ detector.

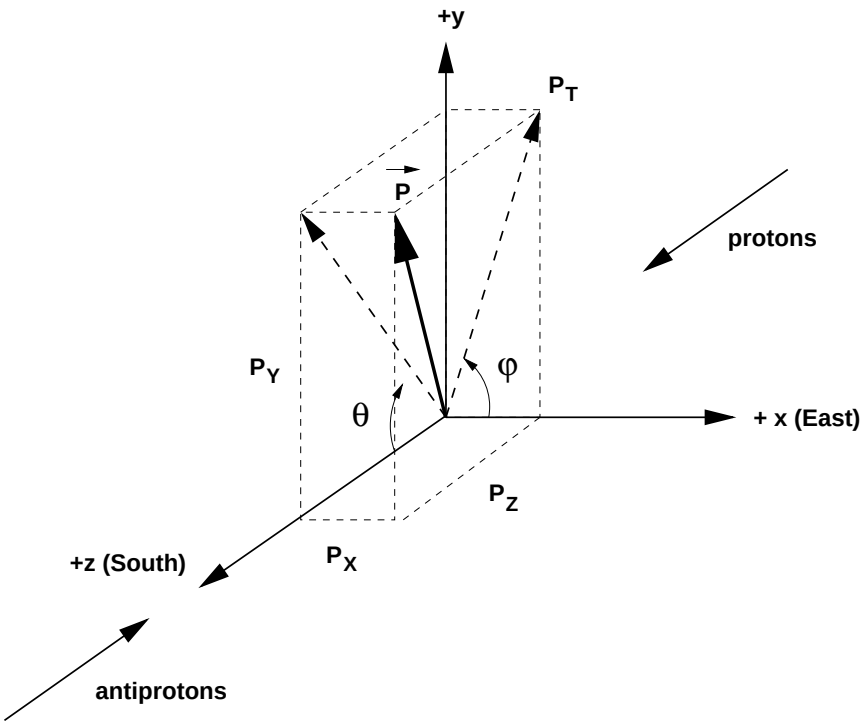

Figure 3.3: View of the DØ coordinates.

Another kinematic variable used in place of the polar angle θ is the rapidity, y. The definition of rapidity is:

$$y = \frac{1}{2} \ln \left[\frac{E + p_z}{E - p_z} \right] \tag{3.1}$$

and it is a more logical quantity to use than θ due to the fact that rapidity intervals are Lorentz

invariant. Although y is useful, the quantity that most often is utilized is the pseudo-rapidity, η, defined as

$$\eta \equiv -\ln(\tan(\theta/2)) = \tanh^{-1}(\cos\theta) \tag{3.2}$$

which approximates the true rapidity y for finite angles in the limit that $m/E \to 0$. It has to be noted here that in a $p\overline{p}$ collider experiment like DØ, the dimensions of the beams along the x and y axis tend to be very small, but along the z axis where the actual collisions take place the size of the beam is not as limited. Because of this the primary interaction point has a Gaussian distribution in the z axis with mean $z = 0$ and $\sigma_z = 28$ cm as is it shown in Figure 3.4. As a result of this

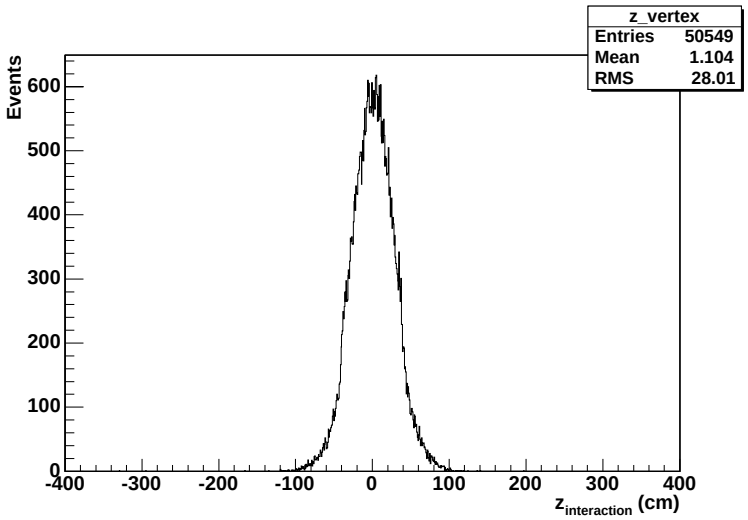

Figure 3.4: Distribution of the interactions point's z-axis position.

beam structure there is another useful pseudo-rapidity variable, the detector pseudo-rapidity, η_d. This pseudo-rapidity is computed with respect to an interaction point whose position is at $z = 0$. Because the real interaction point's position is distributed around $z = 0$, η (also called the "physics" pseudo-rapidity) and η_d may be different. Other kinematic variables that are commonly used for the analysis at DØ are transverse energy[1] $E_T = E\sin\theta$ and transverse momentum $p_T = p\sin\theta$.

The motivation for using these variables is the fact that the center-of-mass energy ($\sqrt{\hat{s}}$) of the scattering in $p\bar{p}$ collisions is not fixed [23]. This is a consequence of the parton structure of a

[1]Note that the term *transverse energy* can have two meanings. At DØ it is typically used for $E_T = E\sin\theta$. This meaning is implied in the dissertation. However this term may also be used to denote the energy in the frame of zero longitudinal momentum (which is not equal to $E\sin\theta$ [23])

nucleon [10]. The partons (quarks and gluons) each carry only a fraction of the total nucleon energy. Scattering of partons of different energy results in the center-of-mass frame that does not coincide with the lab frame; also the total energy released in the collision is only a fraction of the total energy of the colliding beams. Although the collision energy of the nucleons as a whole is fixed, the energy balance can not be used to analyze the outcome of the collision, since a significant fraction of energy escapes the detector as the nucleon remnants (*spectators*) carry it away down the un-instrumented beam-pipe. However, the transverse energy balance can be used since it is known to be zero before the collision and its undetectable fraction is negligible.

3.4 The DØ Detector Components

The following sections provide a brief overview of each of the components in the Run II DØ detector. For a much more complete treatment, the reader is referred to the existing write-ups, design reports, and publications on the individual subsystems [24]

The DØ detector consists of the three major subsystems:

1. Inner Tracking System;
2. Calorimeter System;
3. Muon System.

The full list of the DØ detector components includes:

- Preshower detectors;
- Intercryostat and Massless Gap Detectors;
- Luminosity Monitor;
- Forward Proton Detector (FPD);
- Trigger Framework;
- Data Acquisition System (DAQ).

Figure 3.5 shows the $r - z$ view of the DØ detector [22] indicating its major components.

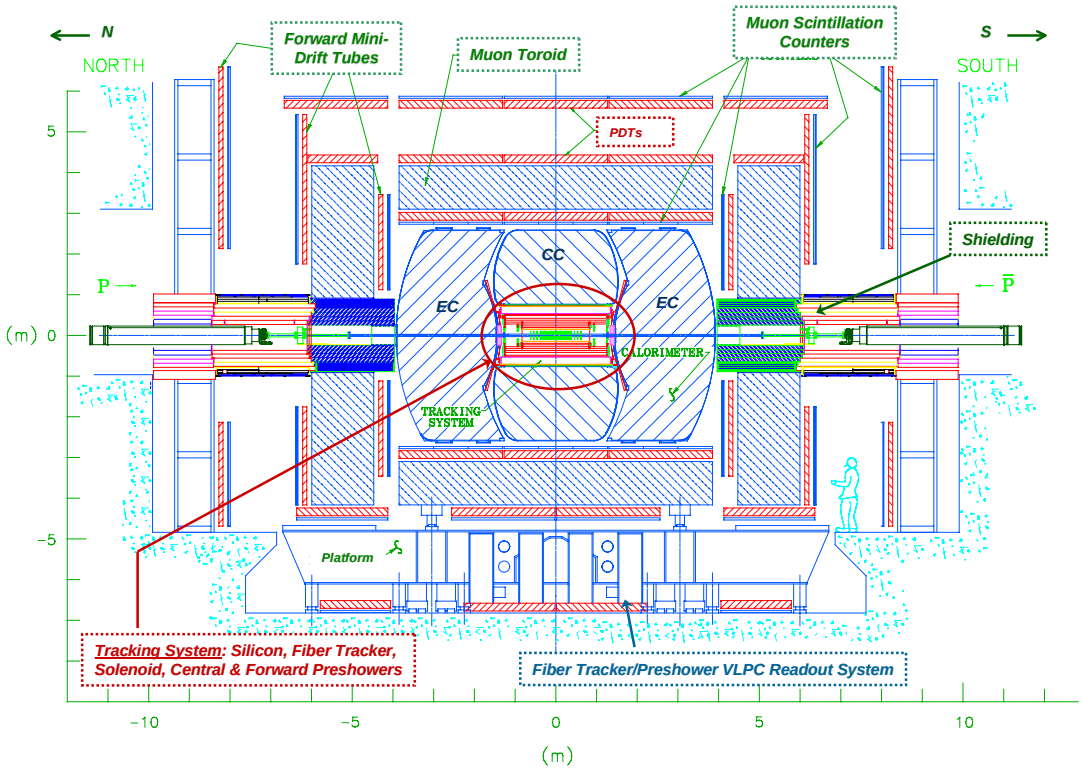

Figure 3.5: The $r - z$ view of the DØ Detector.

3.4.1 Tracking System

The tracking system of the upgraded DØ detector consists of two subsystems:

- The Silicon Microstrip Tracker (SMT);
- The Central Fiber Tracker (CFT).

Surrounding these subsystems is a superconductive solenoid magnet, which provides a 2 Tesla magnetic field parallel to the beam direction. In combination with the magnetic field, the trackers are designed to perform the following goals:

- detection of charged particles over large range of pseudo-rapidity ($\eta \approx \pm 3$);
- charged particle momentum measurement in the solenoidal magnetic field;
- secondary vertex measurement for identification of heavy flavors.

In the following sections we will take a closer look at these two subsystems. The $r - z$ view of the quadrant of the tracking system is shown in Figure 3.6.

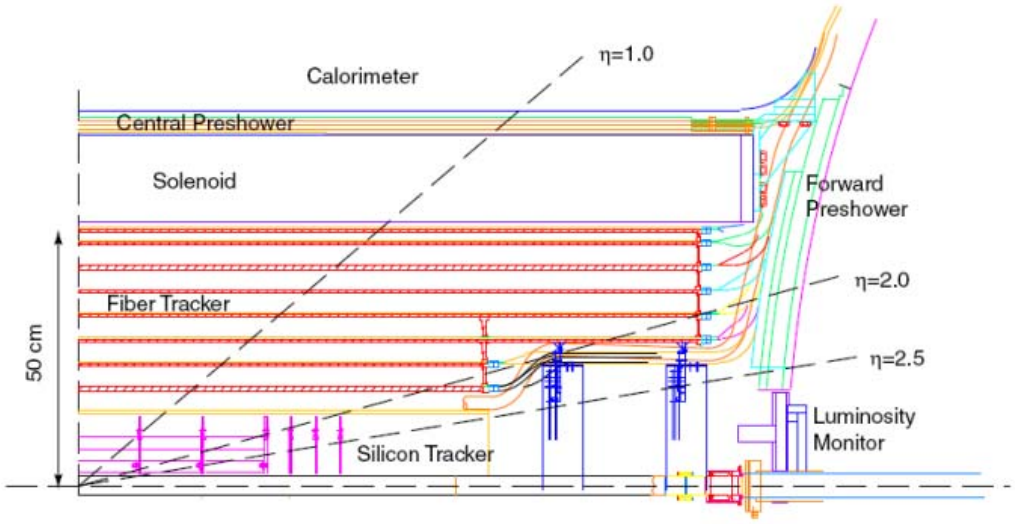

Figure 3.6: DØ tracking system (the quadrant $r - z$ view) (Adapted from [25]).

3.4.2 Silicon Microstrip Tracker

The innermost tracking subsystem and the component closest to the Tevatron's beryllium bean-pipe is the Silicon Microstrip Tracker (SMT) [26] shown in Figure 3.7. This is a completely new component and it was included in the DØ Detector as part of the Run II upgrade [27]. Its primary function is to provide precision tracking and vertex information from the interaction point in $p\overline{p}$ collisions as well as to identify and reconstruct displaced vertices from the primary interaction. These secondary vertices are characteristic signatures of relatively long-lived decaying particles containing b and c quarks as shown in Figure 3.8

The choice of a silicon semiconductor tracking device was motivated by the following properties of the silicon [28]:

- low ionization energy (good detectable signal);
- long mean free path (good charge collection efficiency);

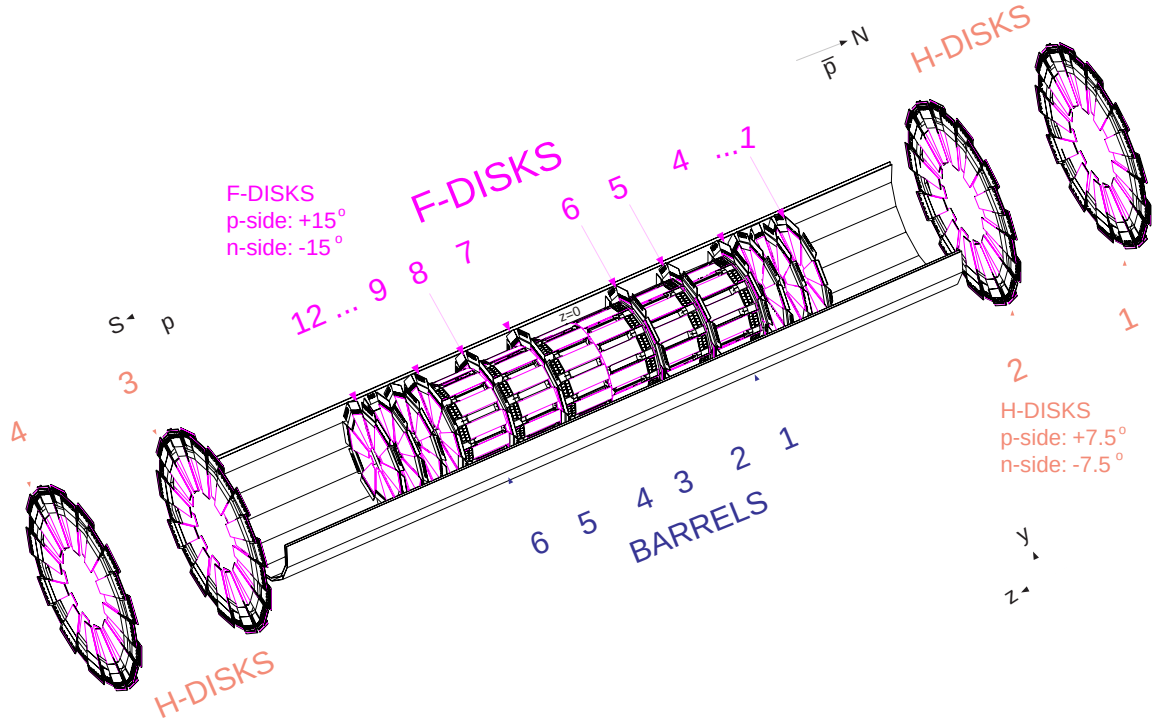

Figure 3.7: The SMT design structure.

- high mobility (fast charge collection);
- low Z (low multiple scattering);
- well-developed technology.

Mechanically, the tracker consists of two parts symmetric with respect to $z = 0$ with the north-SMT ($z > 0$) and the south-SMT ($z < 0$). The fact that the primary interaction point has a Gaussian distribution in the z axis with mean $z = 0$ and $\sigma_z = 28$ cm, as it shown in Figure 3.4, defines the shape and length of the SMT detector. The Silicon Tracker was designed as a hybrid system consisting of *barrel detectors* measuring primarily the $r-\phi$ coordinate and *disk detectors* which measure $r - z$ as well as $r - \phi$. The above hybrid design provides detector surfaces at all η so that the tracks are generally perpendicular to them. In this type of system, the tracks for high η particles are reconstructed in three dimensions primarily by the disks, while particles at small η are detected primarily by the barrels. The interspersed disk and barrel design is shown in Figure 3.7.

Additionally the detector must be radiation-hard to operate efficiently in the high luminosity environment of Run II, while the small bunch crossing interval expected in Run II sets the performance

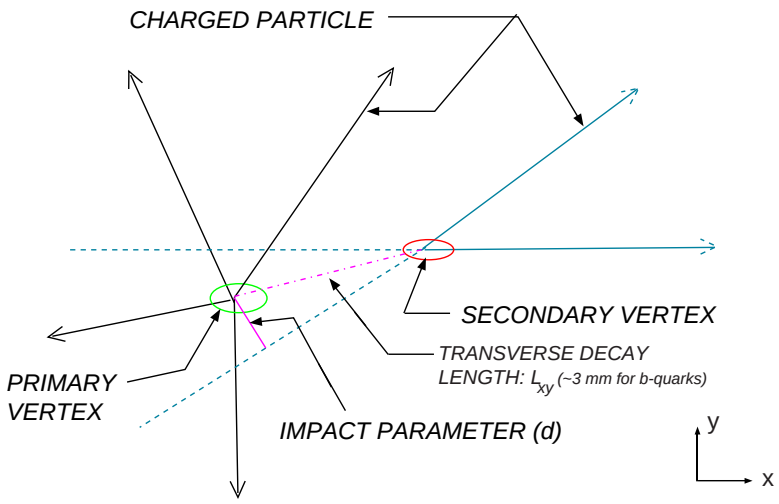

Figure 3.8: Displased vertex originating from b or c quarks.

criteria for the readout electronics of the SMT. Both barrels and the disks have the same conceptual structure. The basic detector unit [25] consists of:

1. Silicon microstrip sensors;

2. SVX II front end readout chips;

3. High density interconnect (HDI) circuit with Kapton strip cable;

4. Supporting Rochacell-carbon and beryllium components.

The basic detector unit for the barrel detector is called a *ladder*. There are three types of ladders distinguished by the number of readout chips and types of silicon sensors: 3-chip, 6-chip and 9-chip ladders. The 3-chip ladders are single-sided detectors, while the 6-chip and 9-chip ladders are double-sided stereo detectors, with the 6-chip detectors having an angle of 90° and the 9-chip detectors having a small 2° angle. The 3-chip ladder shown in Figure 3.9 is a 300 μm-thick, 12 cm $\times$ 2.1 cm detector consisting of two silicon sensors. Each sensor is a one-sided sensor with 50 μm strip pitch. The two sensors are wire-bonded together on the strip side and supported by the rochacell-carbon fiber support rails on the other side (not shown in the photograph). The strips are connected to the SVX II chips which are mounted on the HDI circuit. The HDI circuit is laminated onto a 300 μm thick beryllium plate and glued to the surface of the detector. Similar is the construction of the

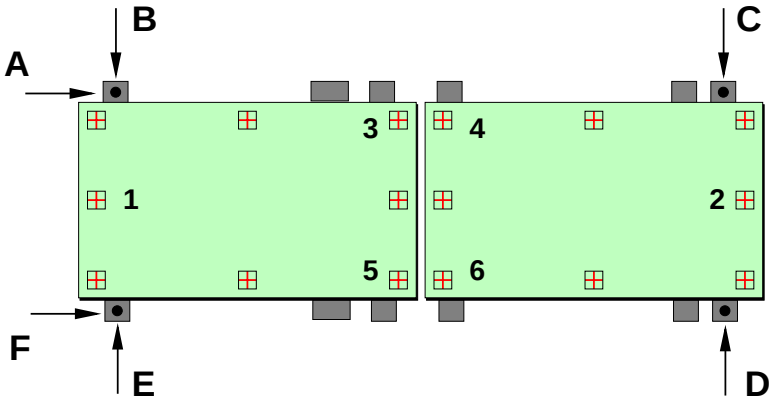

Figure 3.9: Illustration of a 3-chip ladder. Features measured with OGP probe are four Be structures (AB, C, D EF) and six fiducials on the sensor surface (1-6).

9-chip ladder, consisting of two double-sided (instead of single-sided) 2° silicon sensors. The 6-chip ladders consist of one double-sided small-angle 90° silicon sensor.

The ladders are mounted on *bulkheads*, made from beryllium, a light material used to reduce scattering from the support structure of the detector. They are arranged in patterns of four concentric layers extending radially from 2.7 to 9.4 cm surrounding the interaction point. Such a pattern allows to reconstruct a track of a charged particle based on the hit position at each layer. A *bulkhead* is a mechanical structure made out of beryllium. A schematic diagram of a bulkhead is shown in Figure 3.10. In addition to providing mechanical support, it also serves as an enclosure for the integrated coolant channel system. The cooling ($< 10°$ C) is needed for optimal mode of operation of silicon detectors. Figure 3.11 shows ladders mounted on the bulkhead structure. The SMT is a complicated device with a high level of performance requirements for the first time used in DØ. For example the total number of readout channels is 792,576 [25] (for comparison, in the calorimeter system this number is 55,000 [29]).

Interspersed within the barrels are twelve 8 mm-thick disks, known as the F-Disks. The basic detector unit for the F-Disks is called a *wedge*, these are double-sided detectors with $\pm 15°$ stereo strips (with a strip pitch of 62.5 μm for the n-doped side and 50.0 μm for the p-doped side), overlapping to help improve tracking up to large η. There are 12 such wedges in each F-Disk. Additionally in the forward region there are four H-Disk assemblies (two symmetrically located on each side of the $z = 0$) helping to extend the tracking up to $|\eta| = 3$. These assemblies have back-to-back single-sided

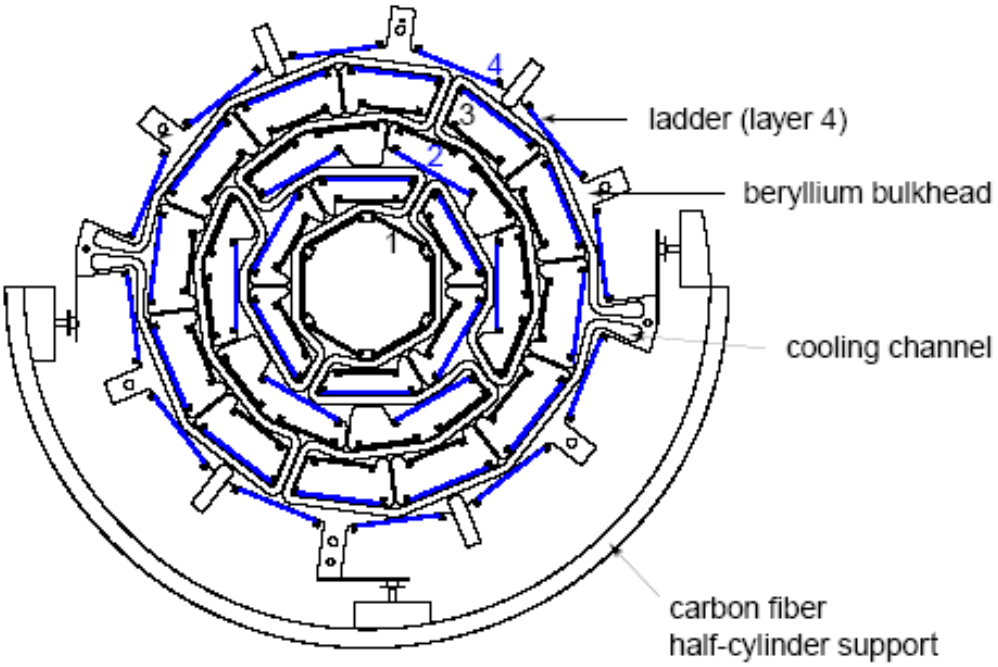

Figure 3.10: The $x - y$ view of the bulkhead.

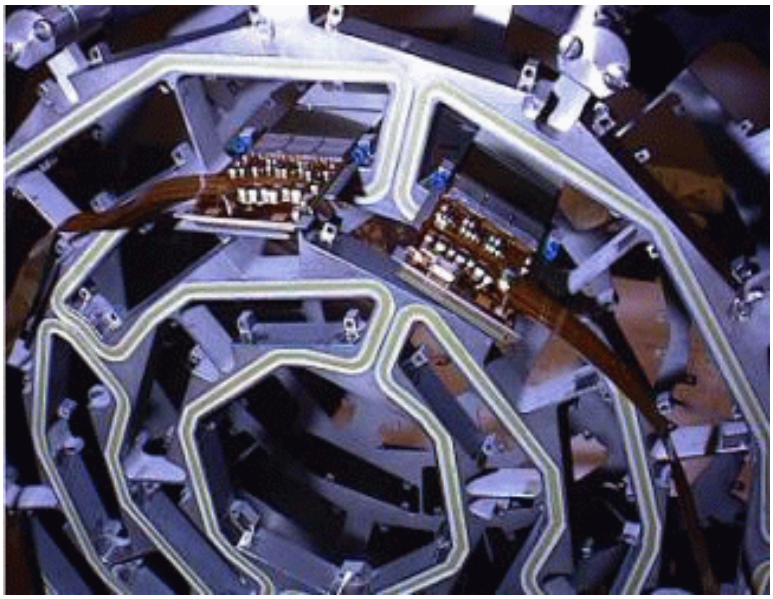

Figure 3.11: A bulkhead with two ladders installed.

wedge detectors with an effective $\pm 7.5^{\circ}$ stereo strips and 81 μm pitch strips. Again the wedges of both the F and H-Disks are mounted on beryllium bulkheads, that provide the mechanical support needed while they enclose the coolant channel system.

The SMT is a very compact detector compared with the other detector subsystems, and its construction was a challenging enterprise for the people that were involved in it. Each of the detector elements (SVX chips, beryllium components, HDI's Kapton strip cables) had to undergo a set of tests, to ensure quality control. Before the finished units (ladder or wedges) were assembled, they had to be tested for performance (burn-in test, laser test), and also features on the silicon sensor and the unit itself had to be precisely measured using a Coordinate Measuring Machine (CMM) [30, 31]. The CMM measurements were done with an Optical Gauging Platform (OGP), these measurements would later ensure precise placement and alignment on the supporting bulkhead. The author of this dissertation was heavily involved with both the OGP measurements of the barrel ladders, as well as with the assembly of the barrels [32]. The main purpose of the OGP measurements was to associate fiducials on the surface of the silicon sensor with ladder features (beryllium support structure). These features during the assembly phase would be precisely measured using a CMM machine, and by combining the two set of measurements, the precise position of the silicon sensor surface with respect to the bulkhead would be determined. An illustration of a 3-Chip ladder, with the measured fiducials on the sensor surfaces and the beryllium (Be) support structures, is shown in Fig. 3.9, while in Fig. 3.12 the relative placement of the optically measured point on the Be support structures, in respect to the ladder plane for a set of installed 3-Chip ladders is shown. During the production phase of the ladders, several other studies were done using the OGP. Studies to determine the best method of performing the OGP measurements (with ladders mounted or free on the optical table) were done, Fig. 3.13 shows a comparison between those methods. The results of these studies, indicate that mounted measurement reproduces better the real placement of the ladder in the barrel module. In order to determine the quality of the delivered silicon sensors, flatness studies performed using OGP, by measuring along with sensor's fiducial features, a grid of points on the silicon surface (before the HDI was attached). Figure 3.14 shows the grid of points taken along with the fiducials for

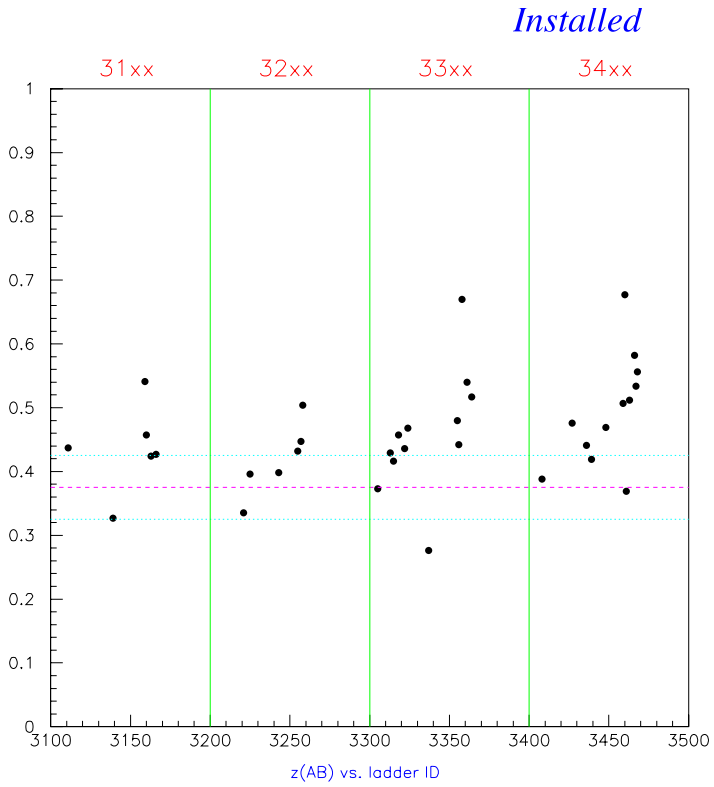

Figure 3.12: Placement of the Be support structures with respect to the ladder plane at the measured point AB of 3.9, for a set of installed 3-chip ladders. Ladder plane is defined by the six points (1-6) shown in 3.9.

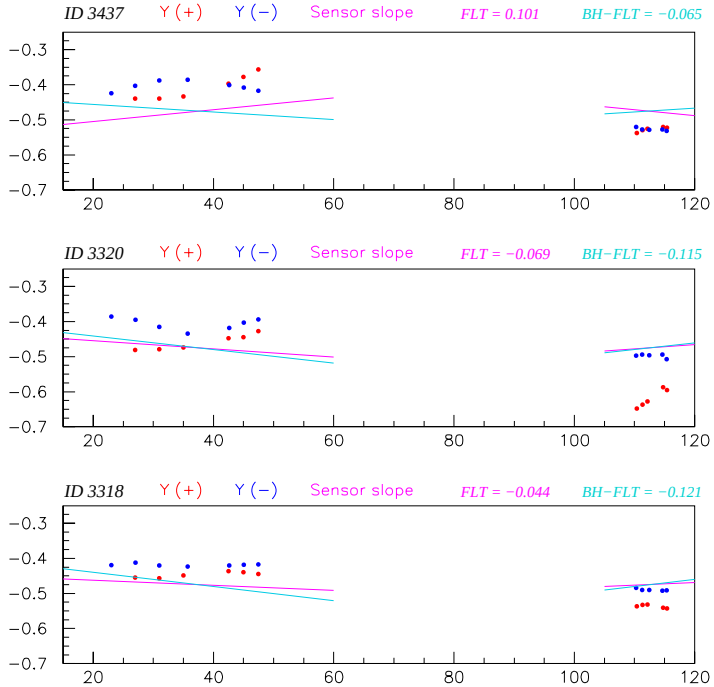

Figure 3.13: Slope of the sensor plane for free (magenta) vs. mounted (cyan) optical measurements for a set of 3-chip ladders. Be support structures on the two sides of the ladder are shown as points (red-blue).

the 9-chip sensors. A more detailed study of the Be support structures alignment with the ladder's

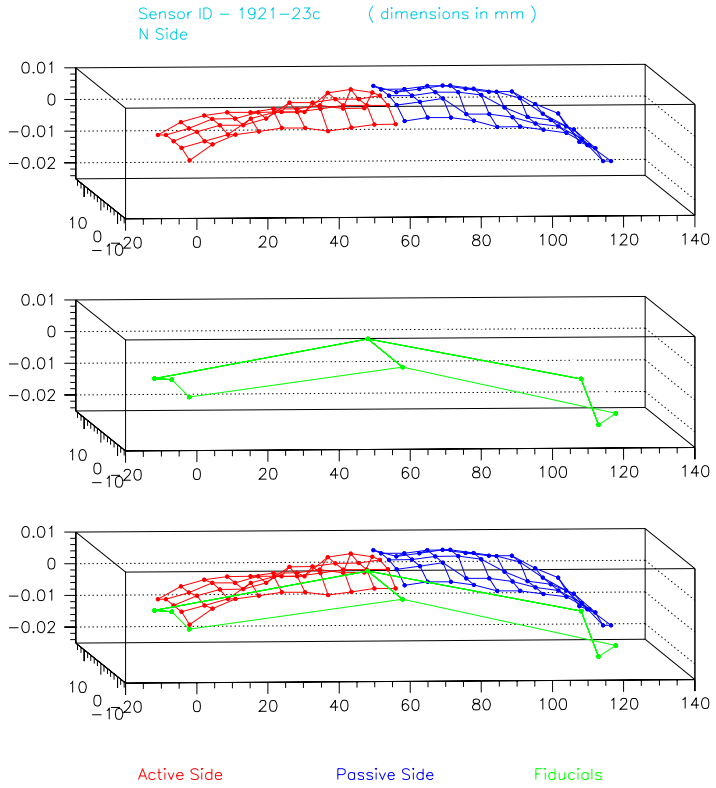

Figure 3.14: Measured fiducials (green) and points (red-blue) on the surface of a 9-chip sensor. Active sensor is the one on which later will be attached the HDI with the SVXII readout chips.

plane was performed also. Using OGP, a set of points on the Be surface was measured, to create a profile as it shown in Fig. 3.15 for a set of 3-chip ladders. Flatness studies were performed also for full fabricated ladders, measuring sensor fiducials, points on the surface of the sensor, and points on the surface of the Be support structures as it shown in Fig. 3.16 for a 6-chip ladder. The assembly stage itself possed also some challenges. For example at the assembly stage of a barrel several goals had to be achieved:

1. Protect the production stage quality of a ladder (very small forces applied and chemical changes in the environment may affect the ladder properties dramatically).

2. Retain the quality of the readout electronics performance as a ladder is moved out of the production and testing enclosure.

3. Precise mechanical positioning of ladders onto a bulkhead that should be retained at the

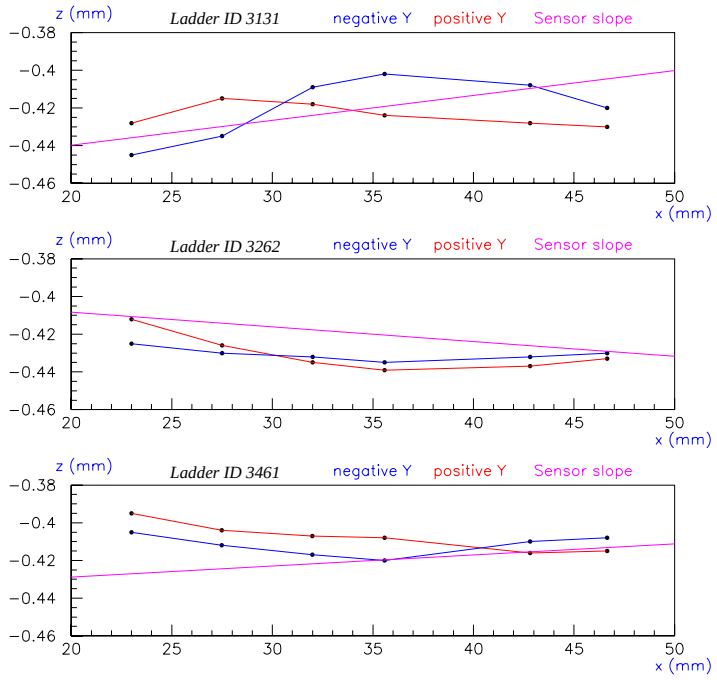

Figure 3.15: Profile of a measured set of points (red-blue) on the Be support structure surface. The slope of the 3-chip sensor is shown in magenta.

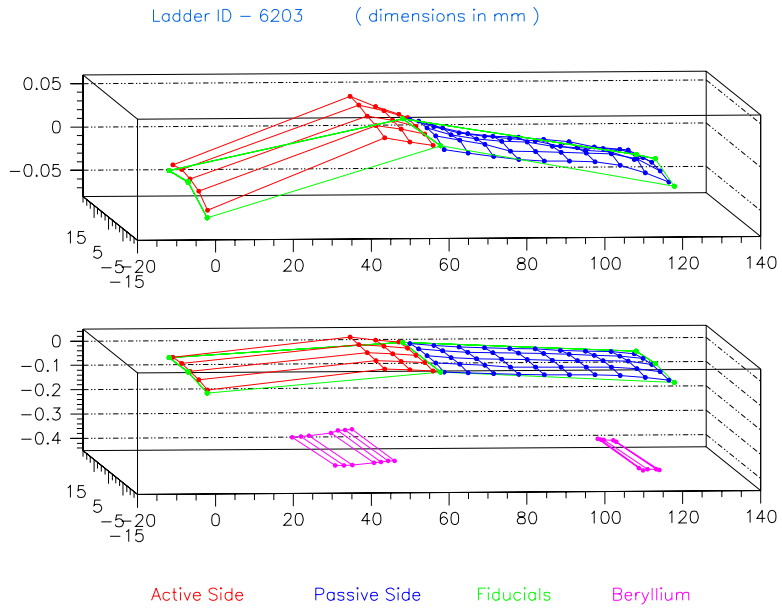

Figure 3.16: 3D Flatness profile of a 6-chip ladder. Various measured features are shown as sensor points (red-blue), fiducials (green) and Be support structures (magenta).

subsequent stages of the SMT construction and commissioning such as combining barrels with disks into enclosing support structure, installing the SMT into the DØ Detector in the experimental hall.

4. Allowing access for the cabling and cooling system outlets.

In order to meet these quality objectives, the task of barrel assembly was performed under controlled conditions in a clean room. The precise mechanical positioning of the ladders on the bulkhead, was done by specially trained technicians, while their position was repeatedly measured using a CMM machine. To ensure high quality performance, the CMM machine was calibrated daily (as was the OGP machine), while a dedicated program to measure features on the face of the bulkhead (ruby calibration spheres), ensured the precise knowledge of the bulkhead positioning in the CMM's measuring table. All of these objectives during the production and testing phase, were of different nature but had to be achieved simultaneously and in relatively small amount of time, which made it a creative and exciting task [33].

3.4.3 Central Fiber Tracker

The scintillating fiber tracker surrounds the silicon detector and covers the central pseudo-rapidity region [27] as shown in Figure 3.6. The fiber tracker serves two main functions:

1. Together with the silicon detector it enables track reconstruction and momentum measurement for all charged particles within the range $|\eta| < 2.0$. Combined hit information from the two tracking systems allows to improve the overall tracking quality.

2. The fiber tracker provides fast "Level 1" track triggering within the range $|\eta| < 1.6$.

A total of about 76,800 scintillating fibers are mounted on eight concentric cylinders. These cylinders are made of carbon fiber and occupy the radial space from 20 to 51 cm. The inner two cylinders are 1.7 m long while the outer six are 2.5 m long. This difference in length is to accommodate the silicon H-Disk detectors located at high η. Each of the cylinders supports a doublet layer of fibers (two mono-layers placed with an offset of one half of the fiber spacing, compensating

for the geometry gap), oriented in the axial direction, parallel to the beam line and a doublet layers of fibers that are oriented at alternating u or v 3.0°) stereo angles. From the innermost to the outermost barrel the orientations for the layers follow the pattern $xu - xv - xu - xv - xu - xv - xu - xv$ where x is the axial doublet layer.

Studies performed in a cosmic ray test stand have shown a doublet hit position resolution of ≈ 100 μm for single muons (see Figure 3.17).

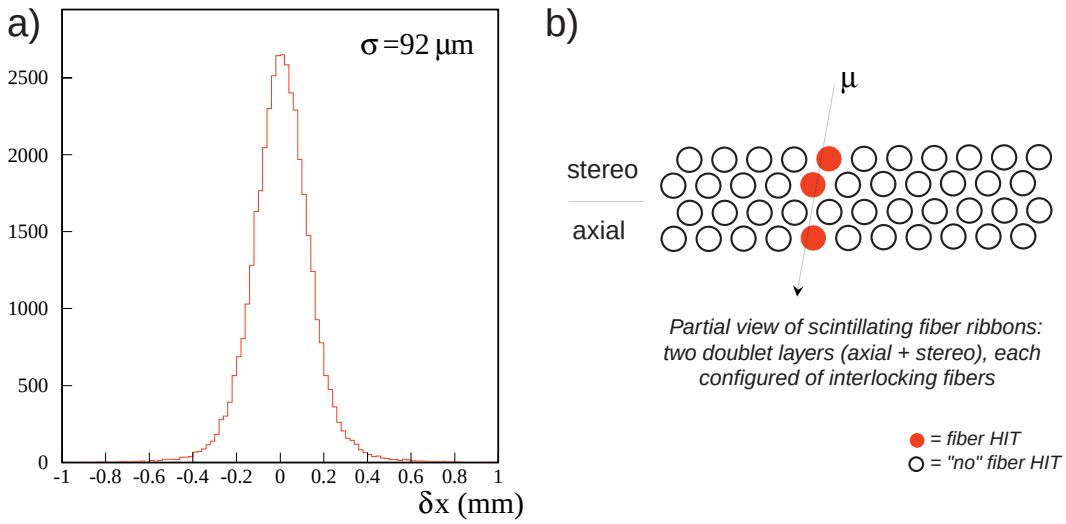

Figure 3.17: a) Position resolution distribution measured in the CFT cosmic ray test stand. b) End view of the interlocking doublet ribbon configuration.

The basic detection element is the multi-clad scintillating fiber. The inner polystyrene core of the fiber is surrounded by two layers of cladding (acrylic and fluoroacrylic). These three materials have indices of refraction of 1.59, 1.49, and 1.42, respectively. The fiber diameter is 835 μm and each cladding is 15 μm thick. The fiber scintillates in the yellow-green part of the visible spectrum, with the peak emission wavelength near 530 nm.

Figure 3.18 shows the $r - z$ view of the scintillating fiber tracker and the end view of the tracker fibers [22].

Scintillating fibers are mated to the waveguides by plastic, diamond-finished optical connectors. These waveguides conduct the scintillation light to photodetectors, which are Visible Light Photon Counters (VLPC) (e.g. [34]). A VLPC is a variant of the solid-state photomultiplier, operating at

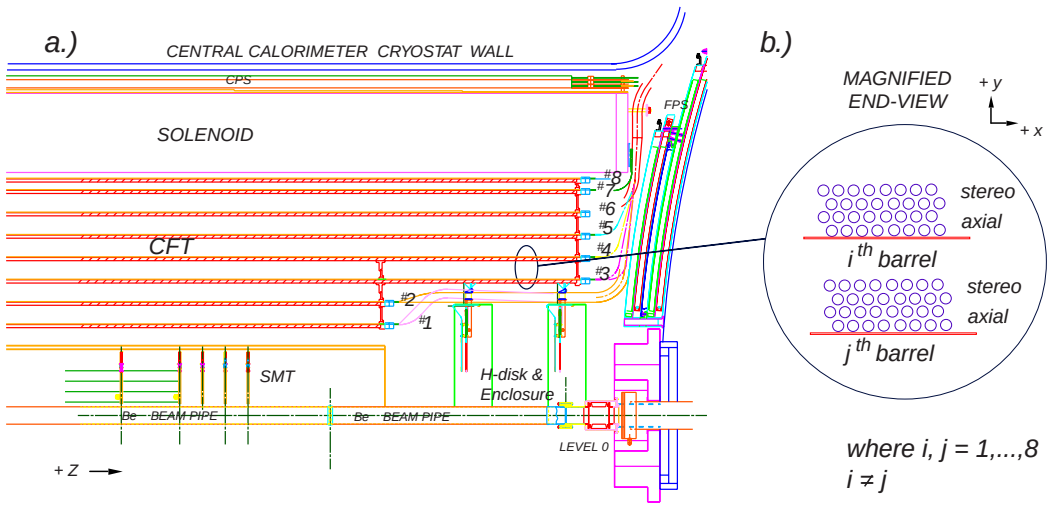

Figure 3.18: The $r - z$ view of the scintillating fiber tracker with the end view of the fibers.

$\sim 9°$ K.

3.4.4 Central and Forward Preshower Detectors

Preshower detectors (Central Preshower (CPS) and Forward Preshower (FPS)) lay just beyond the tracking system and they were designed for the Run II upgrade to aid electron and photon identification and triggering. Both are based on a similar scintillator technology as the CFT. They provide early energy sampling for particles just traveled through the solenoid (CPS) or lead converter (FPS), an important step to the correction of the electromagnetic energy due to the effects of the un-instrumented solenoid and converter material.

In the central region is the CPS [27, 35] that functions both as a calorimeter (by early energy sampling) and as a tracker (by providing precise position measurements). The cylindrical detector is placed in the 51 mm gap between the solenoid coil and the central calorimeter cryostat at a radius of 72 cm, and covers the region $-1.2 < \eta < 1.2$. The detector consists of three layers of scintillating strips arranged in axial and stereo views. The innermost layer is an axially arranged layer, while the two outer layers are arranged at in a u, v-stereo configuration with $\pm 23°$ crossing angles. The scintillating strips have a triangular cross section with a 7 mm base and a 1 mm diameter hole containing wavelength shifting fiber (WLS) in it. Figure 3.19 shows the the cross-sectional end $(x - y)$ and side $(r - z)$ views of the CPS detector. Light from the WLS fibers is allowed to exit

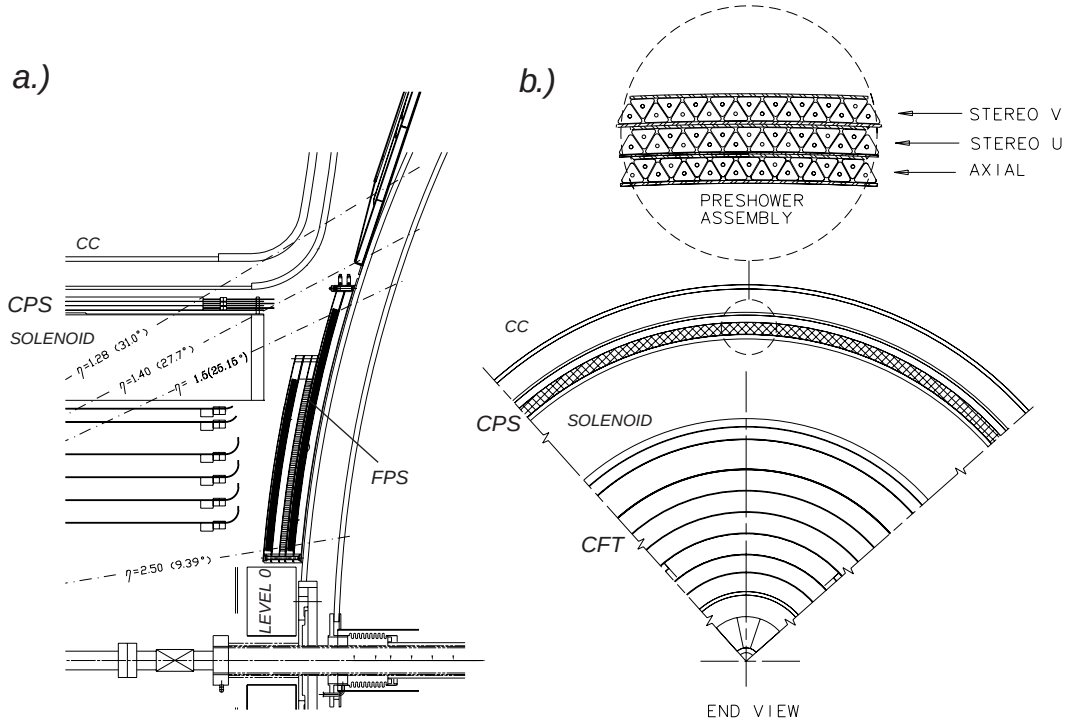

Figure 3.19: $x - y$ and $r - z$ views of the Central Preshower Detector.

through optical connectors similar to the CFT, and is read out by the VLPC's.

The FPS detector is based on the same scintillator technology, and it's the forward region counterpart of the CPS. It covers the $1.4 < |\eta| < 2.5$ region. The FPS detectors are mounted on the inner face of each of the End Calorimeter (EC), as shown in Figure 3.20.

The FPS (and CPS) share the same (VLPC) readout system with the Scintillating Fiber Tracker, which was mentioned in Section 3.4.3.

3.5 Calorimeter System

Calorimeter detectors are devices in which a particle, after interacting with the detector material, loses practically all it's energy by processes which include a stage of ionization or excitation and ultimately result in heat [36]. During these processes, cascades of interactions occur, which are called showers. Although most of the energy of the particle is converted into heat there is a part of the energy which is released in the form of the recordable signal such as scintillating light or ionization.

One great difference of the calorimeter subsystem comparing to the other sub-detectors, is that

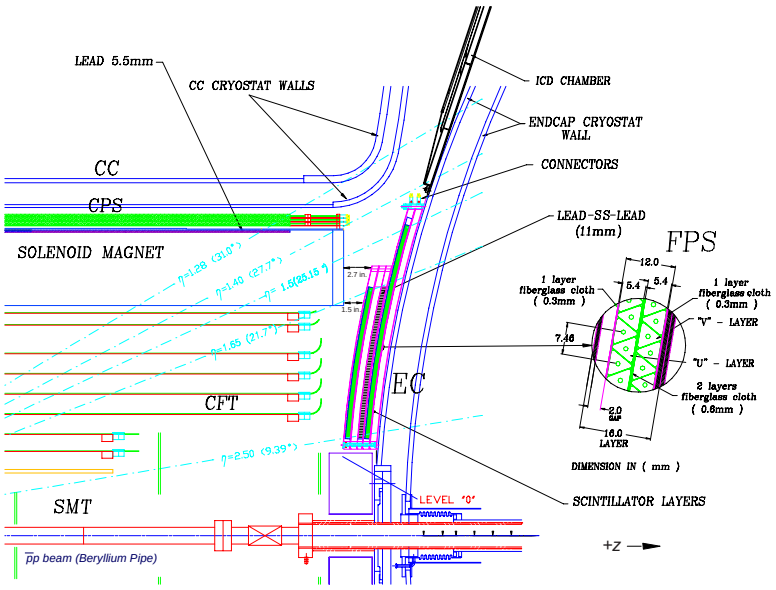

Figure 3.20: Location of Forward Preshower Detector in the DØ Detector

since the particle loses all, or at least a large fraction, of its energy, it's no longer available for further study (contrary to what happens for example in SMT). For this reason calorimeters are sometimes known as "destructive" detectors, and this a feature that has to be taken into consideration when arranging the various subsystems of a particle detector. Calorimeter detectors are used in high energy physics for:

1. Measurement of the particle's energy;

2. Particle identification;

3. Determination of the decay vertex position (if no tracking information exists).

The characteristics of a calorimeter depend on the nature of the dominant showering process responsible for energy loss. For electrons and γ-rays (photons) the energy loss is dominated by electromagnetic interactions - bremsstrahlung, pair production and Compton scattering. In this case contribution from nuclear interactions is small. For strongly-interacting particles such as mesons and nucleons (hadrons), the dominant process for energy loss is nuclear interactions. Muons, which interact electromagnetically, do not produce showers due to their high mass and also pass through with minimal interaction. Neutrinos, which only interact weakly, pass through the calorimeter leaving no

signal (interpreted as missing transverse energy - $\not\!\!E_T$). Other weakly-interacting neutral particles (yet to be discovered) such as gravitino pass through the calorimeter undetected and their presence would be inferred from the amount of $\not\!\!E_T$ observed in the event. From the above it's obvious that calorimeters fall into two categories:

1. *Electromagnetic calorimeters*: designed to measure electron and γ-ray energies;

2. *Hadronic calorimeters*: designed to measure strongly-interacting particle energies.

It has to be noted here that although hadronic showers are dominated by nuclear interactions, they also contain electromagnetic shower components, making the determination of the hadronic showers more complicated, since the electromagnetic part has to be accounted for differently. These two types of showers differ also in relative size. For a given energy of an incident particle, a hadronic shower tends to be of a larger size than the electromagnetic one. Since the properties of the hadronic and electromagnetic showers is very important part of this analysis we will review them in some detail in this chapter. The different depth (in the radially outward direction) for the two types of showers is reflected in the design of the calorimeters for a general purpose collider detector. The calorimeter consists of two sub-detectors: the electromagnetic calorimeter and the hadronic calorimeter. The electromagnetic calorimeter is the innermost calorimeter and is more compact; it encloses the volume closer to the interaction point (after the tracking system in the radially outward direction) while the hadronic calorimeter is the outermost of the two covering the outer region of the detector. Although the above design of the calorimeter is optimized for both types of showers, there are still some difficulties affecting the energy measurement of the showers. The first is that the electromagnetic content of the hadronic shower fluctuates in energy. The second is that most of the hadronic energy is converted into excitation or break-up of the nuclei, from which only a fraction will result in detectable ('visible') energy. The above two difficulties affect the e/h ratio (the ratio of electromagnetic and hadronic response), and as a result this ratio is not equal to one. To improve calorimeter performance, attempts have been made to make it as close to one as possible by means of *compensation*. The main idea was to use uranium as the absorber material [36]; this would contribute an additional, i.e. compensating signal due to nuclear fission caused by nuclear

excitation. The DØ Calorimeter is a compensating calorimeter with $e/h = 1 \pm 0.02$.

Since the shower development is for the most part independent of the charge of the incident particle, calorimeters also are unique instruments for measuring energy of neutral particles. They also can be used for detecting and measuring particle jets, in which mixtures of neutral and charged particles are present at small spatial separation.

From the construction point of view there are two types of calorimeters:

1. Homogeneous calorimeters;

2. Sampling calorimeters (heterogeneous).

In *homogeneous* calorimeters both the function of absorption and signal creation is carried by the same material, typically a pure or doped heavy crystal (like NaI or CsI), or a composite material (like lead glass). Their main disadvantage is the fact that, is very difficult to grow and machine large homogeneous crystals. They are, therefore, mostly used for moderate energy electromagnetic calorimetry (small shower size), for which a high precision measurement is required.

In *sampling* calorimeters, the absorber and signal creation materials are different. The absorber material is inactive and interspersed with layers of signal-producing material (active), typically liquid or solid scintillator. Inactive materials typically used are lead, iron, copper, uranium, or combination thereof. The ratio of energy loss in active and inactive material typically is of the order of 1:10. If the sampling of a signal contains adequate detail of the absorption process, the original phenomenon can be inferred from it, allowing the reconstruction of the energy dissipation profile during the shower development.

In the following section we will take a closer look at the DØ calorimeter.

3.5.1 DØ Calorimeter

The DØ Calorimeter is a compensating sampling calorimeter using liquid argon (LAr) as the active sampling medium and depleted uranium (DU) as well as copper and steel as the absorber material [20, 21, 37]. For the active material LAr was chosen for several reasons: a) it provides uniform gain over the entire calorimeter, allowing for a channel-to-channel response stable over time and

dependent on gap and absorber thickness, b) is highly flexible in segmenting the calorimeter volume into readout cells, c) is radiation hard, d) is easy to calibrate. For the absorber material DU was chosen because due to its high density allows for a compact and inexpensive detector, while also improves the e/h ratio. The need to operate the calorimeter at liquid argon temperatures, along with construction and installation needs (access to the Central Detectors), dictates that the Central Calorimeter (CC) must exist as a separate module from each of the two End Calorimeters (EC-North and EC-South). Each of the three modules (CC, EC-North and EC-South), is placed inside of it's own containment vessel (cryostat). The solution that was chosen by DØ is shown schematically [22] in Figure 3.21.

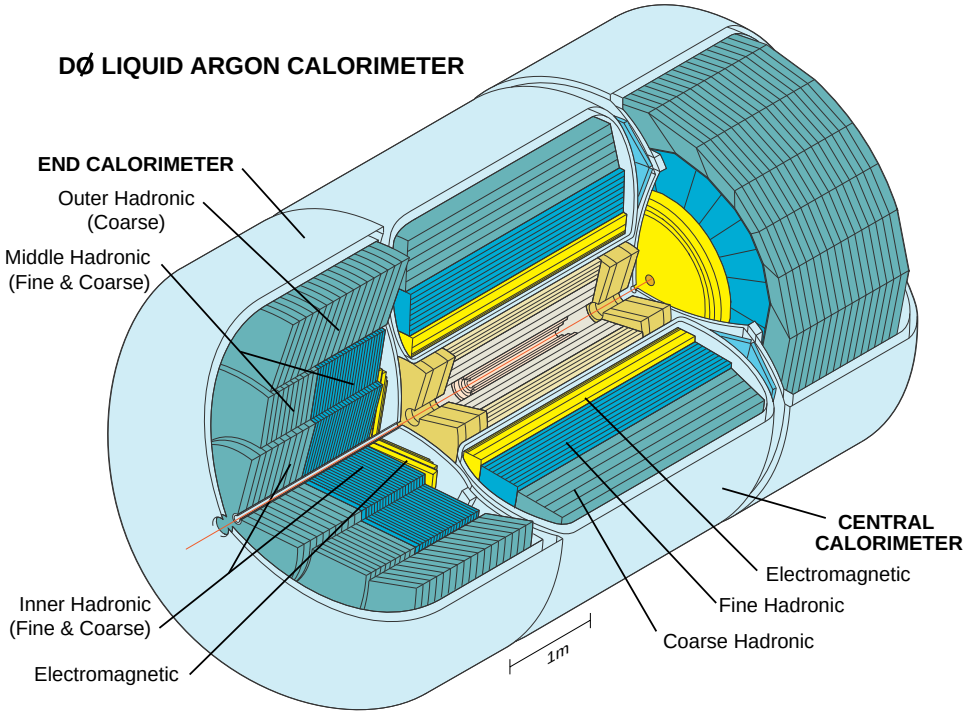

Figure 3.21: DØ Calorimeter.

From these modules the CC covers roughly the $|\Delta\eta| \leq 1.2$ region and each of the End Calorimeters (EC North and EC South), extend the η coverage out to $|\eta| \approx 4.5$. The boundary between CC and EC was chosen to be approximately perpendicular to the beam direction. This choice was shown to introduce less degradation in the missing transverse energy measurement. The dimensions

of the calorimeters are based on the requirement to adequate contain the shower energy. In addition, since the calorimeters are embedded in a multi-detector system, the following factors must be taken into consideration:

- the need for sufficient tracking coverage in front (inside) of the calorimeter;
- the requirements of magnetic measurement of muon momenta outside the calorimeter;
- the size of the experimental hall.

The resulting design has three distinct types of modules in both CC and EC:

1. electromagnetic section (EM) with relatively thin uranium absorber plates;
2. fine-hadronic section (FH) with thicker uranium plates;
3. coarse-hadronic section (CH) with thick copper or stainless steel plates.

The EM calorimeter is 21 radiation lengths deep and consists of four separate floors EM1, EM2, EM3, EM4. These are radial floors for the CC and z-floors for the EC (see section 3.3 for the DØ coordinate system). Each absorber plate is 3 mm (CC) or 4 mm (EC) thick nearly pure depleted uranium [38]. The FH modules consist of three or four layers that have 6 mm thick uranium-niobium (2%) alloy absorber plates. The outer CH section has only one layer that uses relatively thick (46.5 mm) plates of either copper (CC) or stainless steel (EC).

The depth of each layer for the three calorimeter sections is shown in Table 3.1 in the units of *radiation length* X_0 and *absorption length* λ [39].

	EM	FH	CH
CC Depth	$2, 2, 7, 10\ X_0$	$1.3, 1.0, 0.9\lambda$	3.2λ
EC Depth	$0.3, 2.6, 7.9, 9.3\ X_0$	$1.2, 1.2, 1.2\lambda$	3.6λ

Table 3.1: The depth of the calorimeter layers.

From the readout point of view each layer represents a discrete set of *readout cells*. A typical transverse sizes of a cell are $\Delta\eta = 0.1$ and $\Delta\phi = 2\pi/64 \approx 0.1$ (the EM3 layer, however, is twice

as finely segmented in both η and ϕ to allow for more precise location of the EM shower centroid). A set of cells (one cell from each layer) that are aligned along the outward direction (approximate direction of a shower development) constitute a *tower*. The readout tower geometry is shown in Figure 3.22. This is a 'pseudo-projective' geometry. The term 'pseudo-projective' refers to the fact

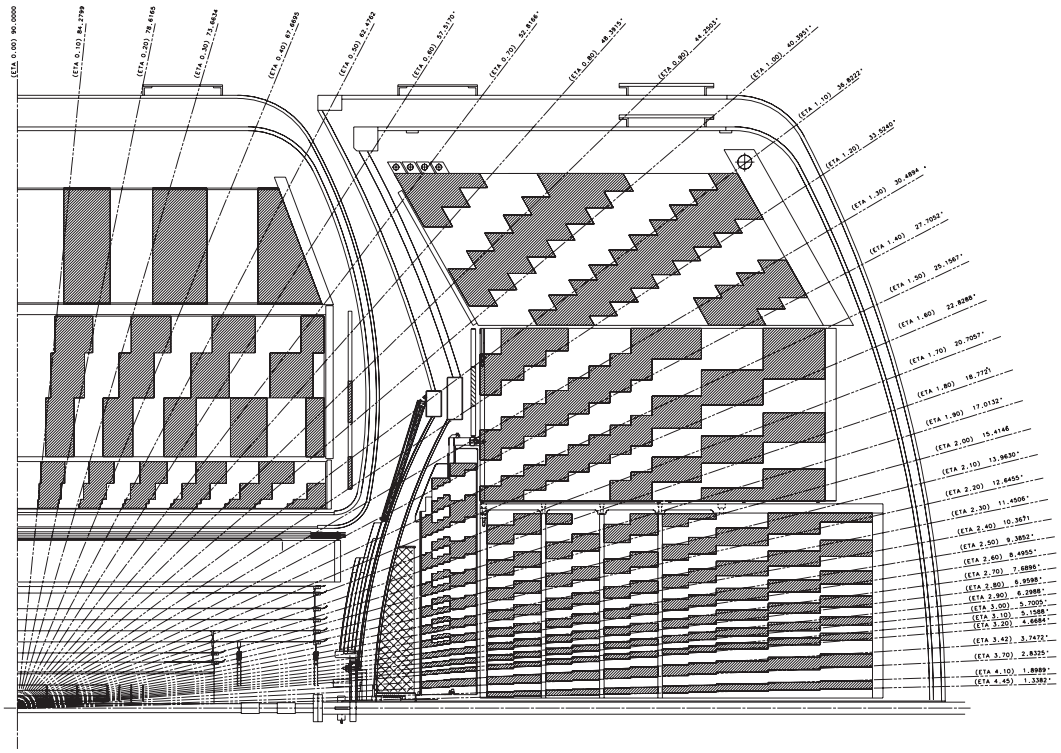

Figure 3.22: Pseudo-projective geometry of the DØ Calorimeter.

that the centers of cells of increasing shower depth lie on the rays projecting from the center of the detector, but the cell boundaries are aligned perpendicular to the absorber plates.

A cell (*readout cell*) is a combination of several adjacent *unit cells*. A schematic view of the calorimeter *unit cell* [4] is shown in Figure 3.23. The gap between the adjacent absorber plates is filled with a 2.3 mm LAr. The electron-ion pairs created via the ionization of the liquid argon by charged particles from a shower are collected by the electrodes in the presence of a strong electric field. Metal absorbers are used as ground electrodes (cathodes), and the readout boards at +2.0 to 2.5 kV, located in the center of the gaps, serve as anodes.

The signal boards are printed circuit boards made of two 0.5 mm thick layers of G10 plastic sandwiching copper-clad readout pads; the outer surface of the circuit boards is coated with a

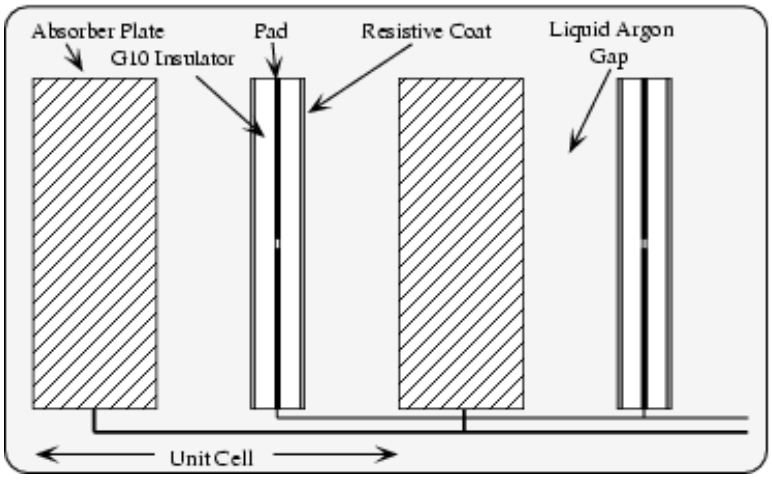

Figure 3.23: Calorimeter unit cell.

resistive epoxy coating. High voltage is applied to the entire resistive coat, and the charge collection in this coat induces a charge on the copper readout pads via capacitive coupling. To detect signals that can be very small, several pads are ganged together in depth to form a *readout cell*. The electronics receives an analog signal from a readout cell which is proportional to the energy deposited by the shower in the active media [40]. The simplified calorimeter data flow path diagram is shown in Figure 3.24 and in a more detailed diagram in Figure 3.25. Coaxial cables carry the signal to a

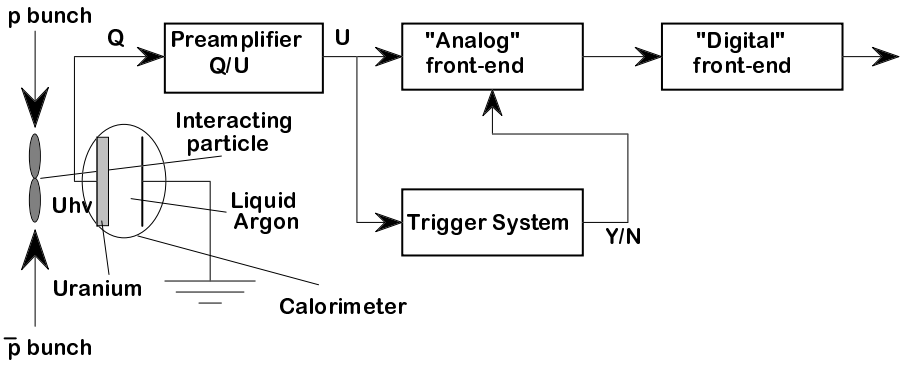

Figure 3.24: Simplified calorimeter data flow diagram.

feed-through port, which allows to pass it through the cryostat. The feed-through boards reorganize signal form the module-structure scheme to the physics scheme in which the readout channels are

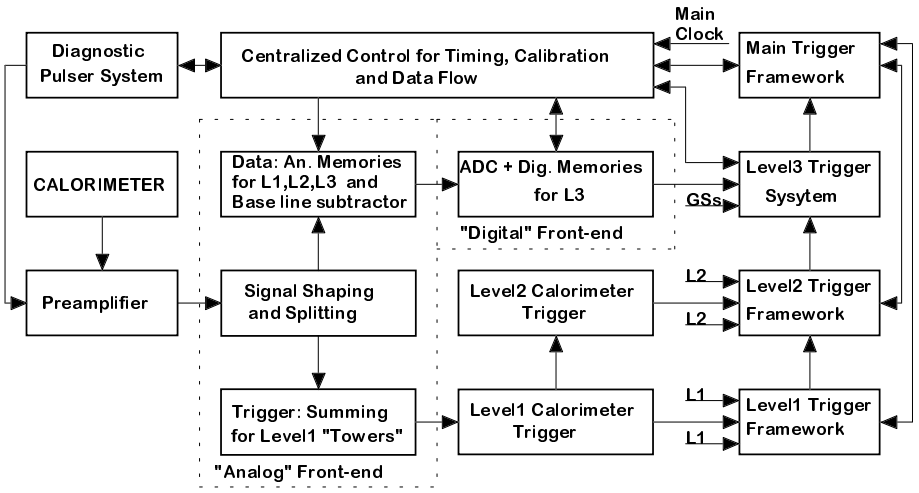

Figure 3.25: Full calorimeter data flow diagram.

arranged in the pseudo-projective $\eta - \phi$ towers [29]. The calorimeter channel configuration is shown in Figure 3.26. The signal is then conducted to the charge-sensitive preamplifiers. The preamplifiers integrate the pulse over time to produce proportional voltages. The preamplifier outputs go through 30 meter coaxial cables to the signal shapers. After the signal is shaped, the data flow splits in two paths. One path takes the data to the Level 1 calorimeter trigger. Another (the precision readout) path leads to the baseline subtraction system (BLS). The BLS performs the cell signal sampling just before and after the beam crossing and takes the difference between the two. This is done in order to separate the signal coming from the event to be recorded from the noise as well as previous collision remnants. The baseline-subtracted output is stored in a "sample and hold" circuit. Following the trigger decision to keep the event, "sample and hold" outputs are read out and digitized by the Analog-to-Digital Converters (ADC). The digitized signal from the calorimeter is then merged with the signal information from the other detector systems to form an *event*.

The performance of the DØ calorimeter has been studied extensively in the past in test beams as well as during the Run I period [41, 42, 43, 44]. It's response to electrons and pions has been observed to be linear. The energy resolution of the calorimeter is parameterized as:

$$\left(\frac{\sigma}{E}\right)^2 = C^2 + \frac{S^2}{\sqrt{E}} + \frac{N^2}{E} \tag{3.3}$$

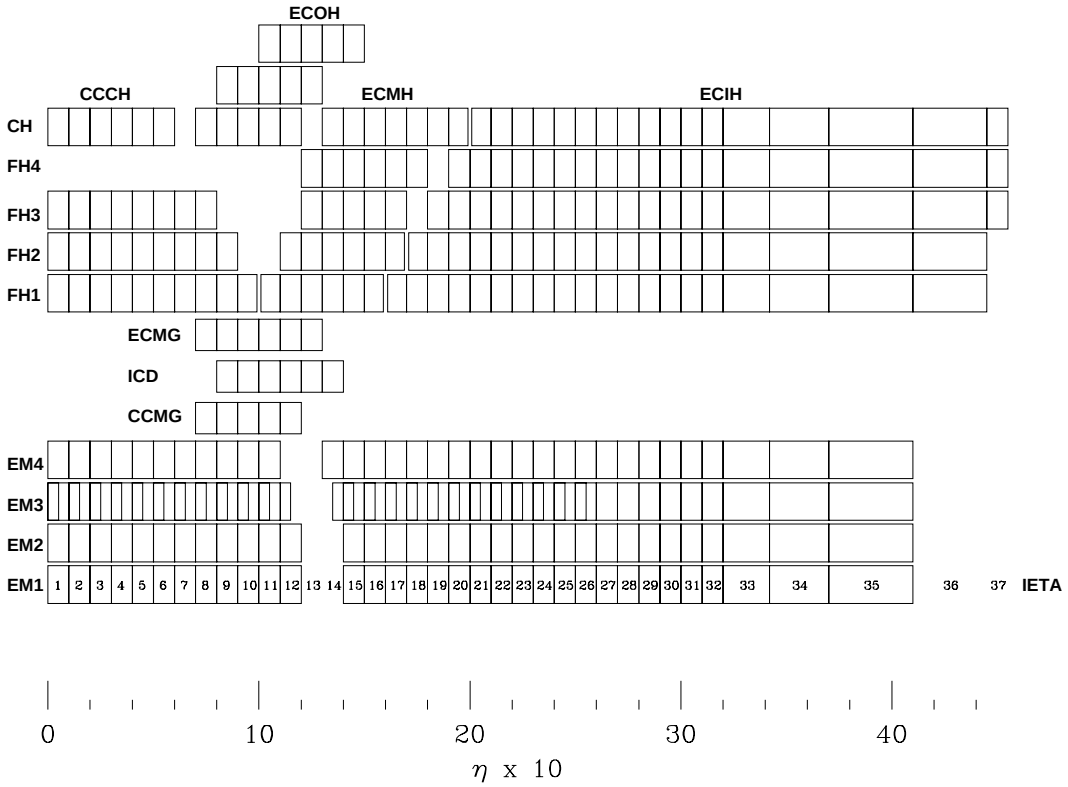

Figure 3.26: Segmentation of the DØ calorimeter towers in terms of depth and η.

where C, S and N denote calibration errors, stochastic fluctuations of shower development, and noise contributions, respectively. The position resolution of the EM calorimeter varies as $1/\sqrt{E}$, while the ratio e/h is typical for it's kind from 1.11 (at 10 GeV) to 1.05 (at 159 GeV).

3.5.2 Intercryostat and Massless Gap Detectors

Particles traversing the region between the EC and CC detectors ($1.1 < |\eta| < 1.4$), will pass through several layers of the CC and EC support structures with a large amount of un-instrumented material as can been in Figure 3.22. Most of this material is due to the cryostat walls, calorimeter support, and cabling for the detector readout [39, 20]. To help instrument this region, scintillation detectors have been mounted on each of the EC cryostat walls, facing the gap. Each inter-cryostat detector (ICD) (*i.e.,* north or south) consists of 16 trapezoidal-wedges, 22.5° in ϕ with a total of 384 scintillator tiles of size $\Delta\eta = \Delta\phi = 0.1$ exactly matching the calorimeter cells. The tiles carry a WLS fiber which transmits light via an optical connector to photomultipliers located outside the EC walls.

In addition separate single-cell structures, called massless gaps, are installed in both CC and EC calorimeters. Together, the ICD and massless gaps provide a good approximation to the standard DØ sampling of hadron showers. Much of the readout electronics for the ICD is similar to that of the DØ calorimeters.

3.5.3 Luminosity and the Luminosity Monitor

In high-energy physics, many measurements relevant to a physical process are expressed in terms of a variable characterizing this process, the cross section σ. This variable can be calculated from theory for each physical process (and compared with experimental data), and corresponds to the interaction probability per unit flux for this process. In high-energy physics the basic unit for cross section is 1 barn = 10^{-24}cm^2. In any collider experiment, particle flux comes from the colliding beams and it's called instantaneous luminosity, $\mathcal{L}$. Luminosity is proportional to the product of the number of particles in each beam passing through a unit area per unit time, and it is expressed in units of $\text{cm}^{-2}\text{s}^{-1}$. Using the luminosity and the cross section the rate for a given process is:

$$R = \sigma\mathcal{L} \tag{3.4}$$

where R is in Hertz (Hz). Usually the quantity we are interested in is the total number of expected events, N, for a specific process. The following expression defines the number of expected events for a process with cross section σ:

$$N = \sigma \int \mathcal{L}dt\,, \tag{3.5}$$

where the quantity $\int \mathcal{L}dt$ is the luminosity integrated over time and it is referred to as integrated luminosity, and is measured in units of inverse barns. It is obvious from the above that instantaneous luminosity monitoring is an important issue for any collider experiment, since precise cross section measurements rely completely on the known integrated luminosity of the data sample [4].

The DØ Luminosity Monitor in Run II consists of two hodoscopes of scintillation pixels mounted on the faces of the end cryostats [27]. The layout, location, and some relevant parameters [45] of

the Luminosity Monitor are shown in Fig. 3.27.

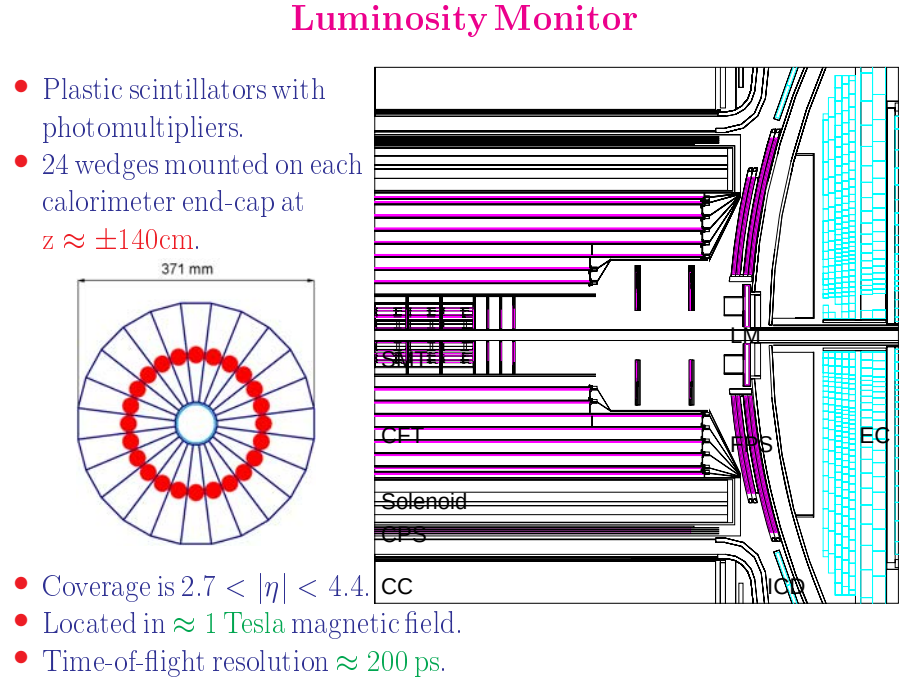

Figure 3.27: DØ Luminosity Monitor.

Light coming from the scintillators is read out using photomultiplier tubes. These counters detect non-diffractive[2] inelastic collisions with high efficiency. The rate of these collisions is used for determining the luminosity. In addition, the luminosity monitor acts as a tool that provides diagnostic information regarding the accelerator performance and also can be used to help identify the number of interactions per beam crossing [46, 47, 48]. The Tevatron integrated luminosity over time, for the period March 2001 - September 2004, is shown in Fig. 3.28.

It has to be noted here that, the above figure shows the *delivered integrated luminosity*. The *recorded integrated luminosity* from the DAQ system, available for physics studies, is less than the above due to sub-detector and trigger inefficiencies, and dead time.

[2]In *diffractive $p\bar{p}$ scattering* nucleon substructure is not revealed , i.e. it is a nucleon-nucleon scattering. *Non-diffractive scattering* one the other hand is a scattering in which both scattering participant is a nucleon constituent (a quark or a gluon).

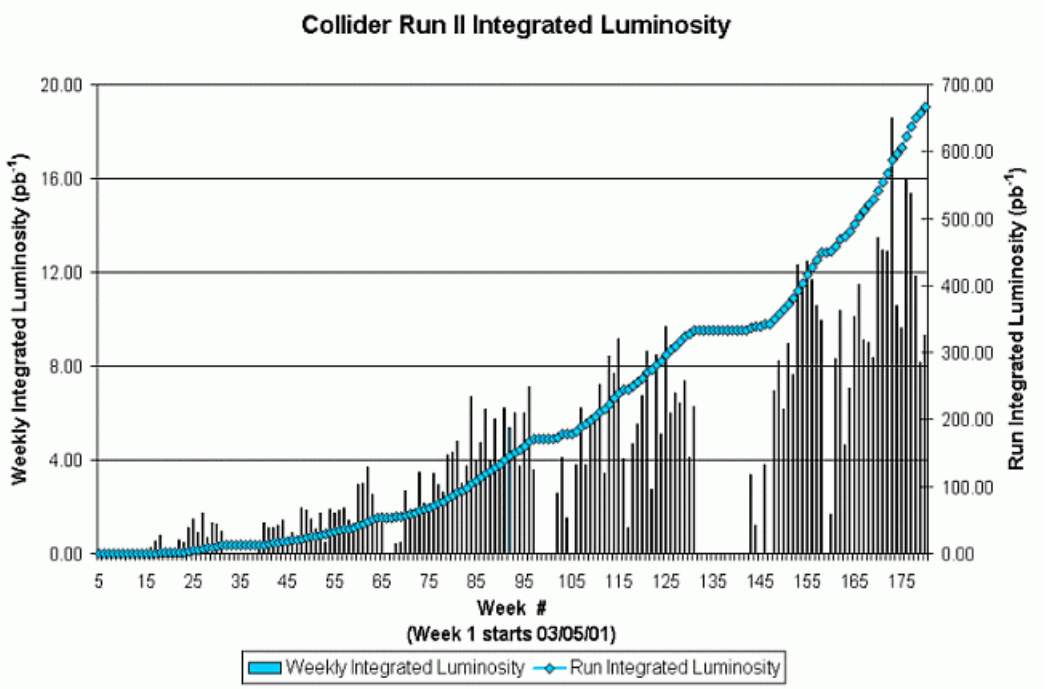

Figure 3.28: Collider Integrated Luminosity delivered to DØ in Run II [49].

3.5.4 Muon System

Muons, being much heavier than electrons, typically do not lose much energy via bremsstrahlung [4] i.e., they do not readily initiate electromagnetic showers at the Tevatron energies. Thus muons above some energy threshold ($\approx$ 3.5 - 5.0 GeV) can pass through the entire DØ detector, and their energy loss mostly occurs due to ionization of the detector media which is a low energy-loss absorption process. Because of this property muon system is typically the outermost detector system. Being located outside the calorimeter the muon system is well protected from the debris from the hadronic and electromagnetic showers by the thick calorimeter material. The purpose of the muon system is identification of muons and independent measurement of their momenta in the toroidal magnetic field. During the Run I phase this was the only way to determine the muon momenta, currently in Run II the existence of the 2 Tesla magnetic field in the central region along with the tracking system provides a second independent way. In this analysis the muon system is not used, therefore only a very brief description will be made, however, it is crucial for many physics topics covered by DØ, including extra dimension searches, Higgs searches in the WW and $b\bar{b}$ decay modes. The DØ

muon system is shown in Figure 3.29 [22].

It consists from three major components [40]:

- Wide Angle MUon Spectrometer (WAMUS) covering $|\eta| < 1$;
- Forward Angle MUon Spectrometer (FAMUS) covering $1 < |\eta| < 2$;
- Solid-iron magnet creating toroidal field of 1.8 T.

The WAMUS consists of three detection layers as shown in Figure 3.29, increasing radially outwards and labeled as A, B and C. Between layers A and B, C there is a 1.8 T toroid field. Each layer within the WAMUS has two types of detectors: proportional drift tubes (PDT) and scintillators. The tubes are 10.1 cm across and 5.5 cm high, with around twenty-four of them making a chamber. They use a gas mixture of 80% argon, 10% CH_4, and 10% CF_4 [27]. When operated at a voltage of 2.5 kV for the pads and 5.0 kV for the wires, the drift velocity in this gas is around 10cm/μs, with a maximum drift time of 500 ns. The scintillators for the WAMUS are broken in two categories, the A-ϕ counters (that cover the A-layer PDT's), and the Cosmic Caps (located outside the B-layer and C-layer PDT's). The timing resolution for the A-ϕ scintillators is $\sim$ 4 ns, while for the Cosmic Cap scintillators is $\sim$ 5 ns, which can be improved by off-line corrections to about 2.5 ns.

The FAMUS has a similar structure, it consists from three layers as shown in Figure 3.29 labeled A, B and C and each layers made of a combination of two types of detectors Iarocci mini drift tubes (MDT) and scintillation pixel counters. Figures 3.30 and 3.31 illustrate the $\rho - \phi$ view of the MDT's and the scintillator pixel counters.

The muon system also contains a series of 50 cm thick iron and 15 cm thick polyethylene shielding with 5 cm thick lead skins, designed to reduce backgrounds from interactions of the beam with the quadrupole magnets and beam pipe.

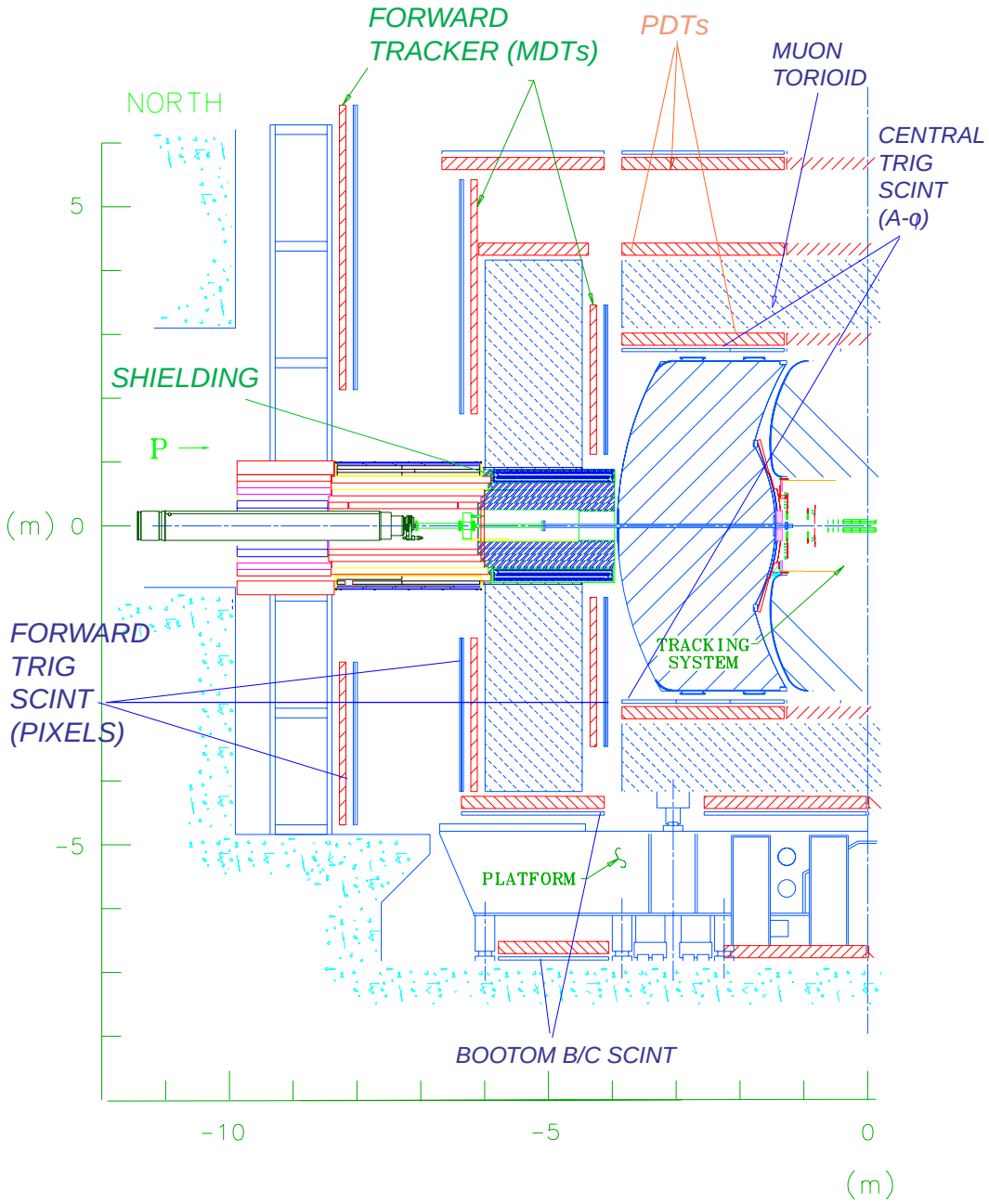

Figure 3.29: DØ muon detection system.

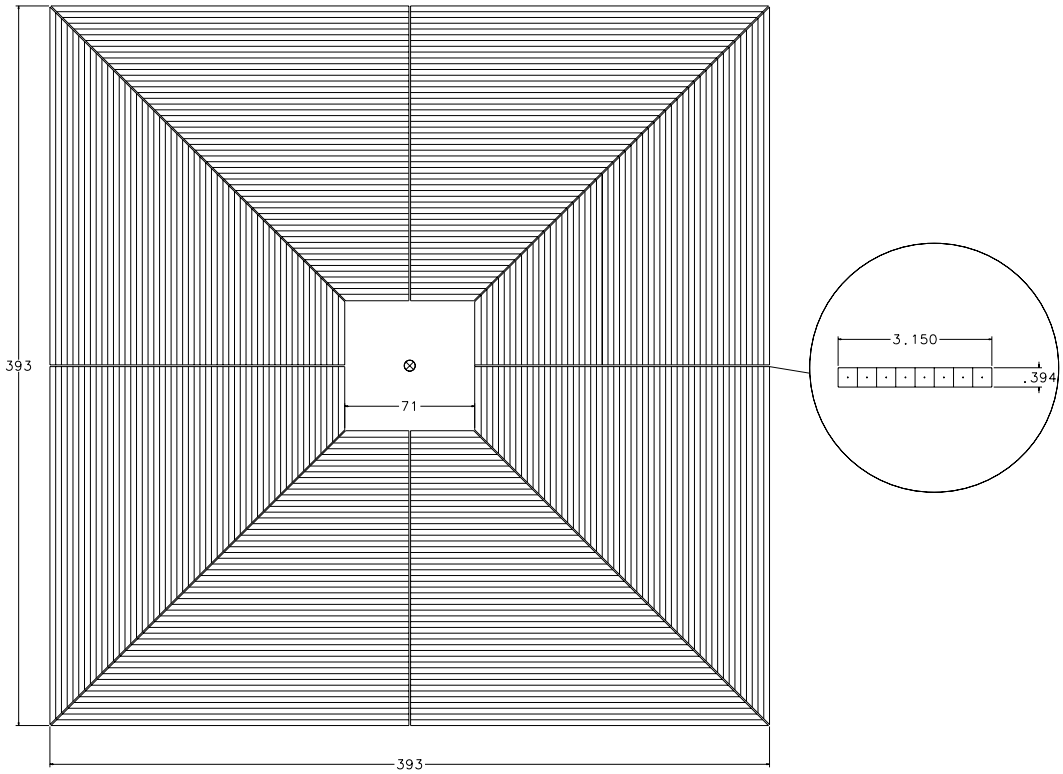

Figure 3.30: Shown here is the $\rho - \phi$ view of one plane of the MDT's. The insert shows the cross section of a single Iarocci tube

3.6 Forward Proton Detector

The Forward Proton Detector (FPD) was designed to study non-perturbative (*i.e.*, low-p_T) QCD phenomena of elastic and diffractive $p\bar{p}$ scattering [50]. It consists of a series of spectrometers located on both sides of the DØ interaction region, about 30 m away form the center of the detector. To allow the detector to function close to the beam, each spectrometer (a scintillating fiber detector) is placed in a stainless steel container (*Roman pot*). The pots allow the entrance and exit of protons through thin windows and they are remotely controlled so they can be moved close to the beam (within a few mm) during stable beam conditions and retracted otherwise. The detectors measure the (x,y) position of a deflected proton (or anti-proton) track at the pot position. This information is used for measuring proton scattering angle and its momentum. For the momentum measurement magnetic field created by the Tevatron magnets is used. The FPD has not been used in this analysis since the signature of interest occurs mainly in the central part of the detector.

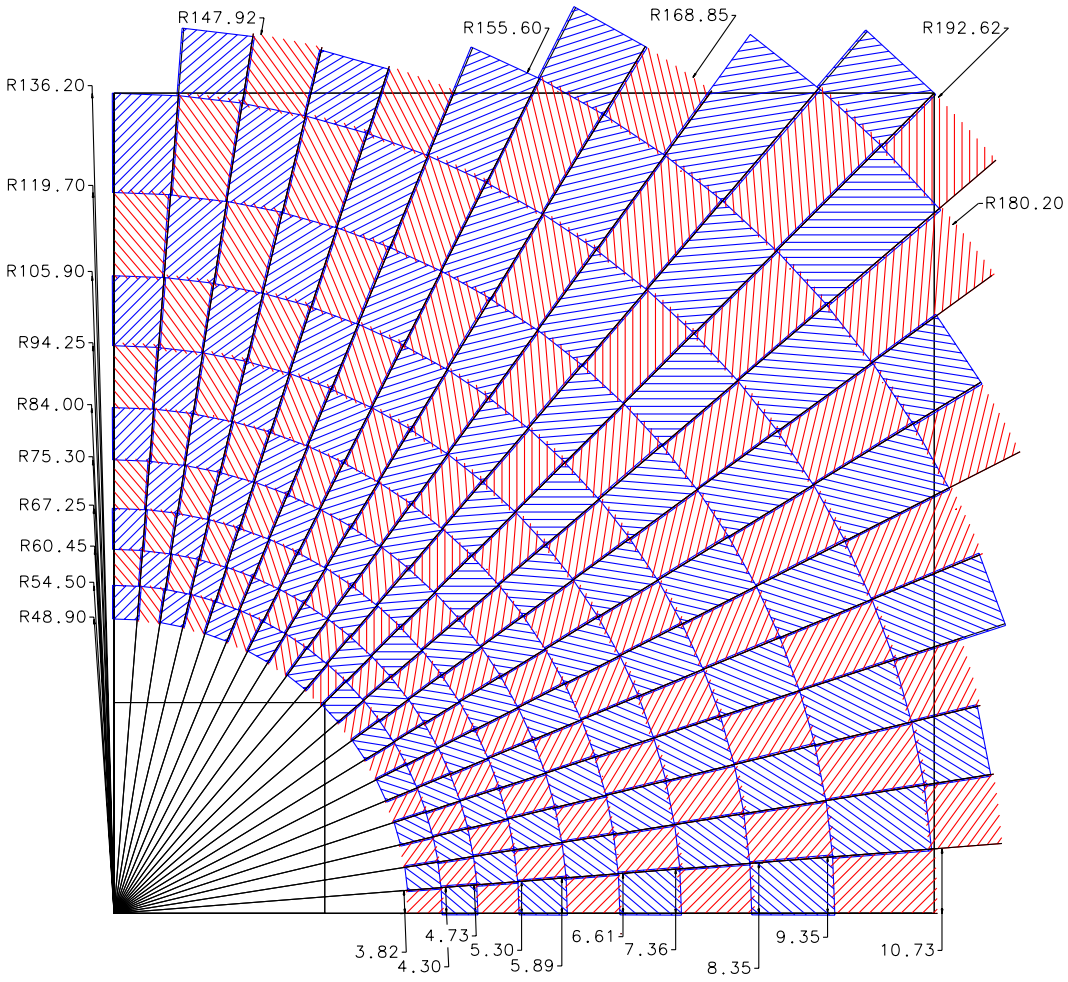

Figure 3.31: An $\rho - \phi$ view of the scintillator pixel counters.

3.7 Trigger and Data Acquisition Systems (DAQ)

For Hadron collider experiments only a few events in a million are of some physics interest. Most of the collisions are just low-p_T non-diffractive $p\bar{p}$ scattering and parton scattering events. These processes have been thoroughly studied in the past, thus making these events less interesting for studies at DØ . Collecting all the events produced from the collisions (and filter them later to isolate the few interesting events for physics studies) is not only unpractical but also simply impossible. The high luminosity ($\mathcal{L} = 10^{32} cm^{-2} s^{-1}$) , and high rate (2.5 MHz or 396 ns beam crossing) environment in Run II exceeds by far the rate at which event processing and recording can be performed. Hence, most of the non-interesting events must be discarded, leaving as many as possible interesting events which should be recorded for further analysis. This type of selection is referred to as *triggering*, and a summary of this selection process in DØ is given below. Triggering is a decision process that looks at the coarse detector information in the event and quickly decides whether to keep or reject it, according to a specified pattern that corresponds to a particular type of event. The very limited time interval in which a trigger makes its decision, leads to the following problem when more than one triggers are used simultaneously. The number of events that is accepted by one trigger can be many times larger than the number of events accepted by a second trigger. Attempting to write all these events on tape would be impossible due to the limited rate at which events can be recorded on tape. In order to deal with this problem, a fixed acceptance rate can be imposed beforehand to the high-rate trigger suppressing (scaling-down) its rate. This part of the selection process is referred to as *prescaling*. By tuning the trigger (and/or the prescales) carefully, we can assure that a high proportion of the recorded events on tape are of physics interest. The DØ trigger framework is organized into three main levels (L1, L2, L3) of increasingly sophisticated event selection and decreasing output rate [4]. At L1 and L2, a decision is made based on the raw detector information and simple algorithms in Field Programmable Gate Arrays (FPGA's) on specialized microprocessors. The FPGA's are hardware devices allowing L1 and L2 (that are forced to work at a relatively high rate), to make decisions very quickly. The L3 uses software filtering algorithms running on a set of high performance processors. It makes more "intelligent" decisions than that of the first two trigger

levels and works with a much lower rate. After a decision is made from the above three levels to keep or discard an event, the event is sent to the Data Acquisition System (DAQ) and then moved to storage tapes. The overall DØ trigger scheme is shown in Figure 3.32 [22], which indicates the

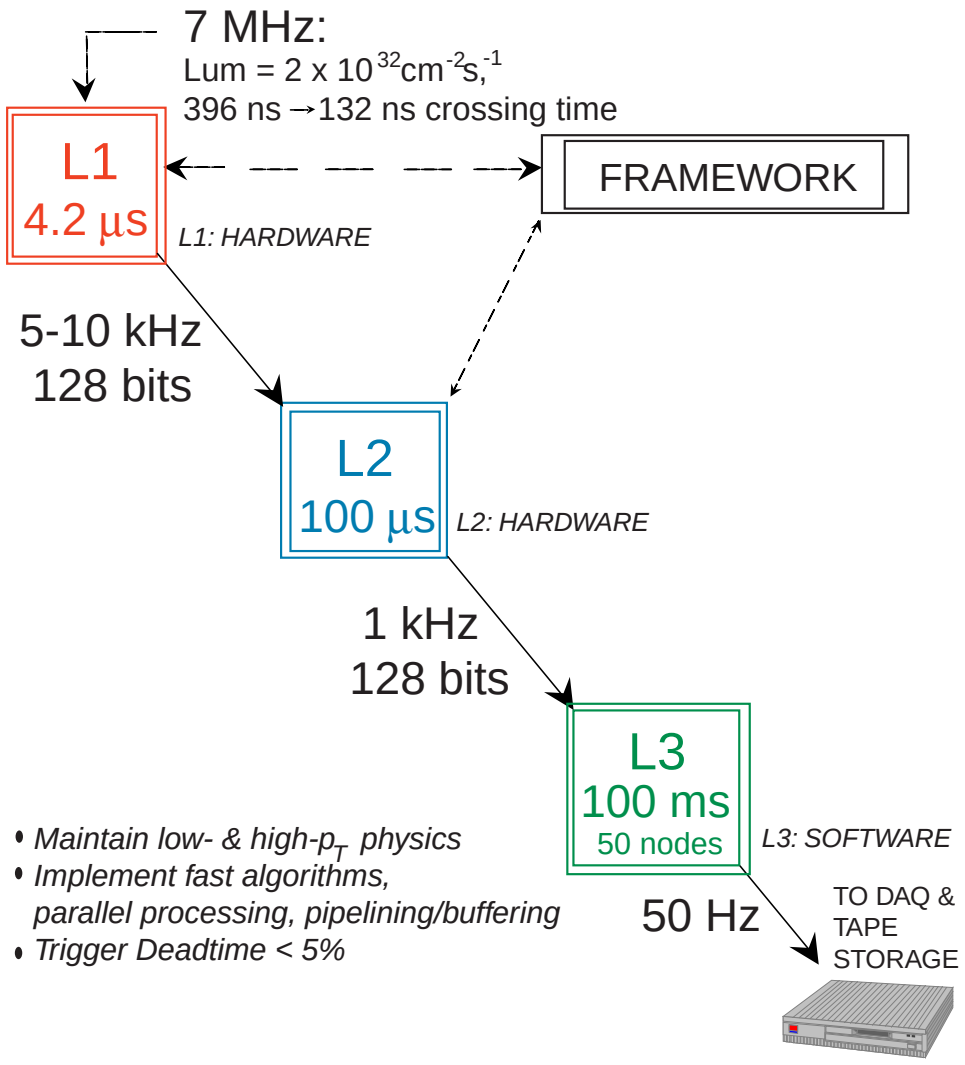

Figure 3.32: DØ trigger scheme layout and typical trigger rates.

event rate at each stage. For example, the input rate into the trigger system (collision rate) is 2.5 MHz (with a maximum of 7 MHz at 132 ns bunch crossing) while the L3 output rate is $\sim$ 50 Hz. Thus, the reduction in the event rate due to the trigger selection is of the order of a million. In the next sections we will look into some details for these three levels of the trigger system.

3.7.1 DØ Level 1 Trigger

Level one trigger (L1) is a hardware system that compiles a list of candidate events based on information obtained from the CFT, Preshower detectors, Calorimeter, and Muon scintillation counters as shown in Figure 3.33 [22]. Each L1 processor examines the corresponding detector system (in

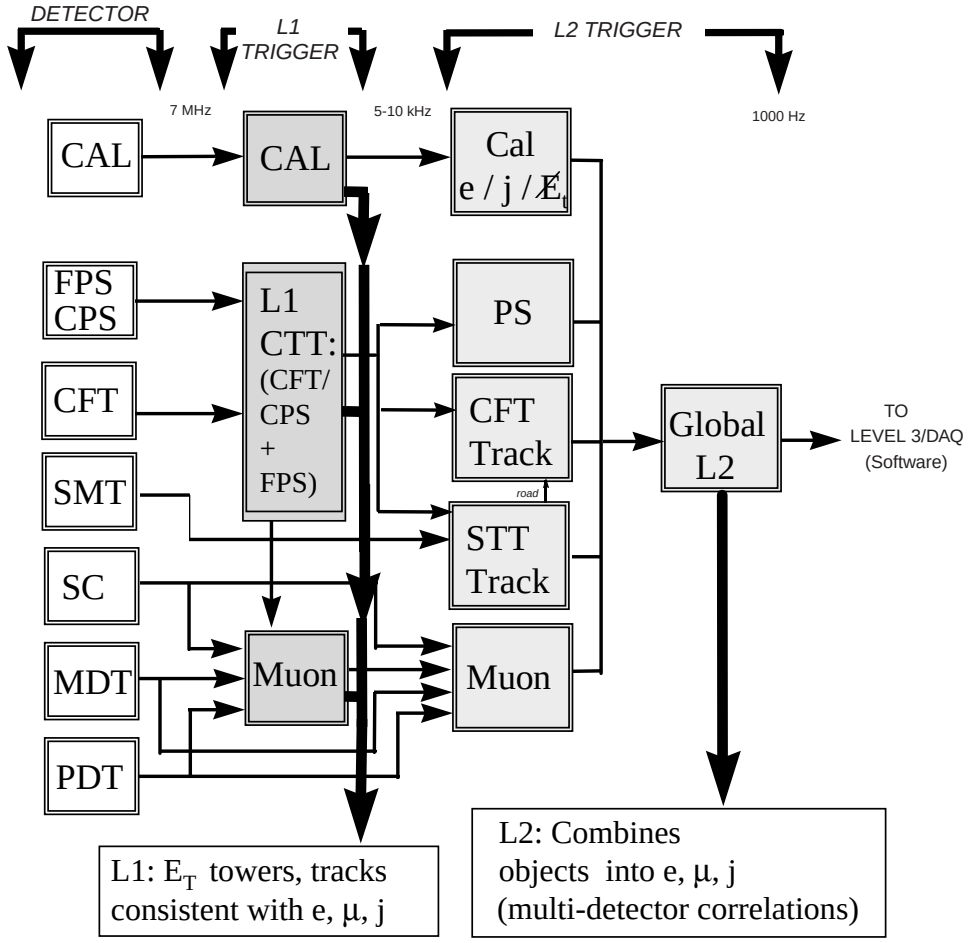

Figure 3.33: The L1 and L2 trigger data flow path.

parallel with the others) on the basis of trigger terms. A trigger term for example can include the candidate's a) trigger tower E_T above some threshold, total energy, and missing E_T; b) energy deposition above some threshold, track isolation and match in the preshowers; c) hit pattern in the CFT consistent with the track momentum above a threshold, etc. Each trigger term specifies that a condition required from the trigger has been met for this event. These decisions from the individual L1 processors are than send to the L1 Framework (L1FW) capable of supporting many unique L1

trigger bits. The L1FW based on a set of specific combinations of trigger terms makes a final global L1 decision, which in turn is passed to the L2 system.

3.7.2 DØ Level 2 Trigger

The level two system (L2) is a hardware system, that correlates the L1 trigger information (from each of the subsystems) in two stages, the preprocessor stage and the global processor stage. At the first stage a list of trigger objects is build (in parallel) using correlation algorithms and the L1 detector-specific trigger information, for example correlation of the calorimeter energy deposition and the rapidity of an electron in the central tracker. The above list of trigger objects is then fed to the second stage, the global processor via serial data highways of 128-bit wide data buses "Magic Bus, MBus" as shown in Figure 3.34 [22]. The global processor compiles the correlations between the

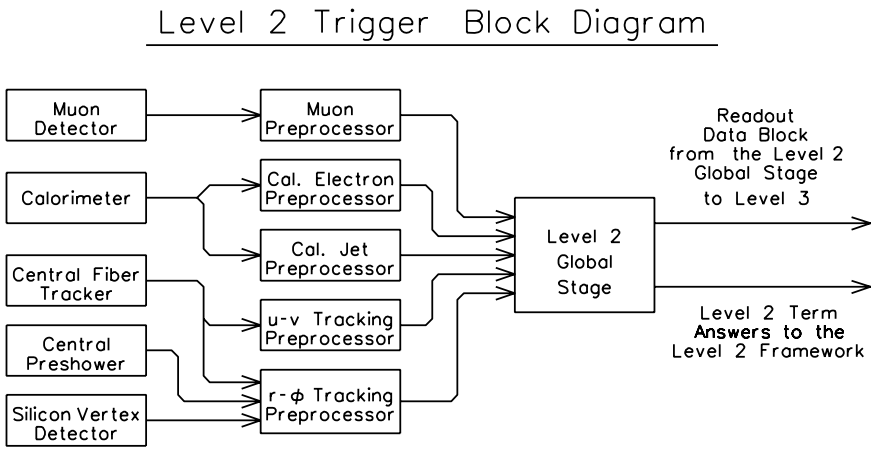

Figure 3.34: The L2 configuration.

various detector subsystems to form measurable quantities, based on algorithms that select distinct physics signatures of interest. At the last stage, as with L1, the output is fed to the L2 Framework (L2FW), which uses the same FPGA's logic as the L1FW to make trigger decisions for L3.

3.7.3 DØ Level 3 Trigger and DAQ

In contrast with L1 and L2, the level three trigger (L3) and data acquisition system (DAQ) is a software based selection system. Hardware-wise it is implemented with a set of high-performance processors operating under a LINUX environment, each one running an independent instance of the L3 filtering software [51, 52, 53]. The Level 3 trigger combines and partially reconstructs full data for each event [52]; each event is analyzed by a different processor to accommodate the high event rate of L2 and also to ensure a high degree of reliability. A diagram of the L3/DAQ system is shown in Figure 3.35 [53].

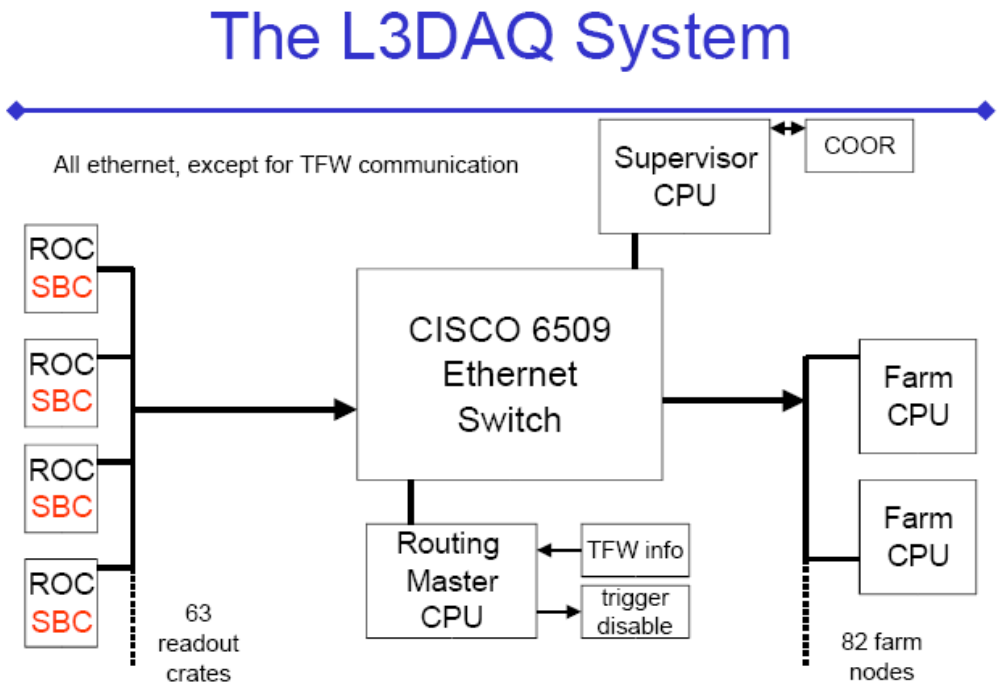

Figure 3.35: The L3/DAQ system layout.

The data flow in parallel out of about 70 VME readout crates (ROC), each corresponding to a section of a sub-detector system or the trigger framework. Each crate is read out by a Single Board Computer (SBC), powered by a 933 MHz Pentium-III processor with 128 MB of RAM. Data size in each crate is 1-10 kB. The total event size is about 250 kB. The data are moved out of SBC's over the Ethernet via a series of Ethernet connections, which transfer them over to the main switch via a

1Gb/s optical fiber. The farm nodes (processors) receive data fragments through the main switch. A farm node builds a complete event, reconstructs it, and performs physics selection. Finally, events that pass the physics criteria are sent via the network to a collector machine and are eventually written to tape for off-line analysis.

Chapter 4

Reconstruction and Particle ID

In this chapter, we present an overview of the software used for the reconstruction of physics objects from raw data at DØ. The full description of this topic is beyond the purpose of this dissertation, therefore only the reconstruction of the relevant physics objects used in this analysis will be mentioned in the following sections. All this information refers to the production version 14 of the DØ reconstruction program (DØRECO).

4.1 Showers

One of the central parts of this analysis is the reconstruction of the electromagnetic objects (electrons and photons). Because of it's significance, a brief description of electromagnetic and hadronic showers will be presented here.

4.1.1 Electromagnetic Showers

During the passage of a photon and/or an electron (positron) through matter (collectively referring to them as electromagnetic particles in this section), more than one process takes place, resulting in the development of an electromagnetic shower. These processes appear multiple times in a form of a cascade reaction, that expands inside the material volume both in the longitudinal and transverse directions (relatively to the particle momentum). A list of electromagnetic interactions taking place

between the matter and electromagnetic particles is given bellow:

- Bremsstrahlung (breaking photon emission by an electron decelerated in a field of an atom);
- Electron-positron pair production ($\gamma \rightarrow e^+e^-$);
- Compton scattering (photon-electron scattering);
- Coulomb scattering (electron-nucleon scattering);
- Bhabha scattering (electron-positron scattering);
- Möller scattering (electron-electron scattering);
- Photoelectric effect (electron emission from the $\gamma-$irradiated atoms);
- Annihilation ($e^+e^- \rightarrow \mu^+\mu^-, or \rightarrow \gamma\gamma$);
- Rayleigh scattering for photons.

Although all the above processes appear during the passage of the electromagnetic particle through matter (if permitted), their relative contribution to the shower development greatly varies with the energy of the incident particle. Most of the above processes appear (or have significant impact) at low energies. High-energy electrons (positrons) predominantly interact and lose energy in matter by bremsstrahlung, while high-energy photons by e^+e^- pair production. Because of these interactions the energy of the incident particle is expected to drop exponentially, for example for electrons we have:

$$E(x) = E_0 \exp(-x/X_0) \tag{4.1}$$

where E_0 is the initial electron energy and $E(x)$ the average energy after passing through thickness x of the material. The characteristic length X_0 is called *radiation length*. For high-energy electrons, it's the mean distance over which the particle's energy is reduced by $1/e$ via bremsstrahlung as can been seen from the above equation. For high-energy photons it's closely related to the total e^+e^- pair production cross section:

$$\sigma = \frac{7}{9}\left(\frac{A}{X_0 N_A}\right) \tag{4.2}$$

where N_A is Avogadro's number, and A is the atomic mass of the material. Therefore for high-energy photons it's related to the thickness of the traversed material ($\frac{9}{7X_0}$) for which there is probability of $\frac{1}{e}$

for the e^+e^- pair production to occur. Because of the above, the radiation length is the appropriate scale length for describing high-energy electromagnetic cascades. Energy loss as a function of the incident particle's energy is shown in Figs. 4.1 and 4.2 for electrons and photons, respectively [54].

Generally the radiation length X_0 is a function of the atomic mass A and the atomic number Z of

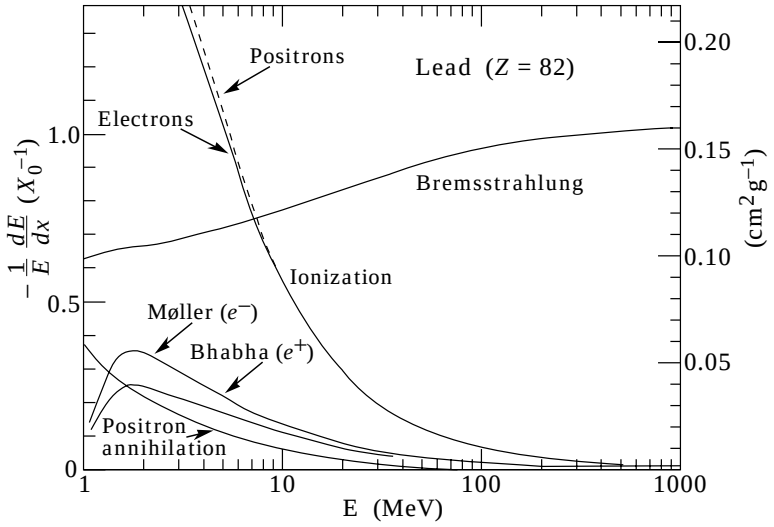

Figure 4.1: Fractional energy loss per radiation length in lead as a function of the electron or positron energy. At high energies bremsstrahlung dominates.

the material; a formula that fits the data for all elements is given by [55]:

$$X_0 = \frac{716.4\ g\ \left(cm^{-2}\right)\ A}{Z\left(Z+1\right)\ \ln\left(287/\sqrt{Z}\right)} \tag{4.3}$$

In order to minimize the overall size of the calorimeter (which is determined from the requirement of the total shower containment), high-Z materials such as uranium are used.

An electromagnetic cascade (shower) is essentially a process in which high-energy electrons or positrons are produced by pair production from high-energy photons, which in turn are produced by bremsstrahlung from high-energy electrons or positrons. This cascading process continues until the average particle energy is no longer high enough to continue the cascade. At this point, other interaction processes take place (ionization and excitation), reducing further the energy of the particles until all energy is absorbed by the detector material. The longitudinal development of the electromagnetic shower is determined by the high-energy part of the cascade, and therefore it scales as the

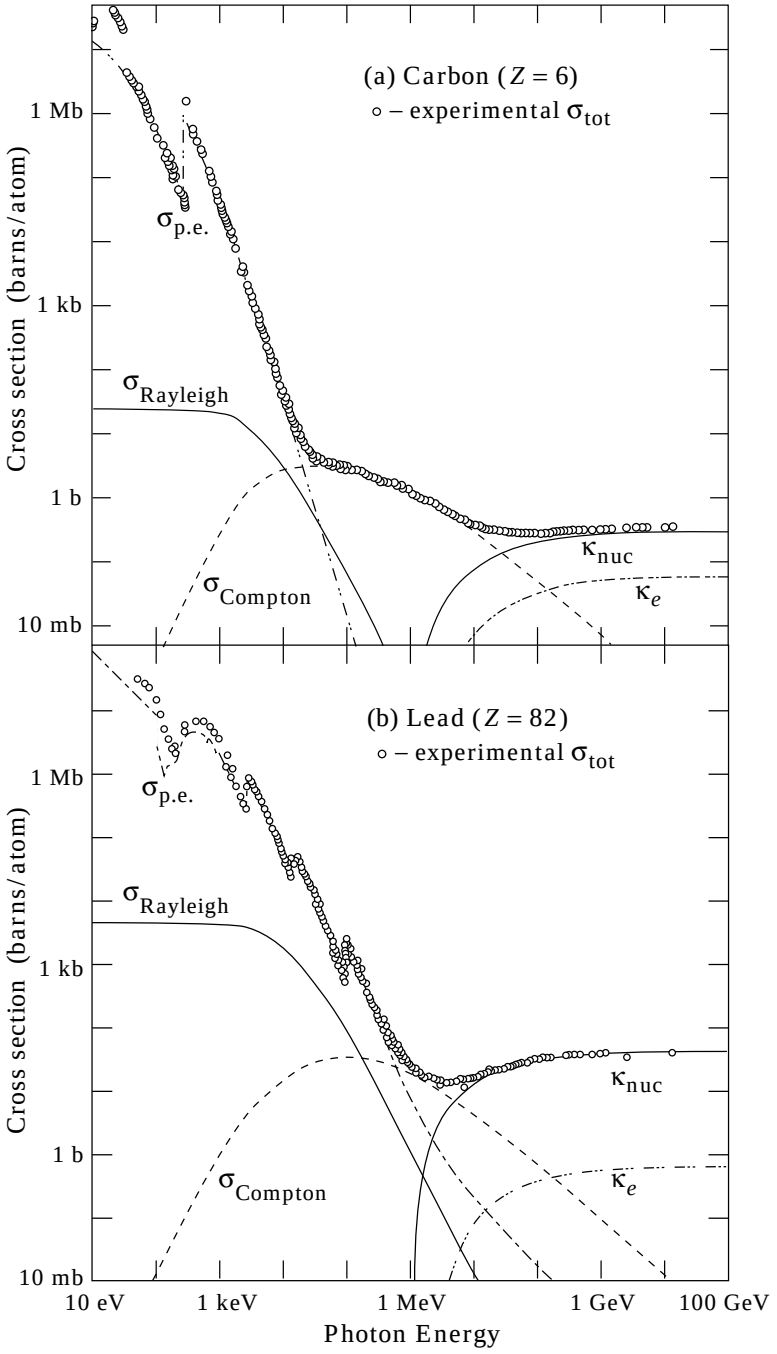

Figure 4.2: Total photon cross sections as a function of energy in carbon and lead, showing contributions of different processes. At high energies pair production dominates ($\mathcal{K}_{nuc}$ and $\mathcal{K}_e$ denote pair production in nuclear and electron fields, respectively).

radiation length. The transverse development of the electromagnetic shower, is mostly determined by scattered electrons (since bremsstrahlung photon production is highly directional), and can be described fairly accurately with the *Molière radius* R_M, given by [56]:

$$R_M = X_0 \, E_s / E_c \tag{4.4}$$

where $E_s \approx 21$ MeV and E_c is Rossi's *critical energy* (energy at which the ionization loss per radiation length is equal to the electron energy). A simulation for a 30 GeV electron induced cascade profile in iron is shown in Figure 4.3 [54, 57]: As it can be seen from the Figure 4.3 the longitudinal

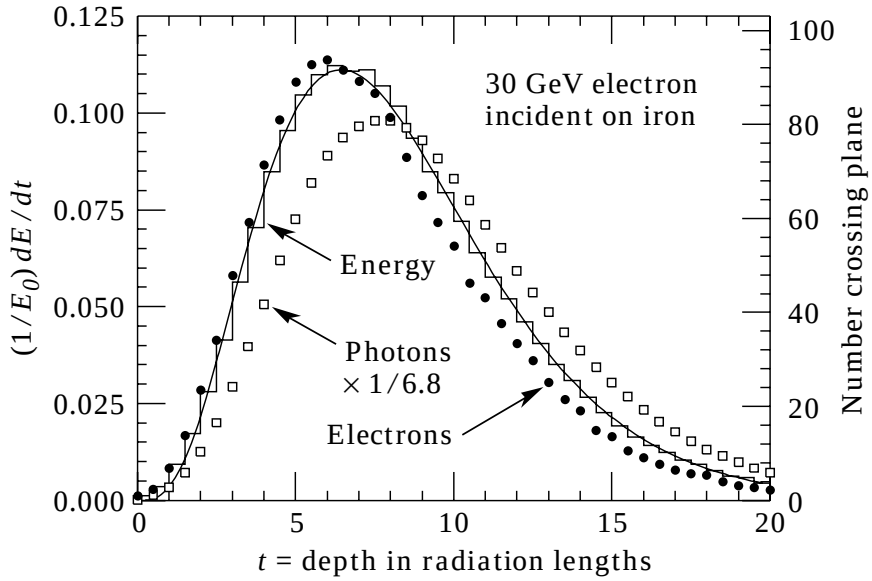

Figure 4.3: 30 GeV electron cascade induced in iron (EGS4 simulation). The histogram shows fractional energy deposition per radiation length, and the curve is a gamma-function fit to the distribution. Circles indicate the number of electrons with total energy greater than 1.5 MeV crossing planes at $X_0/2$ intervals (scale on the right) and the squares are the number of photons with $E \geq$ 1.5 MeV crossing the planes (scaled down to have the same area as the electron distribution).

containment of the shower is within $\sim 20X_0$, a fact that defines the thickness of the EM calorimeter (in DØ this is chosen to be $21X_0$). In the transverse direction the containment of the shower is within a length $R_M \sim 2.5cm$.

4.1.2 Hadronic Showers

The development of hadronic showers, although different in nature from the electromagnetic ones, can be described by the quantity λ, the *absorption length*. This quantity is the mean distance traveled before an inelastic scattering occurs and is analogous to the radiation length X_0, as it defines the longitudinal and transverse dimensions of the hadronic shower. For high-energy hadrons, the main process of energy dissipation when passing through a material, is the inelastic scattering from the constituent nucleons. If σ_{inel} is the cross section for the above process and n is the number of nuclei per unit volume in the matterial, the absorption length is given by:

$$\lambda \approx \frac{1}{n\,\sigma_{inel}}\,. \tag{4.5}$$

The longitudinal development of a hadronic shower is characteristic of a sharp peak near the first interaction point, since at this stage a number of π^0's are produced (which create well-contained EM showers), followed by a more gradual development. In the transverse development, the hadronic shower is essentially contained within a range of λ, since almost 95% of it's energy is contained there. Since the absorption length for a typical calorimeter is at least an order of magnitude greater that X_0, the hadronic showers tend to be bigger, on both the longitudinal and transverse size compared with the electromagnetic ones. Figure 4.4 shows a simulation of showers produced by various particles inside the DØ detector. For the simulation, the DØGSTAR package (DØ GEANT Simulation of Total Apparatus Responce) was used.

4.2 EM Reconstruction and Identification

The first step in the reconstruction of electromagnetic objects in DØ, is the readout of the nearly 55,000 calorimeter cells (readout cells). Because of various reasons, noise appears in the readout calorimeter channels (with some mean width σ; in each particular channel). The presence of noise distorts the process of reconstruction, and to avoid that, only cells for which the ratio of the measured energy (above some pedestal) and the mean width of the noise, is above a threshold are read

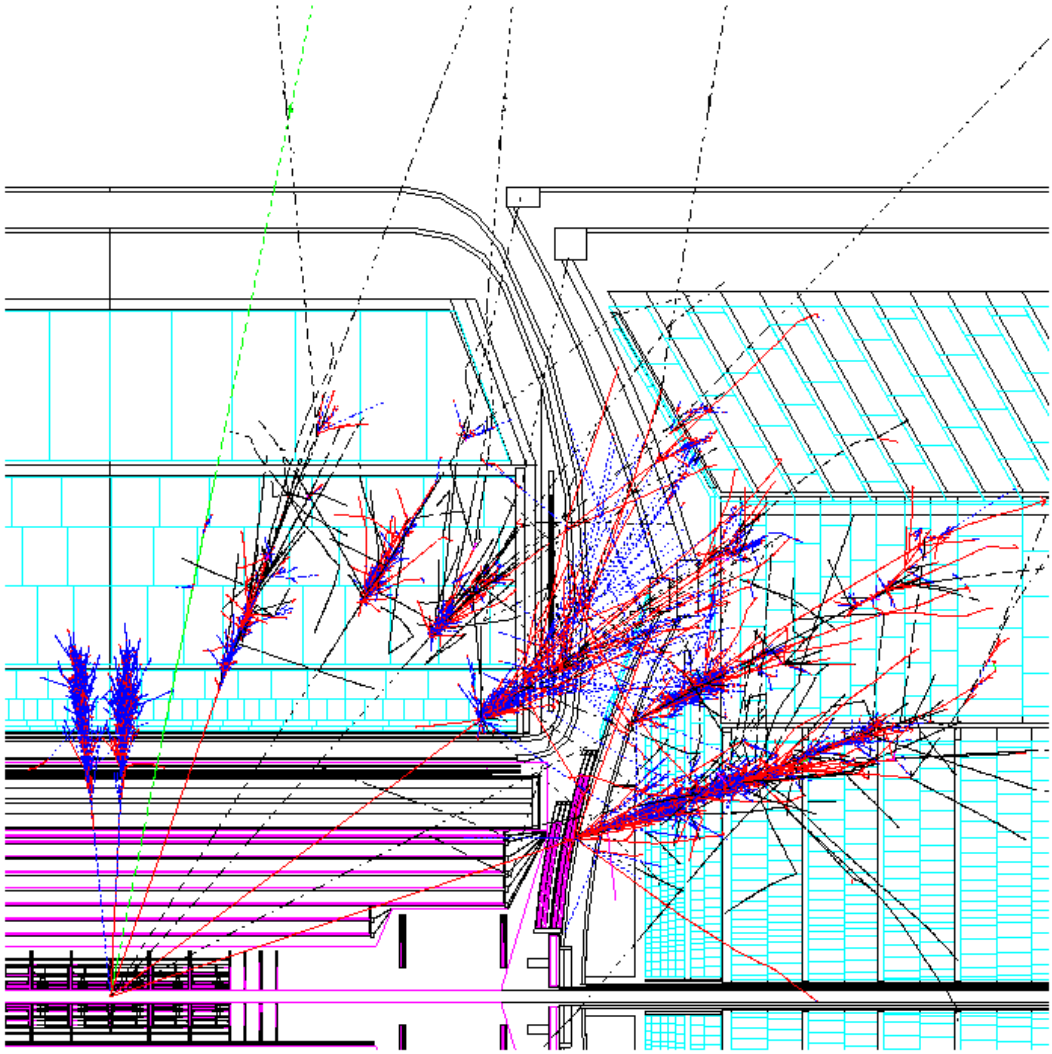

Figure 4.4: Shower simulation with DØGSTAR of particles with $p_T = 50$ GeV. Particles simulated include γ, e^-, μ^+, π^+, K_L^0, K_S^0, n^0, $\overline{p}$.

out. This is usually described as "zero-suppressed" readout, and one refers to a suppression of "x σ". Also due to liquid argon contamination, depleted uranium noise and deficiencies in the readout electronics, cells with unusually high energy can appear ("hot cells") affecting the reconstruction. To mark these cells and prevent their usage, a specifically designed algorithm is used called *NADA* [58]. The resulting calorimeter cells, with the same η and ϕ, are grouped together to form towers. Electromagnetic object reconstruction from calorimeter information (cells or towers), is done in DØ by using three different cluster-finding algorithms [59, 60, 61]:

- Simple-Cone tower clustering algorithm ("Scone Method");
- Cell-level Nearest Neighbor clustering algorithm ("CellNN Method") ;
- Track extrapolation clustering algorithm ("Road Method" - used for EM objects in jets).

For this analysis, objects reconstructed with the simple-cone algorithm are used. After electromagnetic clusters are seeded by towers, the cluster has to pass some selection criteria based on a set of identification (ID) variables, in order to be considered an electromagnetic candidate (electron or photon). This set of variables will be presented briefly in the next sections.

4.2.1 Electromagnetic Isolation

To calculate the *electromagnetic isolation (EM_{iso})* variable, towers and their centroid, in a 10×10 tower window (in $\eta - \phi$ space) around the highest p_T tower are used as shown in Fig. 4.5. Within this window centered in the highest p_T section, the electromagnetic energy E_{EM} within a cone of radius $R < 0.2$ (using only EM floors), and the total energy E_{tot} within a cone of radius $R < 0.4$ (using both EM and hadronic sections) around the centroid is computed as shown in Figs. 4.5 and 4.6. The isolation then is defined as follows:

$$EM_{iso} \;=\; \frac{E_{tot}\,(R<0.4) - E_{EM}\,(R<0.2)}{E_{EM}\,(R<0.2)}\,, \tag{4.6}$$

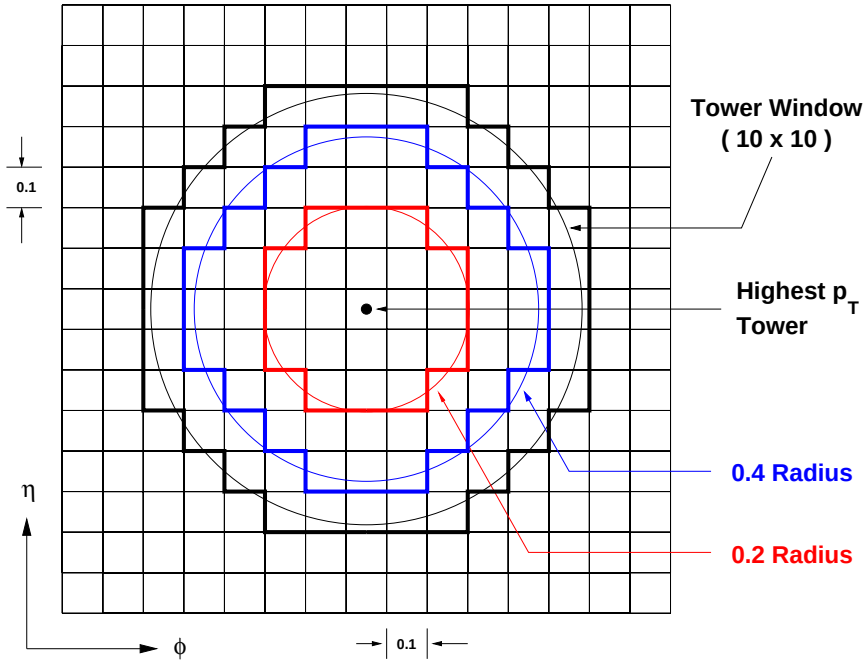

Figure 4.5: Cluster reconstruction windows in $\eta - \phi$.

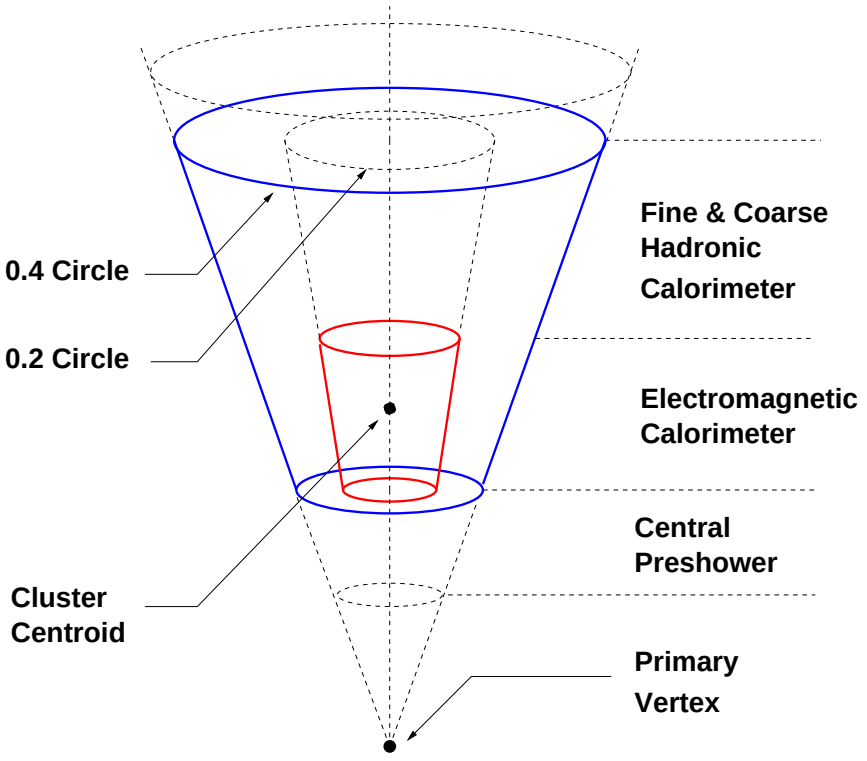

Figure 4.6: Representation of the EM object reconstruction cones.

where the radius R is defined in the $\eta - \phi$ space as:

$$\Delta R \;=\; \sqrt{\Delta\eta^2 + \Delta\phi^2}\,. \tag{4.7}$$

Clusters with $iso < 0.2$ are selected as electromagnetic candidates during reconstruction. The isolation variable is a measure of how deep and narrow a cluster is. Photons and electrons deposit their energy in a narrow region in the EM calorimeter, while hadrons deposit a significant amount of energy in the CH and FH floors and in a much wider radius.

4.2.2 Electromagnetic Fraction

As we have seen in previous sections the development of the electromagnetic and hadronic showers is quite different, so the energy deposited within a cluster can be used as a discriminating variable. The *electromagnetic fraction (EM_{fract})* is defined as follows:

$$EM_{fract} \;=\; \frac{E_{EM,\,FH1}}{E_{total}} \tag{4.8}$$

where E_{EM} is the amount of cluster energy in the EM and FH1 calorimeter floors only and E_{total} is the total amount of cluster energy (including all hadronic floors). A representation of the above energies is shown in Figure 4.7. During cluster reconstruction, clusters with $E_T > 1.5$ GeV and $EM_{fract} > 0.9$ are selected.

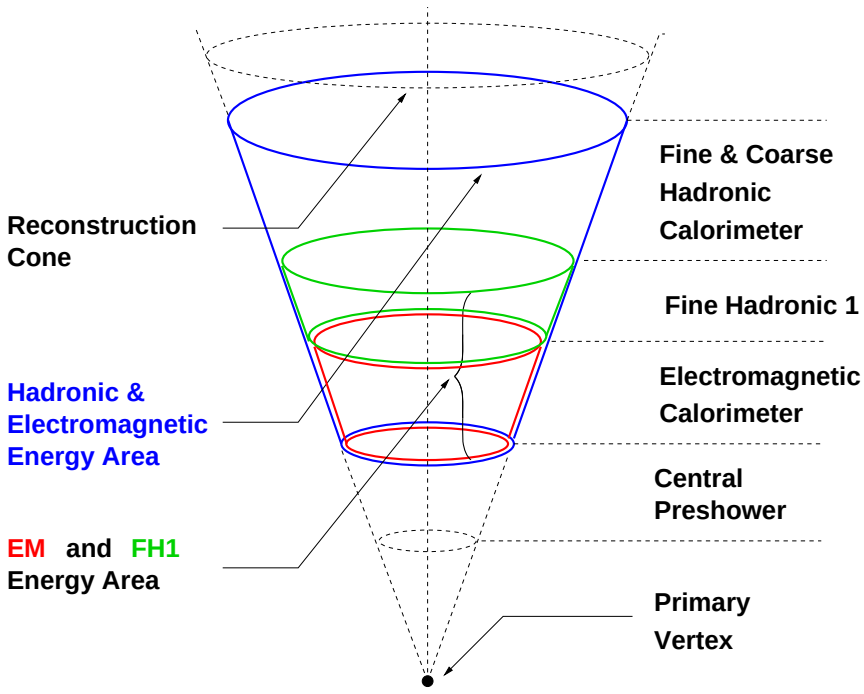

Figure 4.7: Representation of total (E_{total}), hadronic ($FH1$), and electromagnetic energy (EM) of a cluster used for the determination of the electromagnetic energy fraction (EM_{fract}).

4.2.3 H-Matrix Variable

Besides the energy deposition, another difference between the electromagnetic and hadronic showers is the shape of the shower itself. The longitudinal and transverse shower shapes, along with the different energy deposition for hadronic and electromagnetic showers, can both be accounted for, by means of a covariance matrix technique called the *H-Matrix (HM)*. For a sample of Monte Carlo generated electrons (or photons) the H-Matrix is defined as the inverse of the covariant matrix, calculated for each η bin:

$$M_{\alpha\beta} \;=\; \frac{1}{N}\sum_{n=1}^{N}\left(x_{\alpha}^{n}-\langle x_{\alpha}\rangle\right)\left(x_{\beta}^{n}-\langle x_{\beta}\rangle\right), \tag{4.9}$$

where x_{α}^{n} is the value of the selected variable α for the electron n and $\langle x_{\alpha}\rangle$ is the mean value of the selected variable α for the sample. Many combinations of variables have been selected and their performance tested for electrons and photons in the DØ reconstruction algorithm. In this analysis, two closely related sets of variables have been used, comprising the so-called *H-Matrix-8 (HMx8)*

and *H-Matrix-7 (HMx7)* variables: For the H-Matrix-8, the variables chosen are:

- Shower energy fraction in EM1, EM2, EM3, EM4 (longitudinal development);
- Cluster size in $r\phi$ computed from EM3 cells (transverse development);
- Cluster size in r *or* z-axis (EC or CC), computed from EM3 cells (transverse development);
- $\log_{10}(ClusterEnergy)$ (energy dependance);
- Position of the event vertex (impact parameter dependance).

For the H-Matrix-7, the requirement for the transverse development in r *or* z-axis is omitted. To determine whether a shower k is electromagnetic, the following χ^2-like variable is calculated using the H-Matrix as an error matrix:

$$\chi^2_{HM} \;=\; \sum_{\alpha,\beta} \left(x^k_\alpha - \langle x_\alpha \rangle\right) H_{\alpha\beta} \left(x^k_\beta - \langle x_\beta \rangle\right). \tag{4.10}$$

Although this variable is not a real χ^2 (since the variables involved are not always distributed according to the normal distribution), it can be used to separate hadronic from electromagnetic clusters by imposing a cut on χ^2_{HM} (H-matrix cut). This covariance matrix is a measure of how similar the shower is to an electron shower or to a non-electron (hadronic) shower, comming from π^0's that look like EM showers if they carry a significant fraction of the jet energy.

4.2.4 Track Match and Track Veto

The above described variables, although very discriminant, are solely based on the energy deposition in the calorimeter, therefore allowing for QCD processes to contaminate the electromagnetic sample (electrons and photons), for example with photons produced from $\pi^0 \to \gamma\gamma$ decays. In order to reduce this effect, we can use the information provided to us from the detector's tracking systems (SMT and CFT), and require an association of the cluster with a reconstructed track. There are more than one way to do so, since tracks can be reconstructed with information taken from SMT only, CFT only, or both; the latter called "global tracks". In this analysis, as we mention in section 4.4, only global tracks (GTR) are used. For these tracks, three parameters are measured ($p_T,\ \eta,\ \phi$), the

former providing energy information for the track, while the last two providing spatial information. In order to match a track to a cluster, DØRECO uses all or some of the above quantities, creating two χ^2 variables: one with energy dependence and one providing only spatial information. The energy-dependent $\chi^2_{(E/p)}$ variable is defined as:

$$\chi^2_{(E/p)} = \left(\frac{\delta\phi}{\sigma_\phi}\right)^2 + \left(\frac{\delta z}{\sigma_z}\right)^2 + \left(\frac{E_T/p_T - 1}{\sigma_{E/p}}\right)^2; \tag{4.11}$$

and the closely related $\chi^2_{(spatial)}$ variable as:

$$\chi^2_{(spatial)} = \left(\frac{\delta\phi}{\sigma_\phi}\right)^2 + \left(\frac{\delta z}{\sigma_z}\right)^2, \tag{4.12}$$

where in the above expressions:

- $\delta\phi$ (resp. δz) is the difference between the ϕ (resp. z) of the cluster position in EM3 and the impact of the track at the same floor;
- $\sigma_\phi,\ \sigma_z\ and\ \sigma_{E/p}$ are the rms of the distributions of the variables $\phi,\ z\ and E_T/p_T$ based on data;
- E_T/p_T is the transverse energy ratio between cluster and track.

To match a cluster to a track cuts on the above quantities are required.

The above variables serve also as a mean to distinguish electrons from photons, since for a sample of candidates, where there is a high confidence that they are EM objects, only the electron has a track associated with it (charged particle). We will see this in more detail in the analysis section.

4.2.5 EM Energy Scale

After the electromagnetic objects have been reconstructed by DØRECO, their energies need to be corrected for various effects before they can be used reliably in any physics analysis. The package responsible for this task (among others), is called *d0correct* [62], and currently it's provided in DØ from the Common Sample Group (CSG) [63]. This package essentially calls all the post processing

codes for correcting and certifying electromagnetic objects (along with muon, jet and $\not\!\!E_T$ objects). For electromagnetic objects there are two main sources of corrections:

- Geometry Effects;
- Energy Scale Corrections.

The origin of geometry effect corrections is due to the material in front of the calorimeter, calorimeter un-instrumented regions, and gaps between the calorimeter cells. As a result the electron energy reconstructed in the calorimeter is lower than it has initially. Obviously in order to account for these effects, the true energy of the electromagnetic object must be known, therefore the geometry corrections are done by using Monte Carlo simulated single electrons [64]. In this way, a parametric expression for the corrections is deduced as a function of electron's energy and η:

$$\Delta E\,(\eta,\, E_{RECO}) = E_{TRUE} - E_{RECO}\,. \tag{4.13}$$

The origin of energy scale corrections, is due to the fact that sampling calorimeters measure only a fraction of the energy they absorb. To correct for this effect, a calibration and determination of the sampling weights has to be performed. In DØ this work has been done using both Monte Carlo simulation (DØGSTAR) and real data (pure sample $Z \rightarrow e^+e^-$) [65]. These corrections are energy and η, ϕ dependent, and they are found essentially by minimizing the following expression:

$$\chi^2 = \sum_{events} \left(E_{TRUE} - \sum_{k=1}^{4} \beta_k E_k \right)^2 , \tag{4.14}$$

where E_{TRUE} is the energy deposited in the LAr in floor k, and β_k the sampling weight.

In this analysis all the data used were corrected using the standard package d0correct.

4.2.6 Photon Pointing

One of the advantages of the excellent transverse and longitudinal segmentation of the DØ calorimeter and preshower detectors, is that we can utilize it to determine the impact parameter and the z-position of the photon point-of-origin. From the physics point of view, this was appreciated in

some Run I analysis [66, 67], and also in Run II, can be used for the detection of long-lived neutral or charged massive particles that appear in many supersymmetry scenarios [68].

Among other models which allow for a relatively long-lived *next-to-lightest supersymmetric particle (NLSP)*, are the GMSB scenarios, in which a neutral NLSP (usually a neutralino), decays into a photon and a gravitino, the *lightest supersymmetric particle (LSP).*

Photon pointing provides an identification of the angle and point of origin of the electromagnetic shower, independent of the determination of the primary vertex, and based solely on the calorimeter and preshower information. This method of identification, is especially very useful for non-pointing photons. An illustration of pointing and non-pointing photons, based on a DØGSTAR simulation of showers produced by various particles inside the DØ detector, is shown in Fig. 4.8.

For the pointing to be implemented, the first step is to calculate the *center-of-gravity (c.o.g)* of the electromagnetic shower in the preshower and all four electromagnetic floors. After this has been achieved these five spatial points are fitted to a straight line. The above process although simple in principle, requires a very accurate knowledge of the c.o.g in every floor on the preshower and the electromagnetic calorimeter. Because of the fine segmentation of the preshower, the problem is mainly to determine the c.o.g of the calorimeter cells. In order to determine this position, a weighting scheme is used for the calorimeter cells:

$$\begin{aligned} x_{c.o.g}^{floorF} &= \sum_{all\ cells}^{floorF} w_{cell}^{floorF} x_{cell} \ / \ \sum_{all\ cells}^{floorF} w_{cell}^{floorF}, \\ y_{c.o.g}^{floorF} &= \sum_{all\ cells}^{floorF} w_{cell}^{floorF} y_{cell} \ / \ \sum_{all\ cells}^{floorF} w_{cell}^{floorF}, \\ z_{c.o.g}^{floorF} &= \sum_{all\ cells}^{floorF} w_{cell}^{floorF} z_{cell} \ / \ \sum_{all\ cells}^{floorF} w_{cell}^{floorF}, \end{aligned} \tag{4.15}$$

where x, y, z are the cartesian coordinates of the individual calorimeter cell, and w_{cell}^{floorF} a set of weights different for every calorimeter cell and floor. The determination of the weights, is based on a logarithmic weighting of the energy deposition in the electromagnetic calorimeter cells which

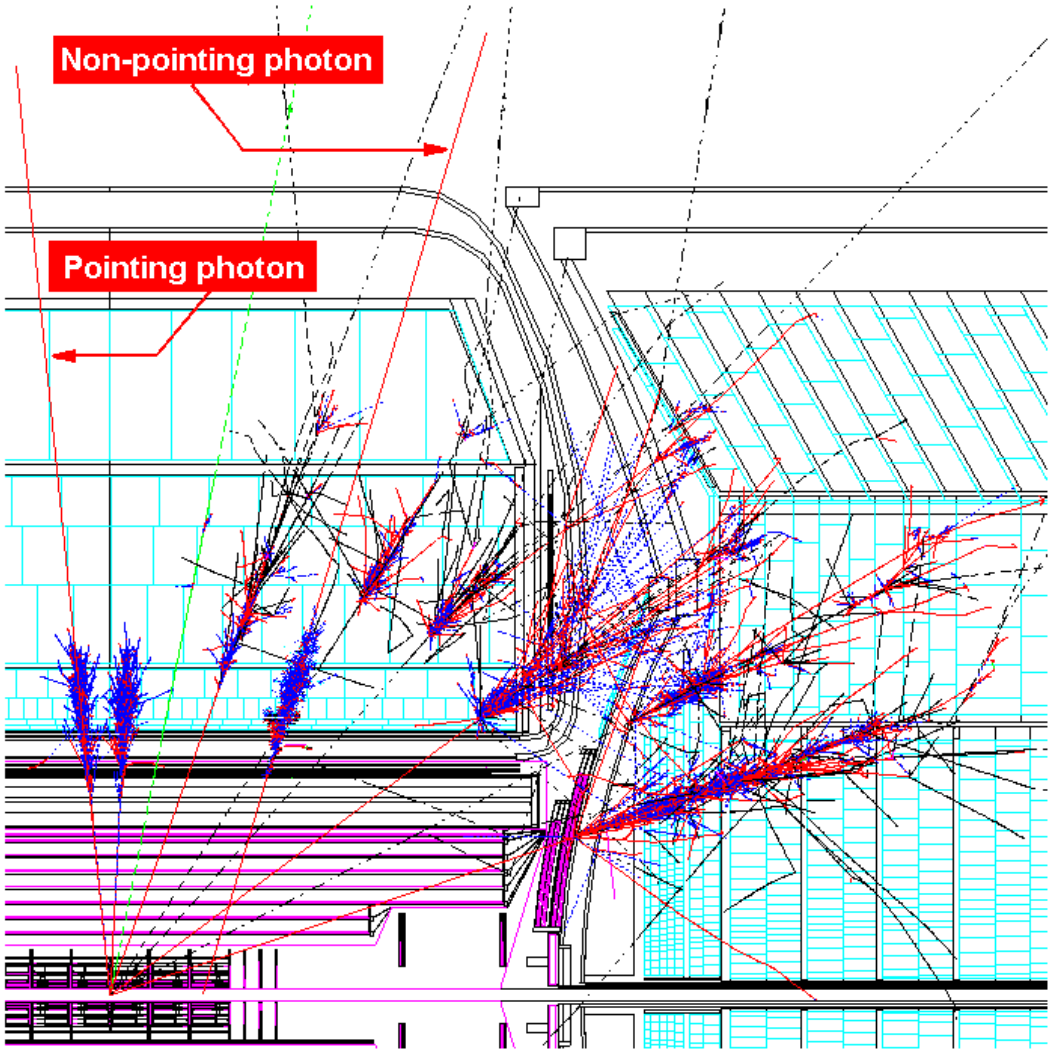

Figure 4.8: Pointing and non-pointing photons in shower simulation with DØGSTAR.

belong to the electromagnetic shower:

$$w_{cell}^{floorF} = max\left\{0,\ \left[w_0 + \ln\left(E_{cell}^{floorF}\ /\ E_{total}^{floorF}\right)\right]\right\}\ , \tag{4.16}$$

where E_{cell}^{floorF} the energy of a cell at floor F, E_{total}^{floorF} the energy of all cells in the floor F, and w_0 a cutoff weight. In the above expression, if the weight w_{cell}^{floorF} is found negative (due to negative cell energies - a byproduct of the calorimeter baseline subtraction), then it is set to zero. In DØ the determination of the weights was done using two methods, via a Neural Network and via a polynomial approach, leading essentially to the same results.

After the c.o.g for each floor is determined using the above method, its spatial correction and correction error are deduced using either a photon Monte Carlo sample (for which the photon trajectory is known), or by using a pure $Z \rightarrow e^- e^+$ Data sample. In the case of the Data sample, tracking can provide us with the information for the electron track, and a full helix extrapolation has to be performed to determine the calorimeter hits. Figures. 4.9 and 4.10 show the residuals in the Central Calorimeter, between the reconstructed position and the position of the c.o.g for a "photon-like"[1] electron data sample. The correction and correction errors are determined by profiling Figs. 4.9, 4.10 and by fitting the resulting profiles with a low-order polynomial. Is has been found that the best description comes from a 5-degree polynomial, which during the fit was forced to be symmetric with respect to the detector center. Figure 4.11 shows the profiling of the residuals in the $r - z$ plane in CC, and Figure 4.12 shows the distribution of the same residuals after correction, which are now centered at zero.

The above process provides us with a correction position map (and their relevant errors) for the whole calorimeter (both Central and Forward region has been studied). Based on these spatial corrections and their associated errors, the pointing algorithm corrects the position of the c.o.g, and then fits them to a straight line, extrapolating it to the origin, to determine the impact parameter (in $r - \phi$) and the z-position (in $r - z$) of the photon point-of-origin. Table 4.1 shows the average

[1] "Photon-like" refers to high p_T electron sample ($p_T > 30$ GeV).

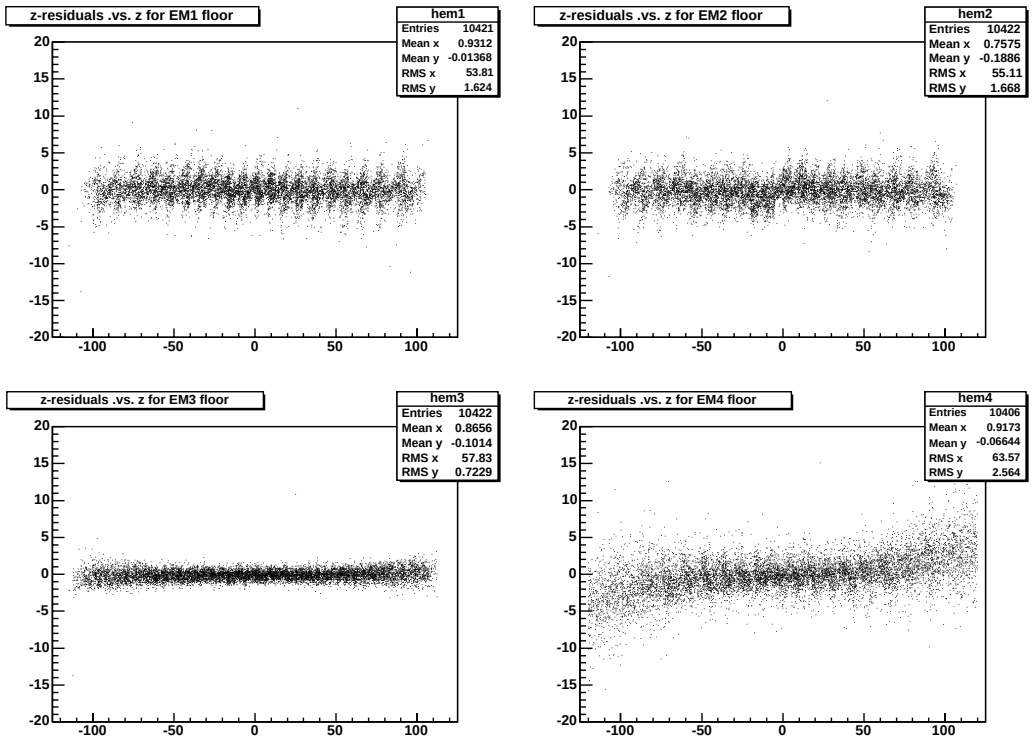

Figure 4.9: Residuals in the $r - z$ plane versus z for the Central Calorimeter.

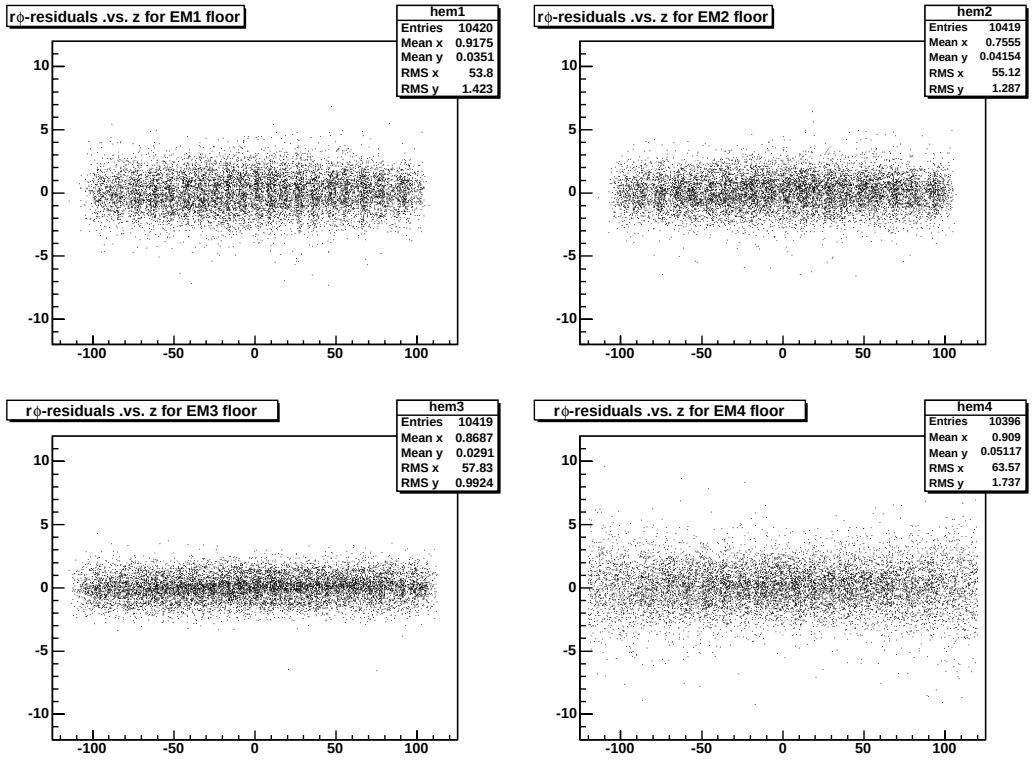

Figure 4.10: Residuals in the $r - \phi$ plane versus z for the Central Calorimeter.

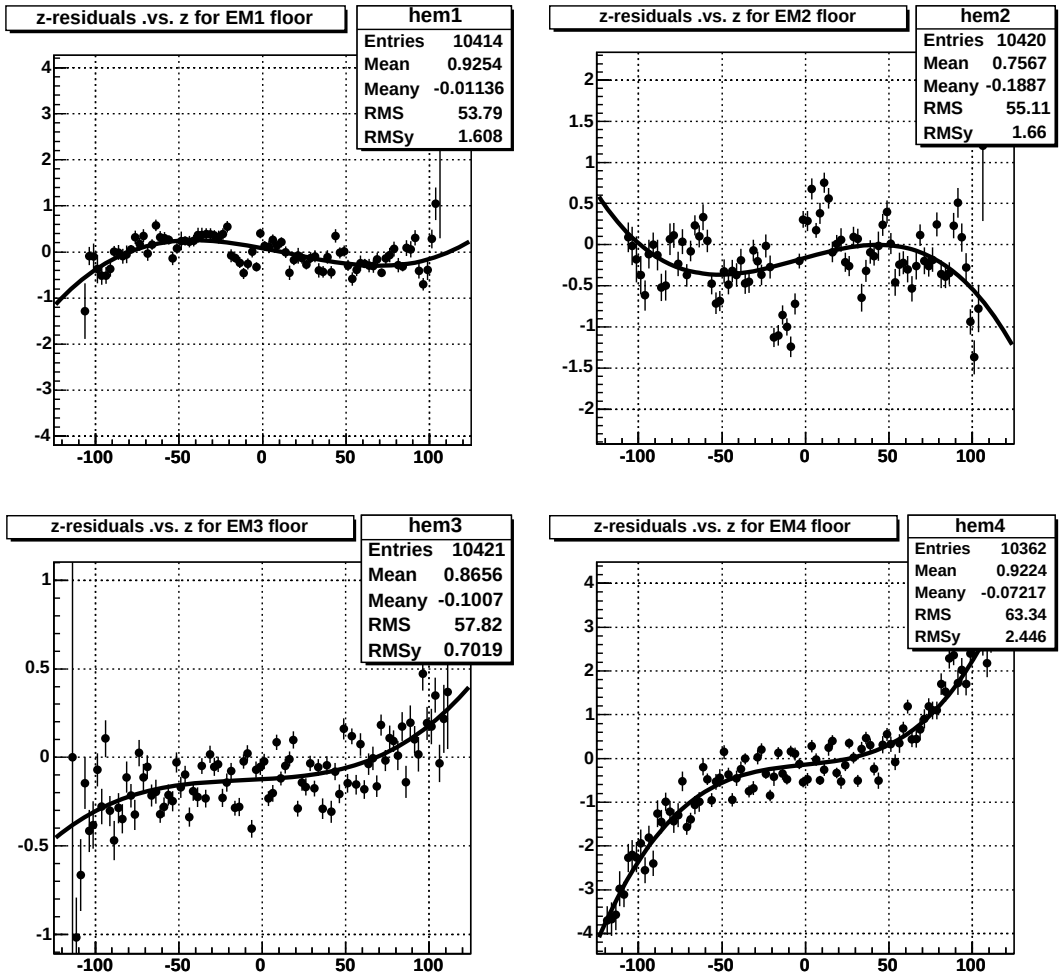

Figure 4.11: Profile of the residuals in the $r - z$ plane versus z for the Central Calorimeter.

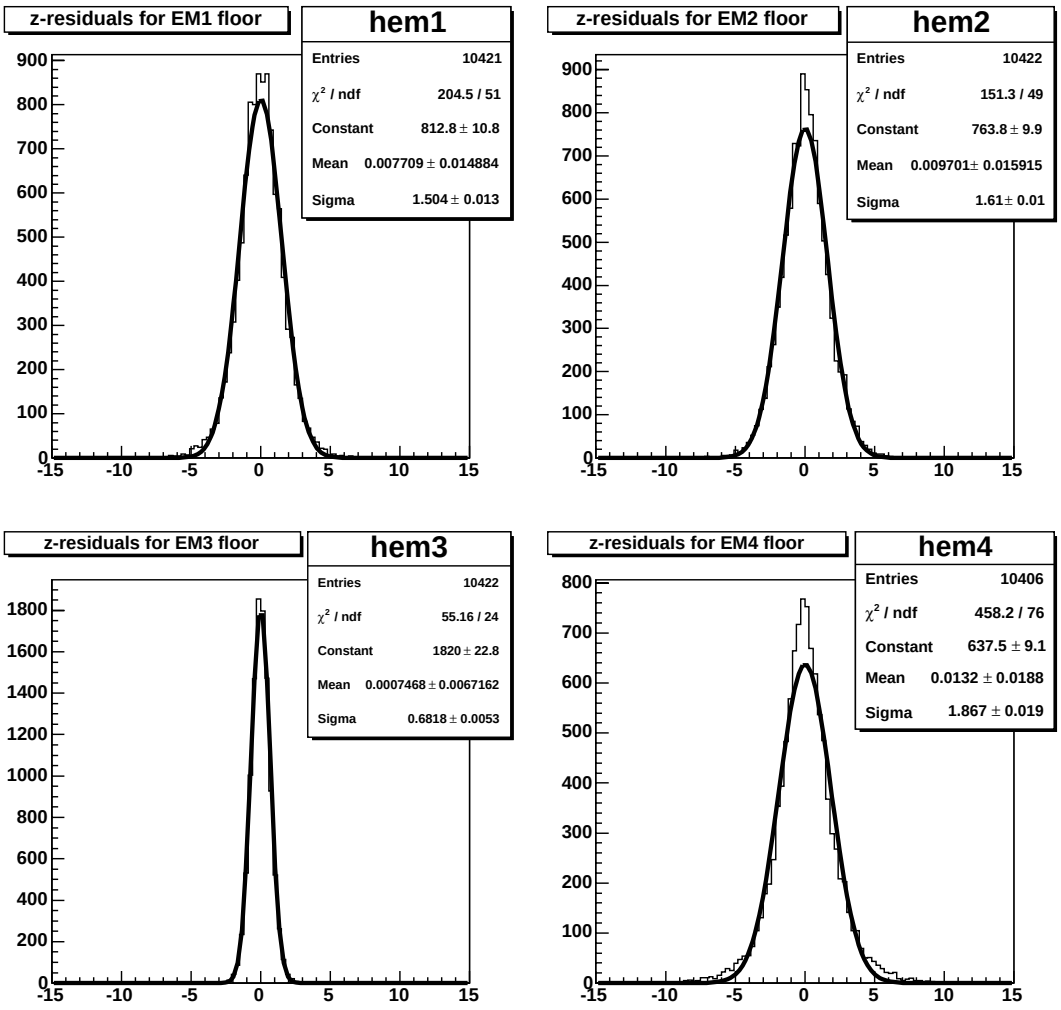

Figure 4.12: Profile of the residuals in the $r - z$ plane versus z for the Central Calorimeter.

resolutions in the central region, for the preshower and calorimeter floors for Run II (Run I values are given in parenthesis). For the Central Calorimeter (which is of an interest for this analysis) the

Quantity	CPS	EM1	EM2	EM3	EM4
$R_{c.o.g}$	73.0 (73.0) cm	85.2 (85.5) cm	87.1 (87.4) cm	91.5 (91.8) cm	99.2 (99.6) cm
σ_z	3.7 (2.5) mm	15 (20) mm	16 (20) mm	6.8 (7.0) mm	19 (15) mm
$\sigma_{r\phi}$	1.7 (1.5)mm	14 (17) mm	13 (17) mm	6.8 (3.5) mm	16 (7.5) mm

Table 4.1: Geometry and average resolutions in the central region for the Preshower detectors and the EM calorimeter floors for Run II, compared to Run I (inside parenthesis).

pointing resolution for the $r - z$ and $r - \phi$ planes is shown in Fig. 4.13 for the Monte Carlo and in Fig. 4.14 for data. The goodness of the fits is shown in Fig. 4.15, where the χ^2 probability is plotted, being nearly flat for both, the $r - z$ and $r - \phi$ planes.

The Central Calorimeter pointing algorithm for Run II, was developed by the author of this dissertation (Run I code developed by Greg Landsberg [69]), and it is to be part of the official DØRECO algorithm in the near future. Since the pointing has not been certified yet, it was not used in this analysis. Also at the time that this dissertation was written, although the code for the EndCap Calorimeter exists, the Forward Preshower information is not reliable, therefore essentially eliminating the chance for forward pointing until this matter is resolved.

4.3 Jet Reconstruction

Although jets don't appear explicitly in the physics signature under study, their correct reconstruction affects the accurate determination of the missing transverse energy, as we will see in section 4.5 The method and algorithms used for the reconstruction of jets at DØ can be found in details in Refs. [70, 71]; here only a brief overview will be made.

Jet reconstruction in DØ is done with cone-based algorithms, a process that proceeds in the following steps:

- Pre-clustering: In this step calorimeter towers are ordered in E_T, and if their energy is above a threshold, they are selected as "seed towers". From these "seed towers" a pre-cluster is formed

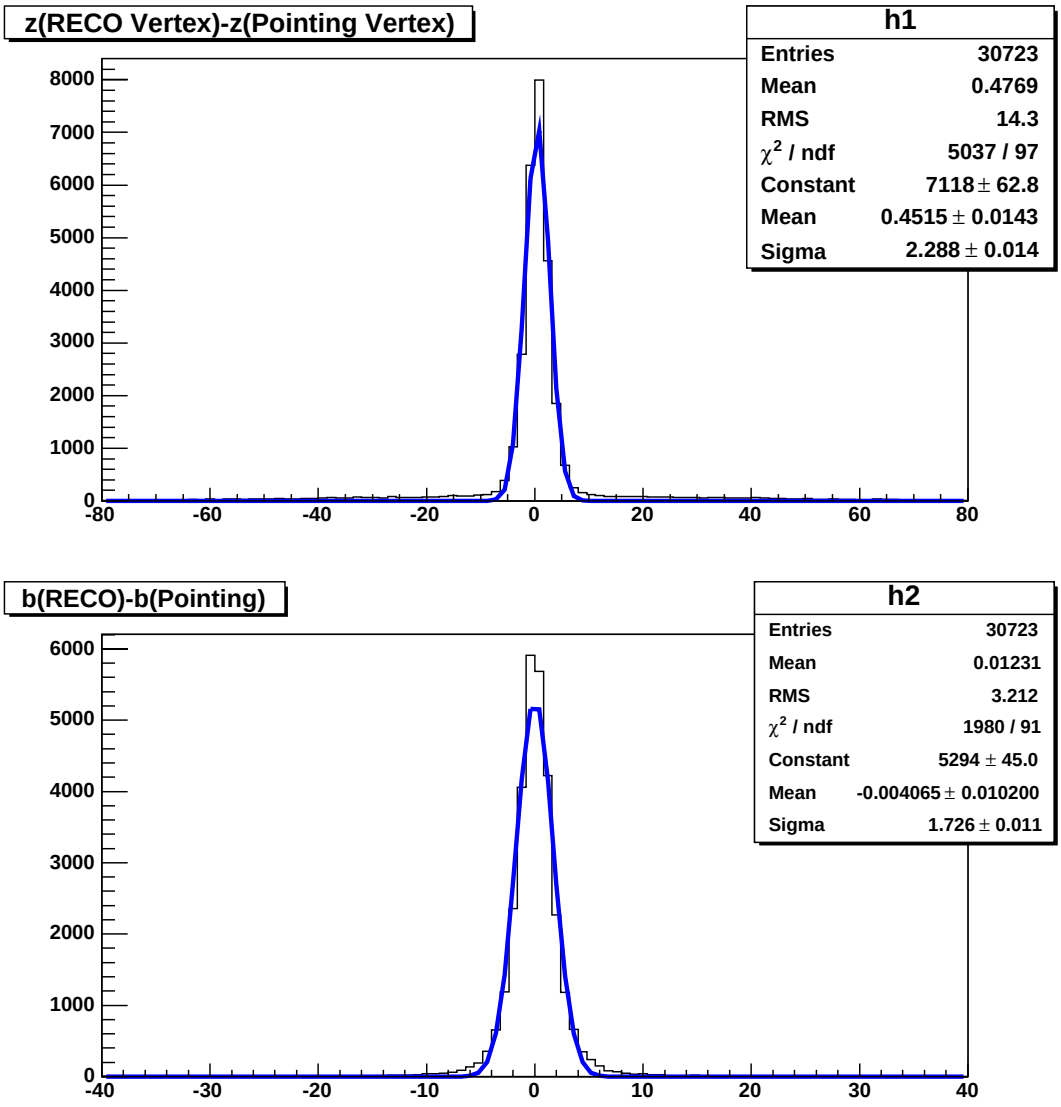

Figure 4.13: Pointing resolutions for the $r - z$ and $r - \phi$ planes for the Central Calorimeter for Monte Carlo.

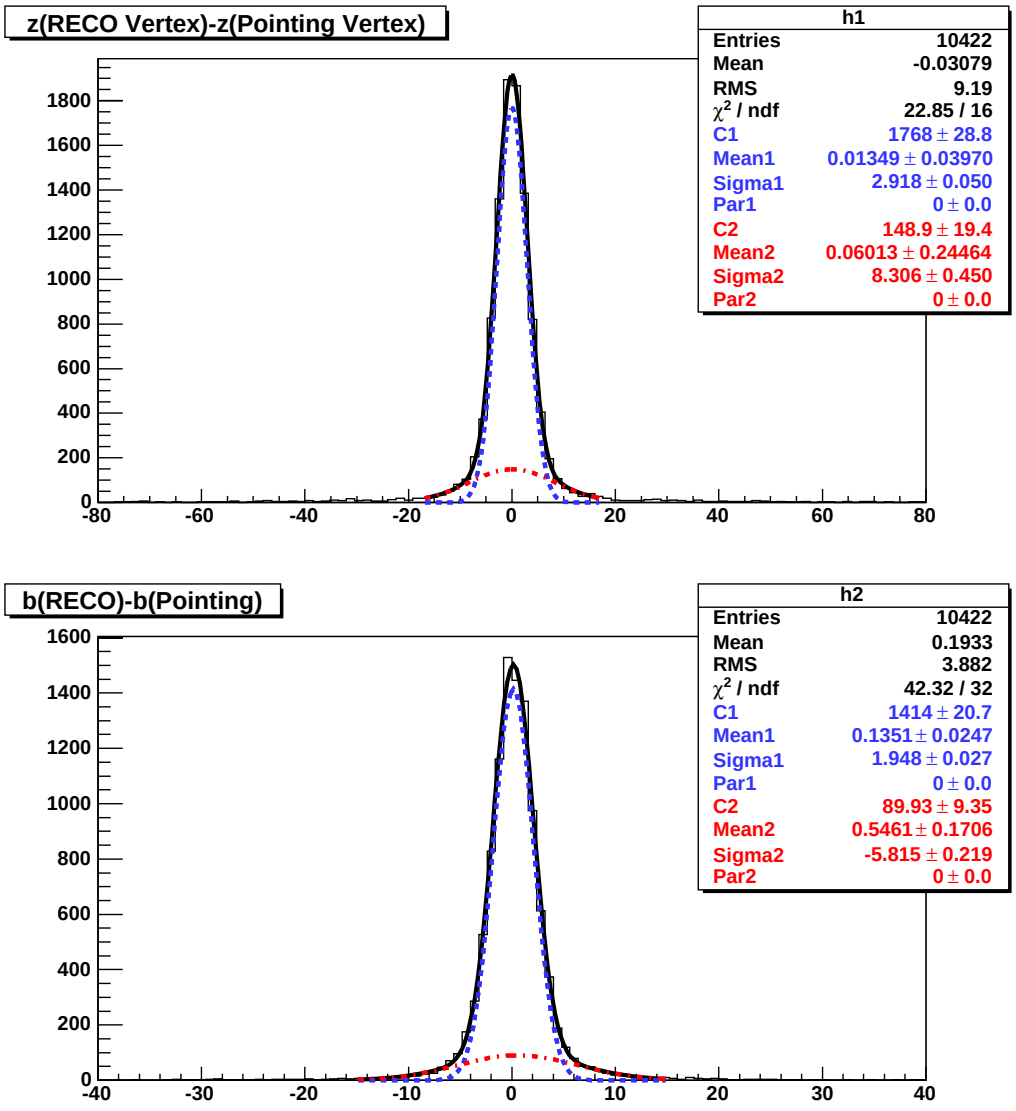

Figure 4.14: Pointing resolutions for the $r - z$ and $r - \phi$ planes for the Central Calorimeter for Data.

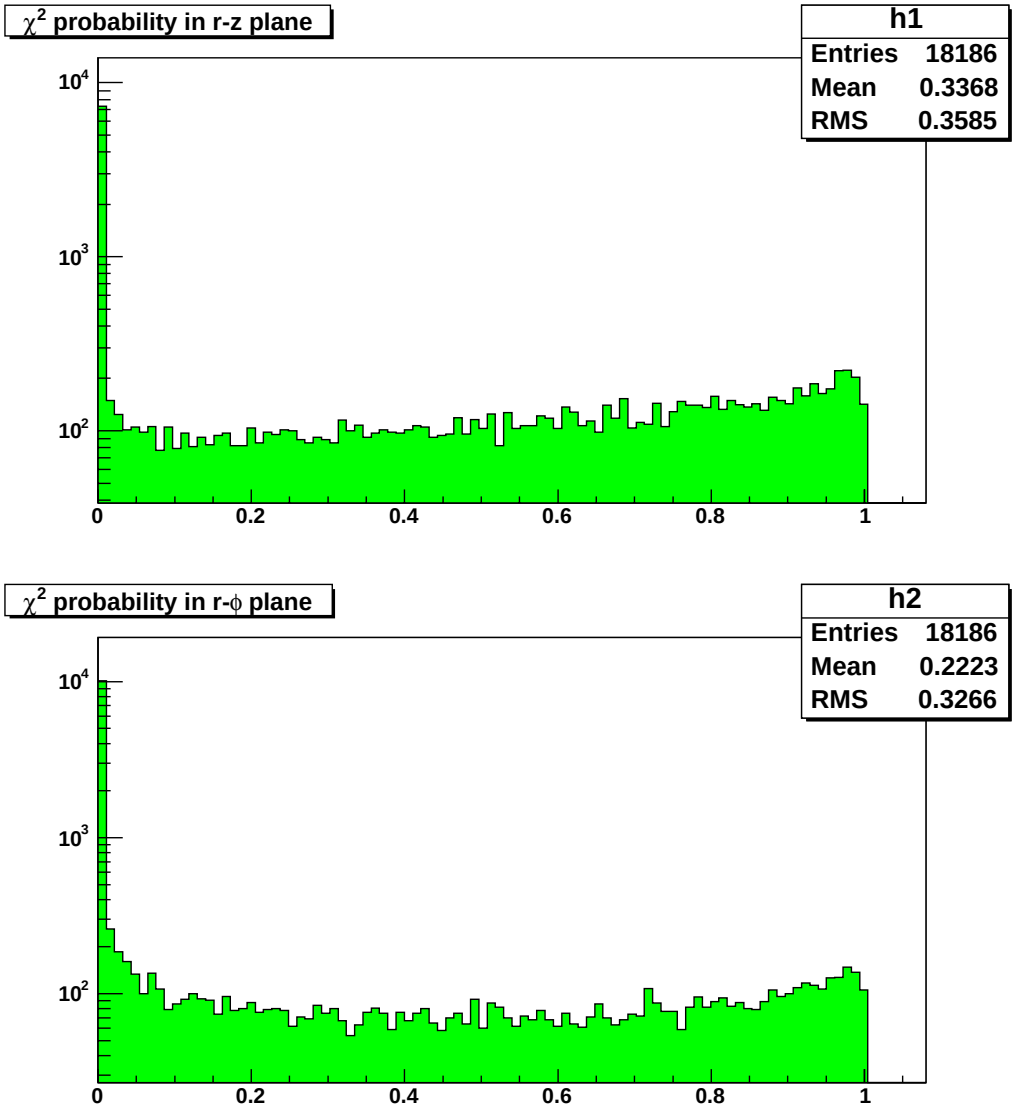

Figure 4.15: χ^2 probability for the fits in $r - z$ and $r - \phi$ planes for the Central Calorimeter.

from all adjacent towers with $\delta\eta < 0.5$ and $\delta\phi < 0.5$. For each pre-cluster, it's centroid is E_T weighted[2] and the new centroid is used as a candidate jet.

- Cone Clustering: In this step starting from the candidate jet, the above process is repeated, only this time, only calorimeter towers within a radius R in the $\eta - \phi$ space are used. This process of cone clustering is repeated until the position of the centroid stabilizes.
- Splitting and Merging: In the final step, to avoid a calorimeter tower to be shared by two jets, the fraction of energy that two jets share is examined. If this fraction is above 50% of the energy of the softer jet, then the two jets are merged and their centroid is re-calculated (merging). Otherwise, towers are assigned to their closest jet and centroids are re-calculated (splitting).

Although it's desirable that the jet's energy be the same as with the parton that created the jet, for most of the time this is not the case. A series of effects lead to differences:

- Jet cone doesn't contain all particles, some of which shower outside of it;
- The response of the calorimeter is not uniform on all energies, therefore summing up the calorimeter energy doesn't account correctly the jet's energy since it contains a large number of particles with a range of energies;
- The calorimeter readout uses improper zero-suppression that can lead to a shift in jet's energy.

To account for the above, jet energy scale corrections are applied in jet reconstruction [72], using the default *dØcorrect* version 6.0 prescription [73]. This prescription applies to jets that passed quality cuts recommended by the Jet and $\not\!\!E_T$ ID Group [74].

4.4 Track and Vertex Reconstruction

Here we will give a brief description of the reconstruction process, the details about the method and algorithms used for this task go beyond of the scope of this section. The reader is referred to Ref. [75] for details about track reconstruction and to Ref. [76] for details about vertex reconstruction used

[2]That is: $\eta_\nu = \sum E_T \cdot \eta_{\nu-1} / \sum E_T$ and $\phi_\nu = \sum E_T \cdot \phi_{\nu-1} / \sum E_T$ for the centroid's position.

by the reconstruction program DØRECO. The first step in track and vertex reconstruction is the reconstruction of the hits found in the two DØ inner tracking systems, the SMT and the CFT. The reconstruction of the tracks from the hits is performed by using the *Road approach*, implemented in the GTR tracking algorithm [75]. This algorithm consists of five components:

- Surfaces (cylinders or planes);
- Paths (a list of surfaces that the particle crosses);
- Propagators (track extrapolation algorithms from one surface to another);
- Fitters (track-cluster matching algorithms);
- Filters (track rejection algorithms).

Using a model of the detector and the hits of the first few surfaces, "seed tracks" are defined initially, and later on extrapolated to the remaining surfaces to determine the hits on them. After these hits have been found, the task of the "fitter" is to perform a χ^2 match of a new cluster to the track-hit, and reject clusters with high χ^2. After these candidate tracks have been found using a certain path, a final clean-up is performed by the "filters". These algorithms reject tracks on the basis of their overall χ^2 match and the number of traversed surfaces without matched clusters. In the central region, which is of the interest of this analysis, track finding starts using the CFT which provides 3D "seed tracks" using the axial and stereo hits. After that, these track candidates are extrapolated into the SMT. After the candidate tracks are found, the reconstruction of primary and secondary vertices is performed, described in detail in [76]. A brief description of the process follows.

The reconstruction of the primary vertex starts with a list of all reconstructed tracks from the previous stage. From these tracks, an initial selection is performed to exclude tracks with high impact parameter significance with respect to the beam line. These tracks can come from particles with a long lifetime, and therefore decaying away from the primary vertex. All the remaining tracks after the above selection, are fitted to a single vertex, and the track with the highest χ^2 is rejected. Then this process is repeated for the remaining tracks, until a set of these remain all having χ^2 below 10. In this case a vertex is found, from which these tracks originate. The entire procedure is then repeated with the remaining tracks, to reconstruct all the remaining primary vertices for the

event. After the primary vertices are defined, the secondary vertex finding is performed that tries to reconstruct the decay position of long lived particles. At the end of the process a list of all the primary and secondary vertices is kept for the event.

4.5 Missing Energy - $\not\!\!E_T$

As we mention at the end of section 3.3 the energy balance in $p\overline{p}$ collisions cannot be used to analyze the outcome of the collision, since a significant fraction of energy escapes the detector (*spectators*). However, the transverse momentum (energy) balance can be used. *Missing energy ($\not\!\!E_T$)* [77] in the plane normal to the beam-line can be the result of the following:

- Particles that have very small interactions with matter (neutrinos);
- Particles (not yet observed) non-interacting with matter (sparticles - LSP, gravitino);
- Mis-measurement of the "visible" final state (vertex position, jet and em object's energy).

For the determination of the missing transverse energy, the sum of the transverse energies of all calorimeter cells above 200 MeV is used (both electromagnetic and hadronic in general), and the missing transverse energy is found by using the following formulas:

$$\not\!\!E_X = -\sum_{cells} E_T \cos\phi\,, \qquad \not\!\!E_Y = -\sum_{cells} E_T \sin\phi\,, \qquad \not\!\!E_T = \sqrt{\not\!\!E_X{}^2 + \not\!\!E_Y{}^2}\,, \tag{4.17}$$

where $\not\!\!E_X$ the missing transverse energy along the x-axis, $\not\!\!E_Y$ the missing transverse energy along the y-axis and E_T the sum of the transverse energies of all calorimeter cells. It is obvious from the above formulas that, in order to calculate the E_T for the calorimeter cells, the position of the vertex that affects the E_T must be known and also an accurate measurement of the scalar energy of the cells must be done. These are the two sources of mis-measurement of the $\not\!\!E_T$ of the "visible" final state. To get an accurate measurement of the scalar energy of the cells, an optimized cell-threshold is used to keep the contribution from noise in the calorimeter readout small. Since the noise level in the coarse hadronic part is higher than comparing to the noise in the em floors, cells in the coarse hadronic floors are used in the above calculation only if they are part of a reconstructed jet. The

above comment shows the importance of the correct jet reconstruction for this analysis, although jets themselves are not explicitly requires in the physics signature under study.

4.5.1 $\not\!\!E_T$ Significance

From the definition of $\not\!\!E_T$ in Eq. 4.17, it's obvious that there are many sources that can affect it's correct determination. Mis-identification of the primary vertex, jet energy resolution, electron/photon energy resolutions, muon energy resolution, un-clustered cell energy, existence of hot-cells, etc. It is therefore desired to be able to decide, how likely is that a measured value of $\not\!\!E_T$ for the event, comes from resolution fluctuations of the energy of the physics objects. In other words what is the "significance" of the measured $\not\!\!E_T$ for that particular event. This knowledge can help us discriminate events with real $\not\!\!E_T$ from events where $\not\!\!E_T$ is mis-measured. This approach to the treatment of $\not\!\!E_T$, was first implemented in Run I [78], and now has been adapted for Run II. Here only a brief description will be made, the reader is referred to [79] for more details.

The basic idea behind the $\not\!\!E_T$ significance algorithm, is that based on our knowledge of the energy resolution of known physics objects, we can compute how likely it is that the measured $\not\!\!E_T$ comes from a resolution fluctuation of the energy of the known objects, in the direction of the observed $\not\!\!E_T$. This decision has to made on an event-by-event basis.

By modeling the probability distribution for the energy of each physics object with a Gaussian, a probability distribution for the $\not\!\!E_T$ can be obtained [79]:

$$p\left(\not\!\!E_T\right) = \not\!\!E_T - N\left(0, \sqrt{\sum_{n=1}^{N_{all}} \sigma_n^2}\right) \tag{4.18}$$

where $N(0,\sigma)$ is the Normal Gaussian distribution, N_{all} is the number of the physics objects in question, and σ_n^2 is the variance of the corresponding distribution for the n physics object. It has to be noted here that for each object, σ_n^2 is quite different and energy dependent, therefore its determination has to be done using data.

Using the formula 4.18, the probability distribution for the projection of $\not\!\!E_T$ in the direction of

the measured $\not\!\!E_T$ can be obtained:

$$p\left(\not\!\!E_T;\vec{\alpha}\right) = \not\!\!E_T - N\left(0, \sqrt{\sum_{n=1}^{N_{all}-1} \sigma_n^2 \cos^2\left(\vec{n},\vec{\alpha}\right) + \sigma_{UE}^2}\right), \tag{4.19}$$

where in the above expression $\vec{\alpha}$ is the direction of the $\not\!\!E_T$, $\vec{n}$ is the direction of the physics object n and σ_{UE} is the resolution of the un-clustered energy (it fluctuates in any direction so it is not projected during the summation).

Based on the above formula a likelihood can be devised:

$$L \;=\; \log \frac{p\left(\not\!\!E_T;\vec{\alpha}\right)_{max}}{p\left(\not\!\!E_T;\vec{\alpha}=\vec{0}\right)} \;=\; 2\log \frac{{\not\!\!E_T}^2}{2\sigma}, \tag{4.20}$$

where σ is the variance of the $p\left(\not\!\!E_T;\vec{\alpha}\right)$ probability distribution found in Eq. 4.19.

An illustration of the usage of $\not\!\!E_T$ significance can be seen in Figure 4.16 where two examples corresponding to events with large $\not\!\!E_T$ are shown. In the first event (left plot) the $\not\!\!E_T$ is due to an energy imbalance from jet resolution fluctuations. The width of $p\left(\not\!\!E_T;\vec{\alpha}\right)$ is width enough to have a significant contribution at $p\left(\not\!\!E_T;\vec{\alpha}=0\right)$. In the second event (right plot) the $\not\!\!E_T$ is real due to the presence of a neutrino. The $p\left(\not\!\!E_T;\vec{\alpha}\right)$ distribution, event though it peaks at a lower value than the previous event is very narrow with almost no contribution at $p\left(\not\!\!E_T;\vec{\alpha}=0\right)$. As consequence both events with $\not\!\!E_T \sim 50$ GeV will have small and large $\not\!\!E_T$ significance due to their particular topology.

The $\not\!\!E_T$ significance was not used in this analysis.

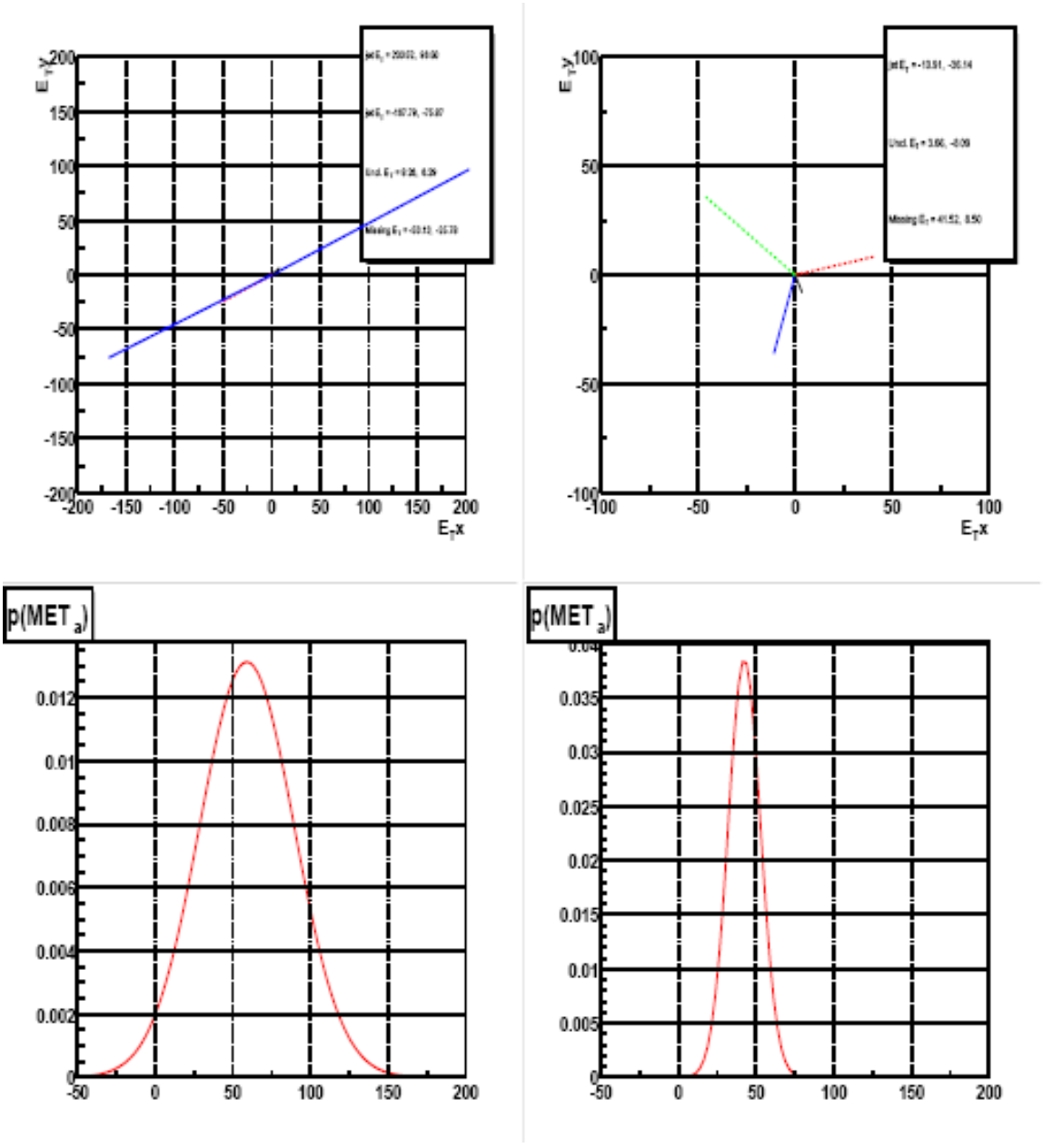

Figure 4.16: Example of $p\left(\not\!\!E_T;\vec{\alpha}\right)$ in two events with large $\not\!\!E_T$.

Chapter 5

Data Sample Selection

This chapter describes the selection of the data sample used for this analysis. As with every search for new physics, we have to rely very often on both the real data recorded in a detector to study the known Standard Model backgrounds, and simulated data in order to describe the signal of the yet unknown physics. In this chapter we will focus our interest on the former; the generated physics signal will be discussed in the next chapter.

5.1 Trigger Requirements

The data sample used for this analysis includes essentially all data collected by the DØ detector, between April 2002 and March 2004. During this time, and as far as this analysis is concerned, there were very few instances where the recorded data were inappropriate for further usage. A set of about 60 runs was excluded, because they had an anomalous high fraction of events with large $\not\!\!E_T$. Also some other runs were excluded because they suffered from calorimeter timing problems. There were also some other incidents that could potentially affect the quality of the data, but in these cases the events/runs were recoverable. An example of this was the presence of "hot cells" in the calorimeter, these cells were simply removed from the analysis while at the same time, a dedicated package (NADA) was used to detect their presence and remove them online. Other examples of runs with problems, include runs that exhibit high temperatures in calorimeter cells ("rings of fire"),

or runs for which there was a mixing in the calorimeter readout towers (one tower was not read, another one read twice). For all of the above cases, either the events were not of any interest for this analysis, or the recorded events were recoverable at a later stage of the reconstruction process. Events recorded were skimmed and delivered for further analysis by the Common Samples Group (CSG), a group responsible for treating, fixing (were possible), and delivering data ready for analysis to the users. Since the data were collected over a relatively long period of time, while the reconstruction code was still under development, they were processed with more than one production versions of the reconstructed program. The major production version used for this analysis was DØRECO production version 14 (p14.xx.yy). Within this major version, more than one sub-versions of the code were used for the reconstruction. The synchronization of the reconstructed physics objects, so that they all meet the same requirements, was also a responsibility of the CSG.

Along with the reconstruction code, the trigger lists used for data taking evolved over time. Different requirements from various physics groups (to trigger on different objects and on all trigger levels) and the need to leave un-prescalled as many triggers as possible while the delivered luminosity increased over time, had an impact on the trigger lists. This analysis was not affected by this evolution; electromagnetic objects are among the most important, so from the beginning, careful thought was used in the design of such triggers. Because of that, they also ran un-prescalled most of the time during this period. Our data set spanned two trigger list versions, involving triggers firing on all levels (L1, L2 and L3). These trigger lists, along with their requirements in each trigger level are briefly described bellow:

The first trigger list comprises the following triggers:

- EM_MX_SH: Require one EM trigger tower having $E_T > 15$ GeV at L1, set the trigger bit true if an $|\eta_d| < 3.0$ EM object is found with $E_T > 20$ GeV meeting loose criteria including a transverse shower shape requirement at L3.

- 2EM_HI: Require two calorimeter EM trigger towers with $E_T > 10$ GeV at L1, one EM object with $E_T > 20$ GeV, $|\eta_d| < 3.0$ meeting loose criteria is found at L3.

- 2EM_HI_SH: Require two calorimeter EM trigger towers with $E_T > 10$ GeV at L1, one EM

object with $E_T > 15$ GeV meeting loose criteria is found (including a transverse shower shape cut) at L3.

and the second trigger list:

- E1_SHT20: Require one calorimeter EM object with $E_T > 11$ GeV at L1, an EM object satisfying tight shower shape requirements with $E_T > 20$ GeV at L3.
- E2_SHT20: Require two calorimeter EM object with $E_T > 6$ GeV at L1, an EM object satisfying tight shower shape requirements with $E_T > 20$ GeV at L3.
- E3_SHT20: Require two calorimeter EM towers with $E_T > 3$ GeV (one of the towers must have $E_T > 9$ GeV) at L1, an EM object satisfying tight shower shape requirements with $E_T > 20$ GeV at L3.
- E1_2SH8: Require one calorimeter EM object with $E_T > 11$ GeV at L1, two EM objects with $E_T > 8$ GeV satisfying loose shower shape requirements at L3.
- E2_2SH8: Require two calorimeter EM objects with $E_T > 6$ GeV at L1, two EM objects with $E_T > 8$ GeV satisfying loose shower shape requirements at L3.
- E3_2SH8: Require two calorimeter EM towers with $E_T > 3$ GeV (one of the towers must have $E_T > 9$ GeV) at L1, two EM objects with $E_T > 8$ GeV satisfying loose shower shape requirements at L3.
- E1_2L15_SH15: Require one calorimeter EM object with $E_T > 11$ GeV at L1, two EM objects are found with $E_T > 15$ GeV satisfying loose cuts (one of the EM objects also must satisfy loose shower shape cuts) at L3.
- E2_2L15_SH15: Require two calorimeter EM objects with $E_T > 6$ GeV at L1, two EM objects are found with $E_T > 15$ GeV satisfying loose cuts (one of the EM objects also must satisfy loose shower shape cuts) at L3.

- E3_2L15_SH15: Require two calorimeter EM towers with $E_T > 3$ GeV (one of the towers must have $E_T > 9$ GeV) at L1, two EM objects are found with $E_T > 15$ GeV satisfying loose cuts (one of the EM objects also must satisfy loose shower shape cuts) at L3.

For the above sets of triggers, studies in both Data and Monte Carlo simulations, were performed to determine their efficiency for events involving two high-p_T photons ($p_T > 20$ GeV). From these studies the efficiency for Data and Monte Carlo was determined to be:

$$\epsilon_{trigger}(p_T > 20\,GeV) = 0.97 \pm 0.01\,. \tag{5.1}$$

5.2 Luminosity Calculation

For each one of the above triggers, the luminosity calculation was done using the standard prescription outlined by the Luminosity ID Group [80]. Luminosity ID Group provides the means for the calculation of luminosity in DØ, in the form of a software package called *lm_access* [81], along with information about the good *luminosity blocks numbers (LBN)* that can be integrated over a desired time period, in order to calculate the luminosity for each trigger name.

This calculated luminosity called *reconstructed luminosity* includes corrections for all sources of disables recorded by the Trigger Framework, losses in the DAQ, lost tapes/files, or failures in DØRECO, and in general differs from the *recorded luminosity* by the DAQ.

For the list of triggers used in this analysis and for the above mentioned time period, the total reconstructed luminosity was calculated to be:

$$\mathcal{L}_{(RECO)} = 263 \pm 17 \text{ pb}^{-1}\,. \tag{5.2}$$

It has to be noted here that in order to maximize the available luminosity for this analysis, the calculation of luminosity was done by using a private list of bad runs and not the official one. This was necessary since a large number of runs were tagged as "bad" in the DØ database because of bad information to various sub-detectors not relevant to this analysis.

5.3 Offline Event Selection

As we have already seen in Chapter 4, the reconstructed physics objects are provided by the Common Sample Group for analysis in DØ. These objects were specifically chosen, so that a large number of analysis can be performed in DØ, and therefore a tighter selection has to be done for objects used by this analysis. In the following we will see these extra requirements and rejections done for this analysis, along with the efficiencies involved in this selection.

5.3.1 Electromagnetic Objects

For the selection of the electromagnetic (EM) objects, we followed the guidelines for certified EM objects, provided by the EM Identification Group (EMID Group) [82]. The full list of guidelines, refers to all reconstructed EM objects in DØ (*i.e.,* all regions of the detector and all alternative reconstruction algorithms.) In this analysis only the Central Region of the detector was used, and only one EM object reconstruction algorithm. The list of off-line selection criteria is as follows:

- Require "scone" reconstruction algorithm for EM objects;
- Require EM objects in the Central Calorimeter, $|\eta_d| < 1.1$;
- Require EM objects with $EM_{iso} < 0.15$, $EM_{fract} > 0.90$, $\chi^2_{HMx7} < 15.0$.

Here η_d is the detector η of the object defined in section 3.3 and the definitions of the variables EM_{iso}, EM_{fract}, and χ^2_{HMx7} are given in section 4.2.

To distinguish electrons from photons, a track matching requirement for the EM objects was used as mentioned in section 4.2.4. The variable used for this distinction, was the EMID $\chi^2_{(spatial)}$ variable. An EM object was considered to be an electron, if there was an associated track with $\chi^2_{(spatial)} > 10^{-3}$, otherwise it was considered to be a photon. The efficiency of such matching criteria was determined using a $Z \rightarrow e^- e^+$ dataset, events were selected from this sample with exactly one and two track matches. Using the above selection, the invariant mass of the di-EM system was plotted, and fitted with a gaussian peak plus some background to separate the Z-signal from the background. From the best of the above fits, the event yields and their statistical errors,

for one and two track matches are deduced. The systematic errors were determined by varying the background parametrization, extracting the event yields as before, and then taking the RMS value in respect to the best event yields as the systematic errors. Table 5.1 shows the event yields, statistical and systematic errors for selected events with exactly one (N_1) and two (N_2) track matches.

Track Matches	Event Yields	Statistical Error	Systematic Error
N_1	1308	48	83
N_2	9608	105	210

Table 5.1: Event yields, statistical and systematic errors for events with exactly one (N1) and two (N2) track matches.

For the calculation of the efficiency, we note that if N_Z is the number of $Z's$ then the event yields N_1 and N_2 exactly one and two track matches satisfy:

$$\begin{aligned} N_1 &= 2 \cdot \epsilon_{trk} \cdot (1 - \epsilon_{trk}) \cdot N_Z \\ N_2 &= {\epsilon_{trk}}^2 \cdot N_Z \end{aligned} \tag{5.3}$$

from which easily follows that the efficiency is given by the expression:

$$\epsilon_{trk} = \frac{2 \cdot N_2}{2 \cdot N_2 + N_1} \tag{5.4}$$

where N_1 and N_2 are the event yields for exactly one and two track matches. The di-EM mass spectra for two and exactly one match is shown in Fig. 5.1.

From the event yields found in Table 5.1 and equation (5.4) the track matching efficiency was determined to be:

$$\epsilon_{trk} \; = \; 0.936 \; \pm \; 0.002\,(stat) \; \pm \; 0.004\,(syst) \tag{5.5}$$

For electrons, geometry and scale corrections were applied, as it was mentioned in section 4.2.5, and applying them, their energy was required to be greater than 20 GeV. These corrections are small and they were verified using Monte Carlo (MC) and by measuring the Z mass in the di-electron channel. In order to establish our trust in the Monte Carlo (MC) generated sample, the agreement between

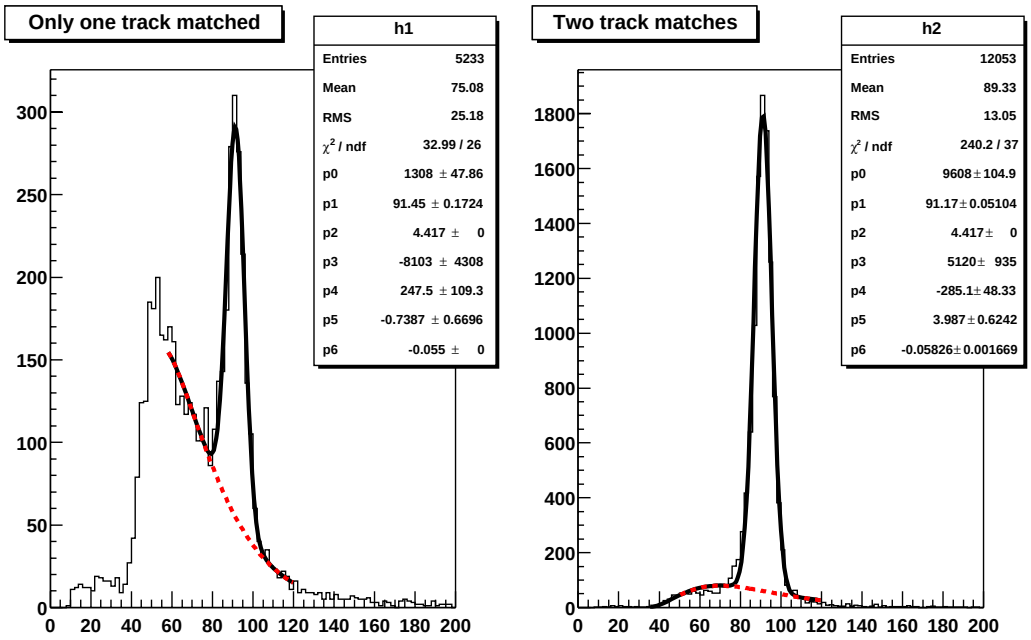

Figure 5.1: DiEM mass spectra for the events with exactly one (left) and exactly two EM clusters with track match.

real data and generated MC, had to be checked for the above set of cuts. This is true especially with respect to the event topology, *i.e.,* the presence of jets in the event. To study this agreement, a MC sample of $Z \rightarrow e^- e^+$ events was generated using PYTHIA [83], and the efficiency of the seven-variable H-matrix χ^2 cut ($HMx7$), was compared with data for different event topologies. Since the $HMx7$ variable essentially distinguishes hadronic from electromagnetic clusters, it's efficiency compared to the number of jets in the event and/or the distance with the closest jet, was the appropriate variable of interest. Jets used for this study were standard jets (JCCB) as described in section 5.3.2.

The determination of the efficiency for the $HMx7$ cut was done essentially as in the case of track matching. Events were selected with one or two $HMx7$ cuts and the efficiency was extracted in a similar fashion. The result of these studies for the efficiency of the $HMx7$ cut versus the number of jets in the event, is shown in Fig. 5.2, while the result versus the distance to the closest jet is shown in Fig. 5.3. From these studies we see that there is no significant event-topology dependence. MC reproduces the data in a reasonably good fashion, except for a small scale factor. Ratios of data to

MC efficiencies versus the number of jets in the event are shown in Fig. 5.4, and versus the distance to the closest jet in Fig 5.5. To check any H-Matrix cut dependance, the above study was repeated for a tighter H-matrix cut $HMx7 < 10$, and the results are shown in Fig 5.6 and Fig 5.7.

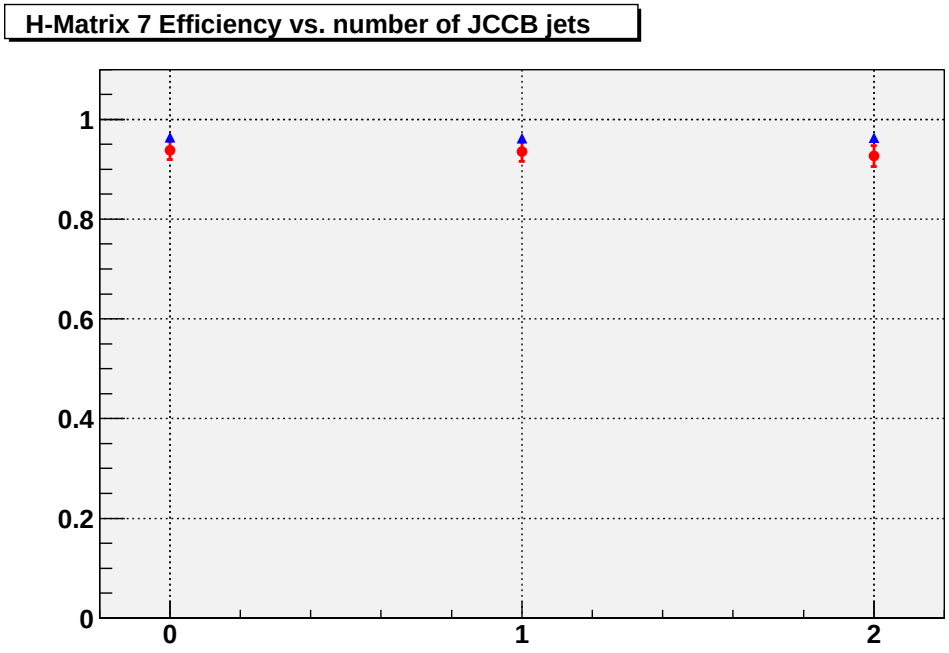

Figure 5.2: Efficiency for H-matrix cut $\chi^2 < 15$ for $Z \rightarrow e^- e^+$ events in Data (red) and in MC (blue) vs. the number of JCCB jets in the event.

Another discriminating variable used in the analysis is track-based isolation. Track-based isolation is defined as, the scalar sum of p_T for all tracks within a hollow cone $0.05 < R < 0.4$ around the photon candidate and for which their z-intersect at the distance of the closest approach z_{DCA}, is less than 2 cm from the primary vertex (PV):

$$TRK_{iso} = \left\{ \sum_{tracks} p_T^{(track)} \right\}_{|z_{PV} - z_{DCA}| < 2\ cm}^{0.05 < R < 0.4} . \tag{5.6}$$

For photon candidates this was required to be less than 2 GeV.

As in the case of the H-Matrix cut, the agreement between real data and generated MC had to be checked. This was done essentially in the same way that was done for the H-Matrix cut, using a $Z \rightarrow e^- e^+$ sample both for Data and MC. After calculating the efficiencies for this cut, track-based

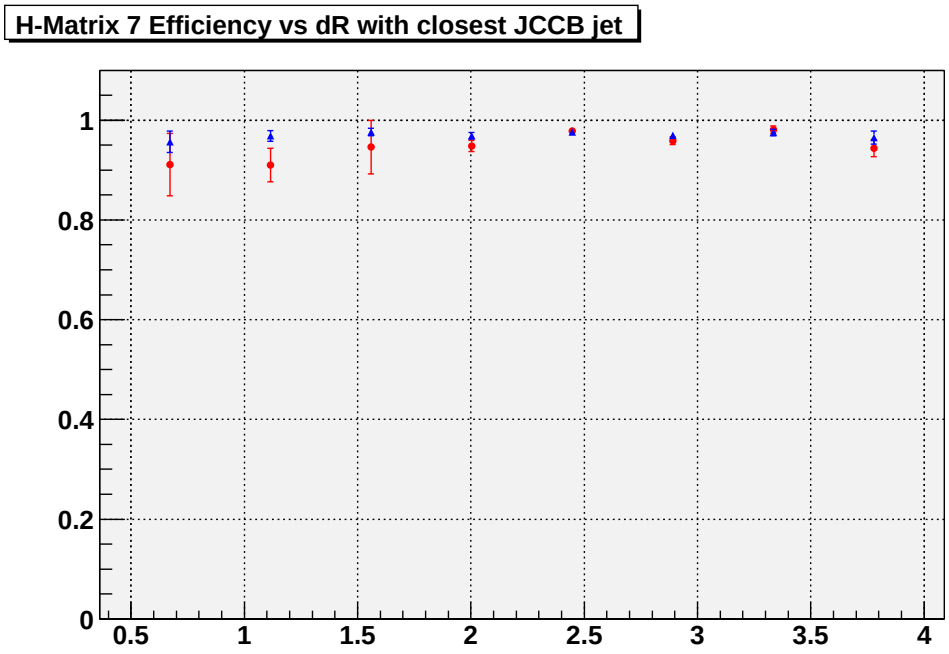

Figure 5.3: Efficiency for H-matrix cut $\chi^2 < 15$ for $Z \to e^- e^+$ events in Data (red) and in MC (blue) vs. the distance $\Delta R = \sqrt{\Delta\phi^2 + \Delta\eta^2}$ to the closest JCCB jet in the event.

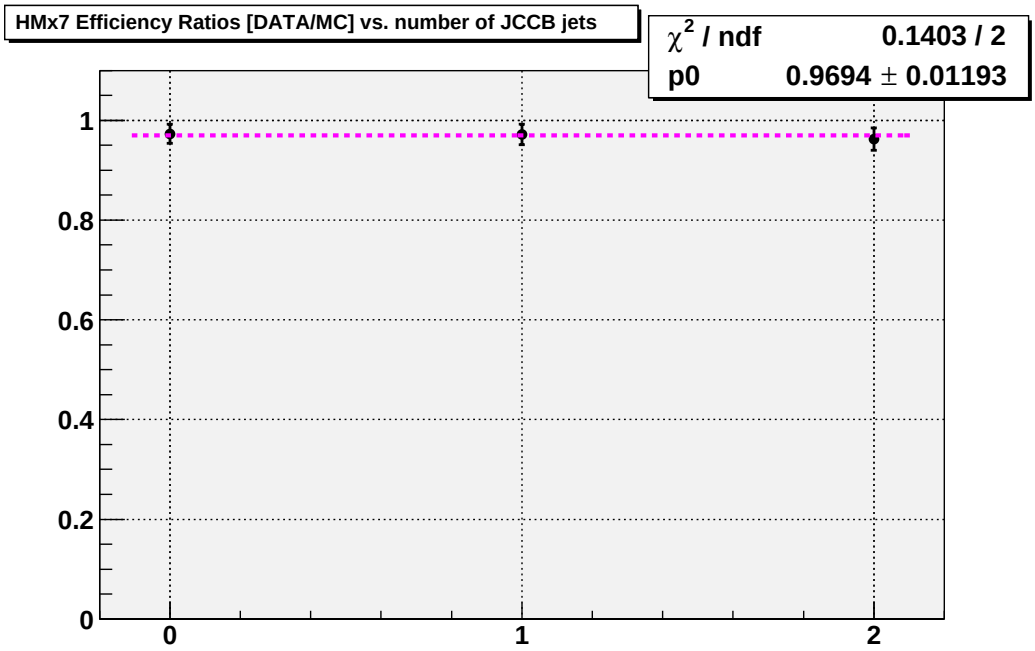

Figure 5.4: Ratio of Data to MC efficiency for H-matrix cut $\chi^2 < 15$ for $Z \to e^- e^+$ events vs. the number of JCCB jets in the event.

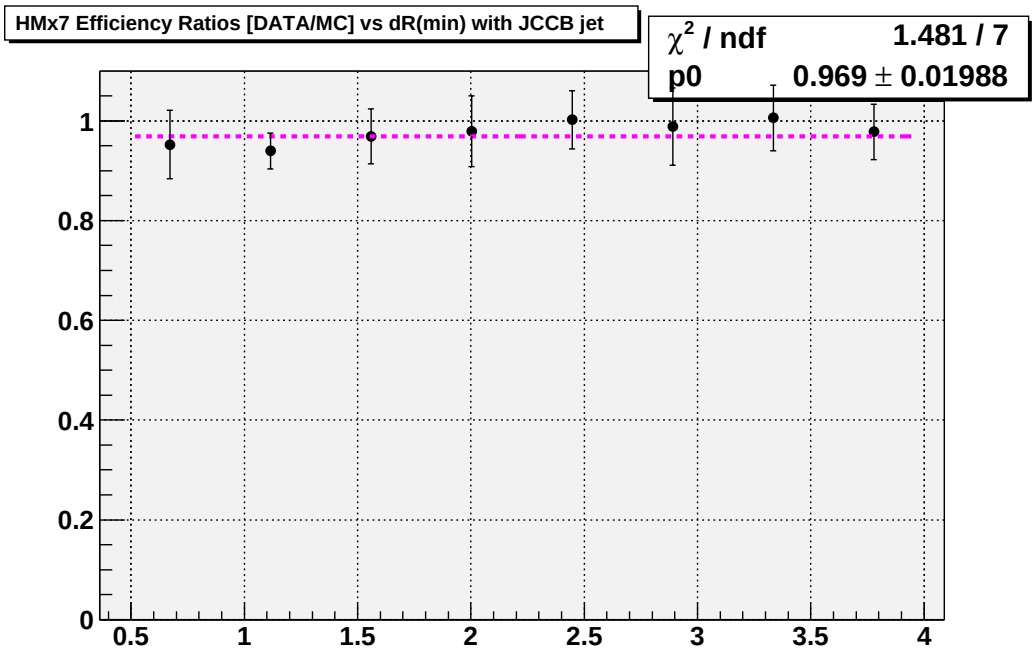

Figure 5.5: Ratio of Data to MC efficiency for H-matrix cut $\chi^2 < 15$ for $Z \rightarrow e^- e^+$ events vs. the distance $\Delta R = \sqrt{\Delta\phi^2 + \Delta\eta^2}$ to the closest JCCB jet in the event.

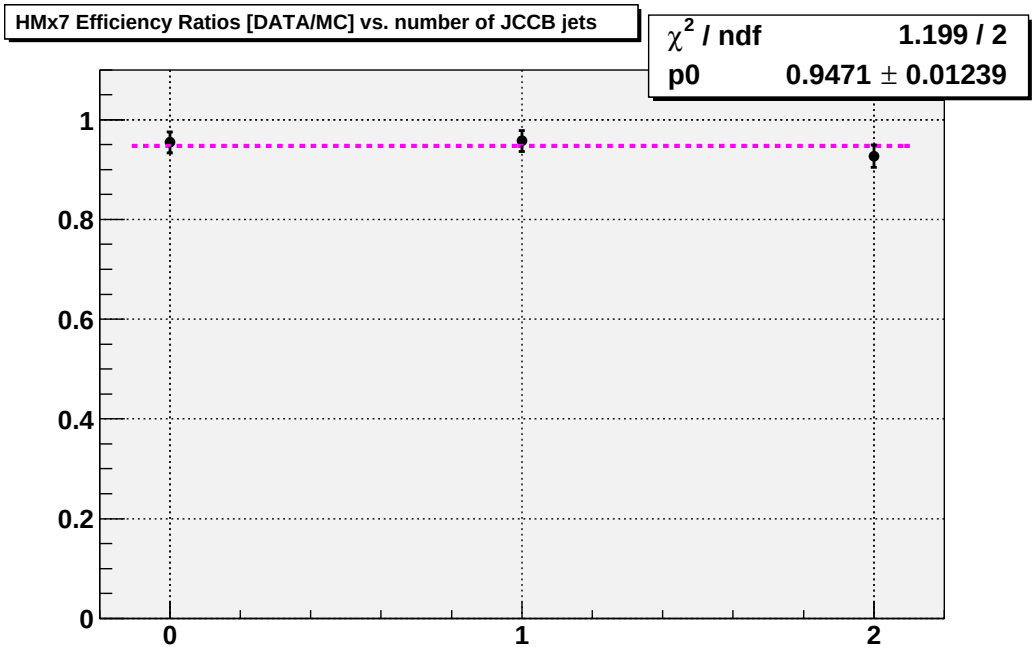

Figure 5.6: Ratio of Data to MC efficiency for H-matrix cut $\chi^2 < 10$ for $Z \rightarrow e^- e^+$ events vs. the number of JCCB jets in the event.

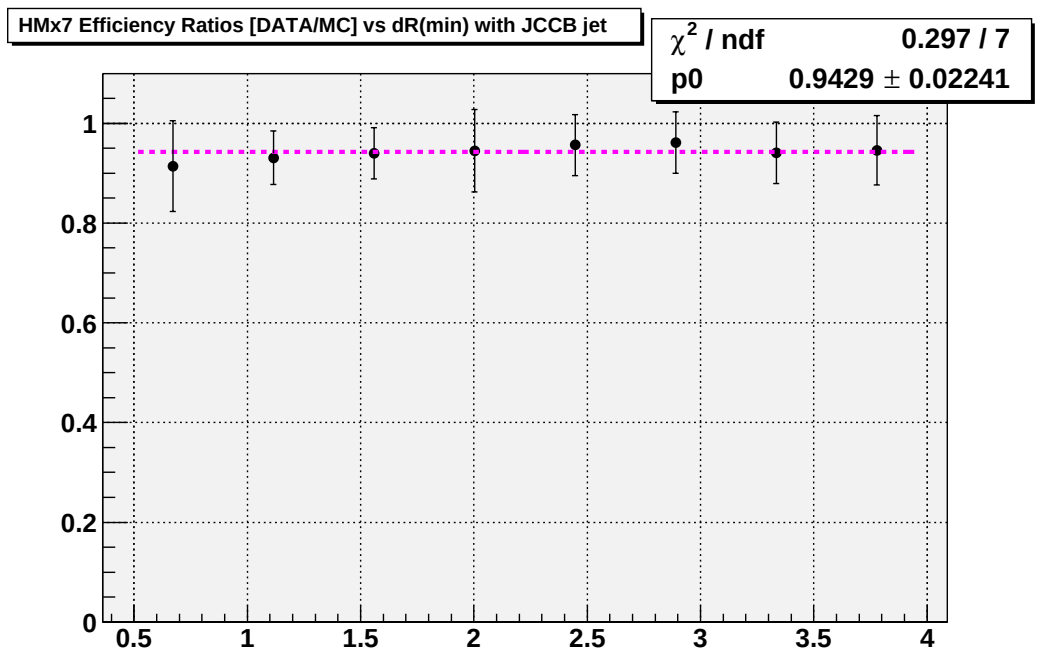

Figure 5.7: Ratio of Data to MC efficiency for H-matrix cut $\chi^2 < 10$ for $Z \rightarrow e^- e^+$ events vs. the distance $\Delta R = \sqrt{\Delta\phi^2 + \Delta\eta^2}$ to the closest JCCB jet in the event.

isolation for data and MC was found to be consistent within errors. Figure 5.8 shows the track-based isolation efficiency versus the number of JCCB jets, and Fig. 5.9 shows the same variable versus the distance to the nearest JCCB jet. As expected, the track-based isolation efficiency decreases for a large number of jets in the event, or when the distance of the closest jet is low, but as can be seen the effect is not significant.

To check that there are no correlations between these two cuts, (*i.e.,* H-matrix and track-based isolation), the combined efficiency of H-matrix and track-based isolation was calculated, by the same means as before. After obtaining the combined efficiency it was compared with the individual results obtained for each cut separately and it was found to agree within the errors. Figures. 5.10 and 5.11 show show the results for the ratio of combined efficiency of H-matrix and track-based isolation cuts.

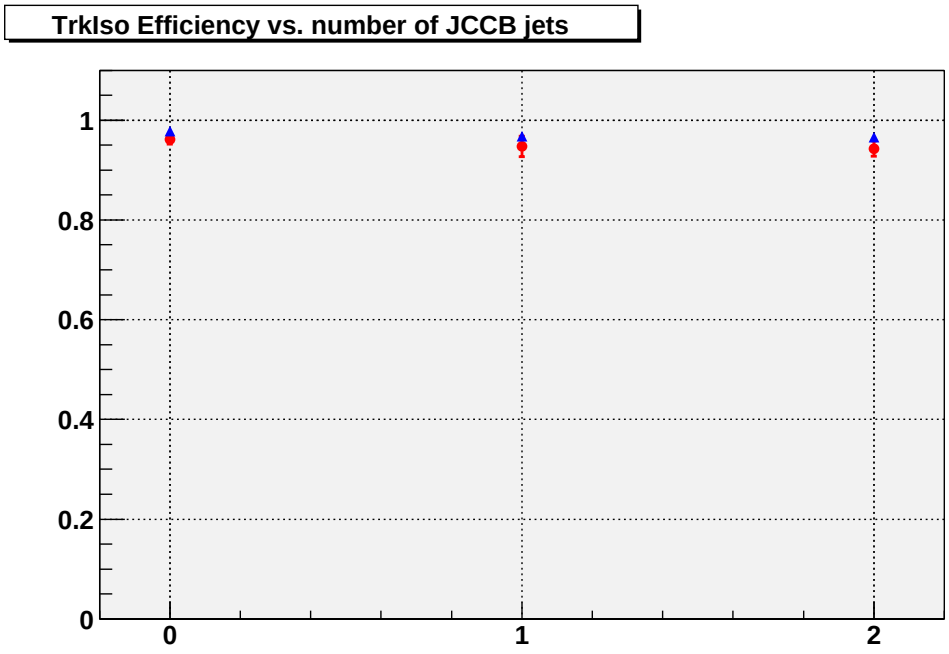

Figure 5.8: Track isolation efficiency for $Z \rightarrow e^{-}e^{+}$ events in Data (red) and in MC (blue) vs. the number of JCCB jets in the event.

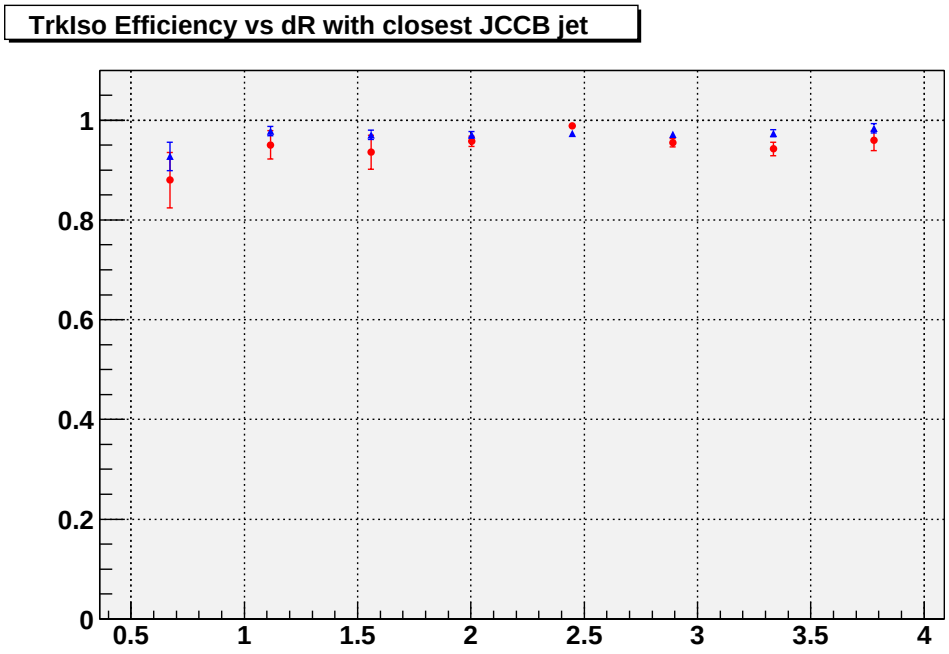

Figure 5.9: Track isolation efficiency for $Z \rightarrow e^{-}e^{+}$ events in Data (red) and in MC (blue) vs. the distance $\Delta R = \sqrt{\Delta\phi^2 + \Delta\eta^2}$ to the closest JCCB jet in the event.

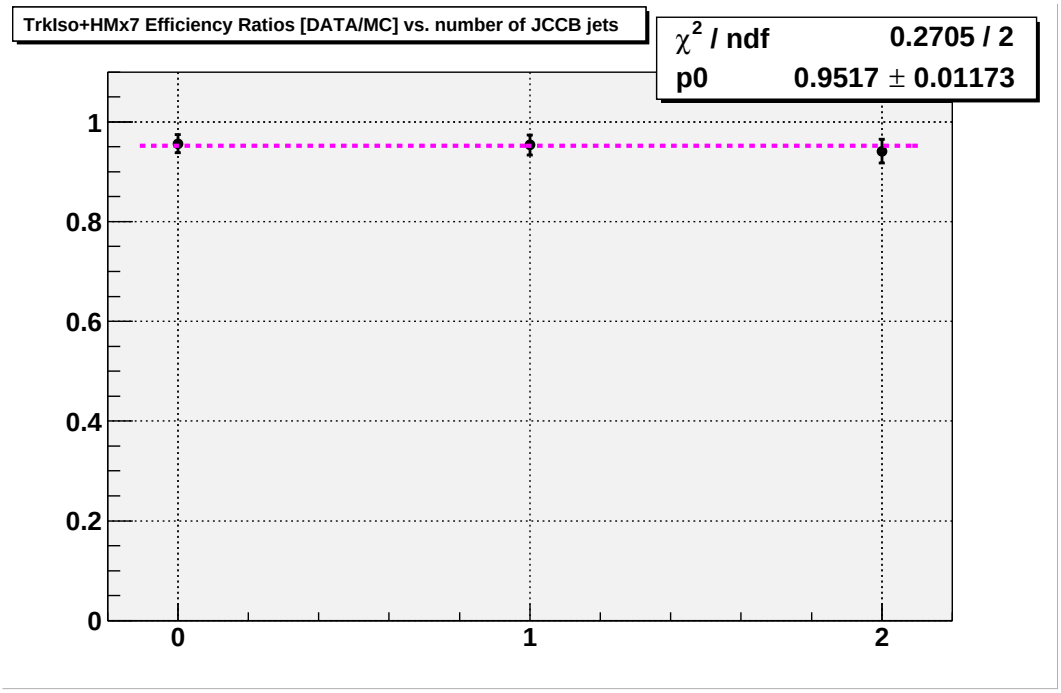

Figure 5.10: Ratio of Data to MC efficiency for H-matrix cut $\chi^2 < 15$ and track isolation cut for $Z \to e^- e^+$ events vs. the number of JCCB jets in the event.

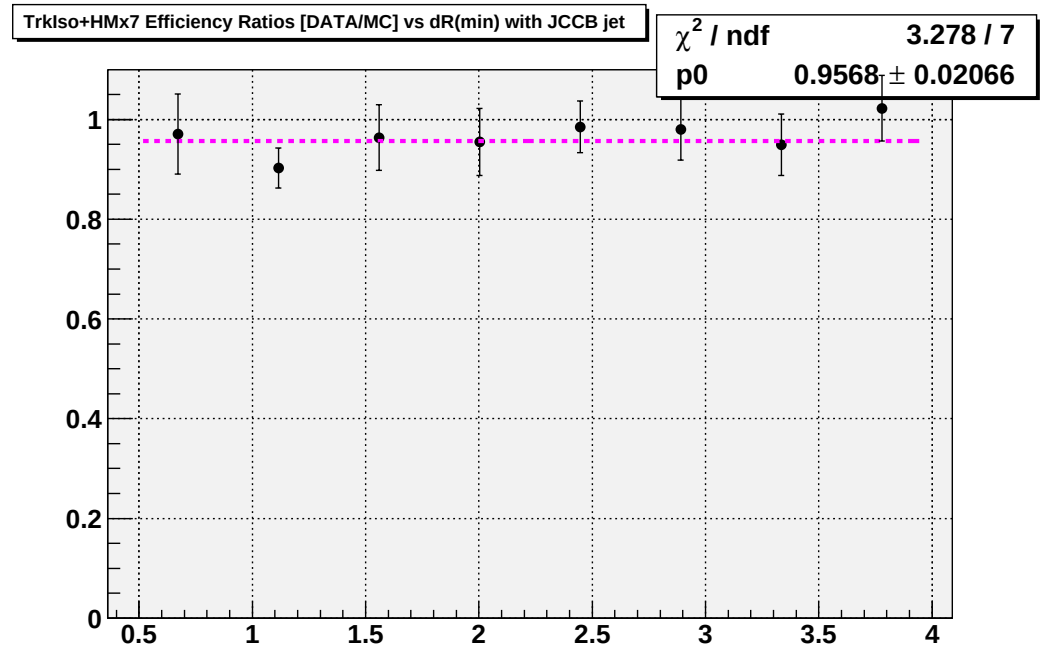

Figure 5.11: Ratio of Data to MC efficiency for H-matrix cut $\chi^2 < 15$ and track isolation cut for $Z \to e^- e^+$ events vs. the distance $\Delta R = \sqrt{\Delta\phi^2 + \Delta\eta^2}$ to the closest JCCB jet in the event.

5.3.2 Jets and $\not\!\!E_T$

As it was mentioned in section 4.3, although jets don't appear explicitly in the physics signature under study, their correct reconstruction affects the accurate determination of the missing transverse energy. The method of jet reconstruction was discussed in section 4.3.

After jets are corrected, $\not\!\!E_T$ is again calculated, using all cells above zero energy that are not in good jets and that are not in the Coarse Hadronic (CH) layer. As a final stage the corrected jets are then added in to complete the calculation [74].

During the event selection, events with correlated calorimeter noise, or events having the sum of transverse energies of all "bad" jets greater than 30 GeV, were rejected. The impact of this selection is relatively small (3%), and it does not depend on the sample (i.e. $Z \to e^- e^+$ versus QCD). The efficiency of this selection is:

$$\epsilon_{rejection}\,(CAL\,noise, \text{“}bad''jets) \;=\; 0.97 \pm 0.02\,. \tag{5.7}$$

Chapter 6

Signal Generation

An essential part in every search for new physics in a $p\overline{p}$ collider is the signal simulation. The importance of this task is crucial; searching for new physics requires first of all a good description of the already accumulated knowledge. It is the difference between the already known and the experimentally observed that guides us to the realization that something new exists. Secondly, in order to firmly establish the existence of any new suspected physics, a relatively good description for it is required, which later needs to be compared with the experimental data. Over the past years computer generation and simulation programs have been developed in order to address both these goals in high-energy-physics experiments. In this chapter we briefly describe the programs used in the DØ experiment to achieve this goal, along with the specific requirements for signal generation needed for this analysis.

6.1 Event Generation and Simulation

In every modern high-energy physics experiment signal generation is based on *Monte Carlo (MC)* computing techniques. The term Monte Carlo refers to any method which solves a problem by generating suitably random numbers and observing the fraction of the numbers obeying some property or properties. The method is useful for obtaining numerical solutions to problems which are too complicated to solve analytically, which is exactly the situation in high-energy physics. In general

event generation and simulation proceeds in three steps:

- Event Generation (simulation of the particle collisions);
- Detector Response Simulation (interaction of the particles passing through the detector);
- Reconstruction and Trigger Simulation.

In the following sections these three steps will be briefly discussed.

6.1.1 Event Generation

A various number of event generators for simulating hadron-hadron collisions exists. The steps followed in all these generators are similar, but their implementation details differ.

- A primary hard scattering is generated for the physics process under study;
- QCD radiative corrections to both the initial and the final state are added;
- Partons are fragmented and short-lived particles are decayed (hadronization).

The main difference between generators, is the model and parameterization of the hadronization stage. For this analysis the ISAJET v 7.58 [84] generator was used to determine masses for the SUSY particles (sparticles) and branching fractions while the PYTHIA v 6.202 [85, 83] generator with CTEQ5M [86, 87, 88] parton distribution functions, is used for event generation. This selection was done because ISAJET provides a better scheme for calculating the masses and branching fractions for SUSY than the PYTHIA's SUSY implementation. The interface between those two generators is described in [89].

6.1.2 Detector Response Simulation

Since our goal is to simulate a real physical process, a detailed simulation of the detector response when particles pass through it is necessary. The *DØ GEANT Simulation of the Total Apparatus Response (DØGSTAR)* [90] software package is responsible for this simulation in DØ. This is essentially a customized version of the package GEANT3 [91], a program developed at CERN. This package uses a description of the detector geometry and the materials involved in each detector

volume. It also simulates tracks and interactions of particles traversing through a magnetic field volume. When appropriate, ionization and secondary particles due to interactions with the detector material are produced. Processes simulated with this package are electromagnetic and hadronic showering, decays of short-lived particles, muon bremsstrahlung, and so forth.

The above simulation phase accounts only for the physical processes inside the detector. In reality what is seen are electric signals that are readout by the detector electronics. The DØ code responsible for simulating the detector electronics is DØSim [92]. This is a package that uses DØGSTAR's output as input and simulates the digitization for each detector, pileup (overlapping minbias events) and raw data simulation. This package is also responsible to account for any noise and inefficiencies present in the detector sub-systems (Calorimeter, SMT, CFT, Muon), and account for them appropriately.

6.1.3 Reconstruction and Trigger Simulation

The output of DØSim is of the same form as the raw data from the detector and is used as input to the last step of the simulation chain, the reconstruction and trigger simulation. As we have already discussed in Chapter 4, the DØRECO package is responsible for reconstruction. Details about the reconstruction of the relevant objects for this analysis can be found there. The purpose of the trigger simulation is due to the fact that not all events are recorded by the data acquisition system (DAQ). Therefore to get a realistic picture, simulated events have to pass through a system that simulates the function of the trigger system. In DØ the program charged with this task is called DØTrigSim [93]. This package uses the same trigger configuration which was used at the time of data taking to simulate the trigger response. Because of it's ability to simulate the trigger system, DØTrigSim can also be used to develop and study the performance of new triggers, and also test and debug online trigger software before it is used online.

6.2 Generated Monte Carlo

The expected event yield for GMSB signal events was estimated using generated Monte Carlo for several model points on three different model lines (see Table 6.1). For all model points on the line, the Monte Carlo signal was inclusive of all processes and decays (*i.e.,* $\gamma\,\gamma + \not\!\!E_T + X$ topology).

Our main model, which this analysis refers to, are the points labeled 8 through 14 (Snowmass model line E) [94, 95]. To roughly scan other areas of the parameter space, both in low values of $tan\beta$ and different number of messenger multiplets, other lines were simulated also.

As described in the previous sections these MC generated events were processed through a full detector simulation, reconstructed and then processed with the same analysis algorithm as the real data. For all the studied points in the model line the most significant contributions to the cross section comes from two sources:

- First chargino pair production;
- First chargino, Second neutralino production.

In Table 6.1 the total cross section is the leading order PYTHIA calculated cross section [83]. To account for next-to-leading-order (NLO) corrections, a K-factor was applied, it's values were taken from [96] and can be seen in Table 6.1.

6.2.1 Signal Efficiency

For the calculation of the signal efficiency, we used the full MC simulation of the signal events. The efficiency for reconstructing and identifying a photon that we get in the signal Monte Carlo is a little lower than that for the electron in $Z \rightarrow e^- e^+$ MC. For a perfectly identifiable $high - p_T$ MC photon ($p_T > 25GeV$, $|z_{EM3}| < 100$) the efficiency to reconstruct an EM object using the "scone" algorithm is 0.90. The efficiency to pass EM fraction and isolation cuts is 0.99 and the efficiency to pass the H-Matrix cut is 0.89. Compared to $Z \rightarrow e^- e^+$ MC the smaller EM cluster reconstruction efficiency is explained by the presence of extra objects in signal events, and the difference in H-Matrix efficiency comes from the fact that there are small differences between electron and photon shower shapes (a

Point	Λ TeV	$\frac{M}{\Lambda}$	$tan\beta$	N_5	$m_{\chi_1^0}$ GeV	$m_{\chi_1^+}$ GeV	σ_{TOT}^{LO} pb	K-factor	Efficiency	95% CL Limit pb
1	55	2	5	1	69.4	122.0	0.861	1.240	0.081 ± 0.008	0.209
2	60	2	5	1	76.9	136.2	0.534	1.229	0.103 ± 0.010	0.165
3	65	2	5	1	84.5	150.5	0.338	1.219	0.118 ± 0.011	0.144
4	70	2	5	1	92.0	164.9	0.225	1.209	0.128 ± 0.012	0.133
5	75	2	5	1	99.4	179.1	0.150	1.199	0.137 ± 0.013	0.124
6	80	2	5	1	106.7	193.0	0.102	1.189	0.134 ± 0.013	0.126
7	85	2	5	1	114.1	207.2	0.070	1.179	0.126 ± 0.012	0.134
8	55	2	15	1	71.8	126.3	0.735	1.236	0.092 ± 0.009	0.184
9	60	2	15	1	79.1	140.2	0.468	1.227	0.100 ± 0.009	0.170
10	65	2	15	1	86.4	154.3	0.301	1.217	0.111 ± 0.011	0.153
11	70	2	15	1	93.7	168.2	0.204	1.207	0.124 ± 0.012	0.137
12	75	2	15	1	101.0	182.3	0.138	1.197	0.137 ± 0.013	0.124
13	80	2	15	1	108.2	196.0	0.094	1.187	0.149 ± 0.014	0.114
14	85	2	15	1	115.5	209.9	0.066	1.177	0.154 ± 0.015	0.110
15	36	10	5	2	88.4	153.1	0.311	1.217	0.119 ± 0.011	0.143
16	38	10	5	2	94.2	163.9	0.230	1.210	0.148 ± 0.014	0.115
17	40	10	5	2	100.0	174.7	0.171	1.202	0.141 ± 0.014	0.120
18	42	10	5	2	105.7	185.4	0.129	1.195	0.160 ± 0.015	0.106
19	44	10	5	2	111.4	196.0	0.099	1.187	0.143 ± 0.014	0.118
20	46	10	5	2	117.1	206.6	0.076	1.180	0.153 ± 0.015	0.111
21	48	10	5	2	122.7	217.3	0.058	1.172	0.138 ± 0.013	0.123

Table 6.1: Points on the GMSB model slopes: their cross-sections, efficiencies and cross-section limits. All points correspond to $\mu > 0$. Points 8-14 correspond to the Snowmass model line E.

difference in which H-Matrix is sensitive) [97].

For the systematic error on the efficiency of the H-Matrix, $Z \rightarrow e^{-}e^{+}$ Data and MC was used. The value of the H-Matrix cut at which the electron efficiency in $Z \rightarrow e^{-}e^{+}$ MC would be close to 0.89 was found to be $HMx7 < 8$ (the $Z \rightarrow e^{-}e^{+}$ MC efficiency is 0.90 at this cut). Then this efficiency was multiplied by a scale factor of 0.97, which is the difference between data and MC for $HMx7 < 15$ cut, to get a "prediction" of the efficiency in data of 0.87. The efficiency measured using Z decays in data was a little smaller, 0.84. The difference (3.5%) between those two values was taken to be the systematic error on the H-Matrix cut for the signal. For the isolated EM cluster reconstruction, a 20% error on the MC prediction for inefficiency was assigned, which translates into a 2% error on the efficiency. The total systematic error on the photon identification is then 4% per photon.

A photon can be mis-identified as an electron if there is a random track that overlaps it or if it converts close to the interaction point and an electron from the the conversion is reconstructed. The former effect is very small (about 0.003). For the later, Monte Carlo simulation predicts a photon efficiency of 0.97. To correct for an underestimation of detector material in the MC which causes an increased in the inefficiency, we apply a factor of 0.97 ± 0.02.

Chapter 7

Standard Model Backgrounds

Chapter 2 shows the expected experimental signatures in the class of GMSB models. Recall that for the GMSB models of interest, the SUSY signal appears in the detector as two isolated photons with high p_T accompanied by a large amount of $\not{E}_T$ corresponding to the undetected energy of the escaping gravitinos. Figure 7.1 shows photon transverse energy for an MC-simulated model point (point #11 in Table 6.1) close to the exclusion limit obtained in the analysis. Unfortunately, as almost always is the case when searching for new physics, there are also other physical processes capable of creating a signal similar in characteristics as the one under study. For detecting and recognizing a possible signal of new physics hidden in the collected data, a good knowledge of these other processes (backgrounds) must be achieved. In the following sections, the contribution of all the other processes predicted by the Standard Model producing events with similar characteristics to our signal will be discussed. This knowledge will eventually help us to decide if the observed signature is solely comprised by events predicted by the Standard Model processes or not. In the latter case, the prospects of discovering new physics appear, while in the former case, where only Standard Model contributions are found, limits on the parameters of the model (*e.g.* SUSY particle masses) can be set, signifying that if this new undiscovered physics exists, it has to lie beyond these limits.

The main physics objects appearing in the signature of this analysis are photons and large $\not{E}_T$, so

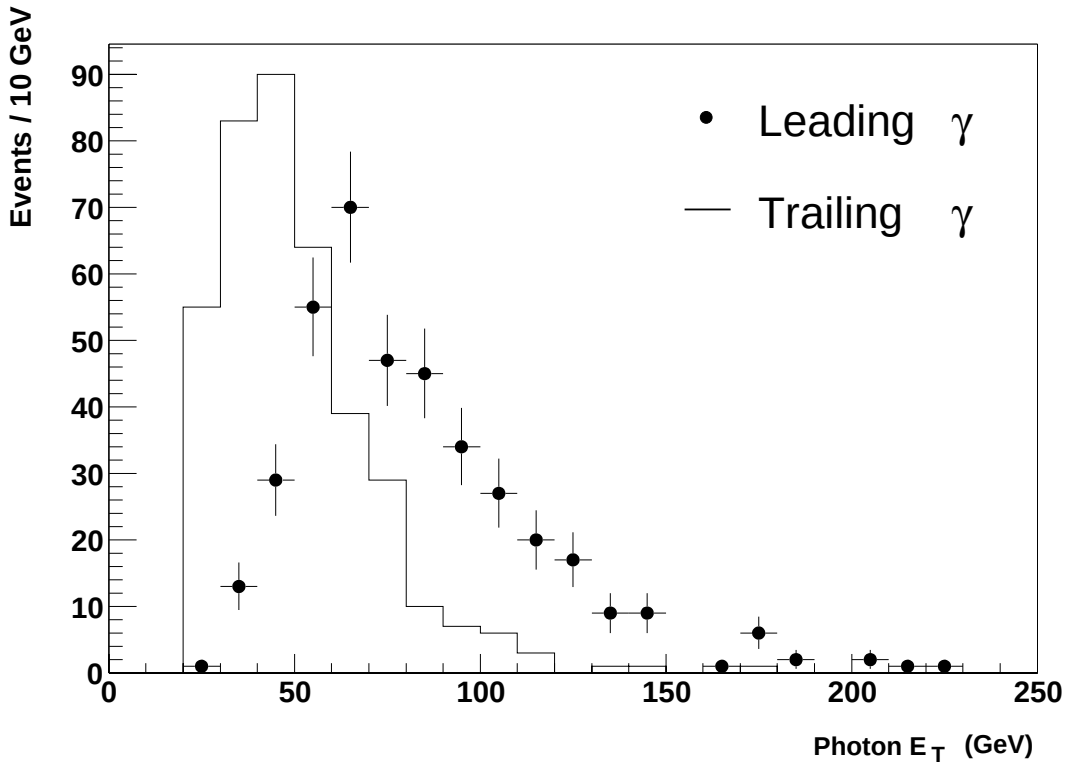

Figure 7.1: Photon E_T for model point close to the exclusion limit obtained in the analysis ($\Lambda = 0.8 \cdot 10^5$, $M_5 = 0.16 \cdot 10^6$, $N_5 = 1$, $tan\beta = 5.0$, $\mu > 0$).

the first step into devising a strategy for dealing with backgrounds is to identify all Standard Model contributions to this topology. At this point it should be noted that out of the two main objects of interest in this analysis, only one of them is a real physical object (photon), while the other one ($\not\!\!E_T$) comes either from real particles escaping the detector, or from mis-measurements of real objects and inefficiencies of the detector itself. Although detector inefficiencies contribute to $\not\!\!E_T$, they almost exclusively correspond to low $\not\!\!E_T$ (for a calibrated detector); therefore the main sources for large $\not\!\!E_T$ are mis-measurements of real objects (jets) and escaping particles (neutrinos). Identifying the Standard Model contributions to these backgrounds, involves looking for processes leading to final states involving photons, jets, and neutrinos. Neutrinos come from Electroweak processes, jets come from QCD processes, and photons come from both. Therefore a natural way to organize background contributions is separating them according to the origin of $\not\!\!E_T$ in QCD and Electroweak processes, keeping in mind that real physical objects are not determined with 100% accuracy, objects can be mis-identified during reconstruction ("fake" objects), and this has to be taken into consideration as

well.

The QCD processes involved in this analysis are:

- Photons plus jets or multi-jet events (dominant);
- Direct di-photons.

and the Electroweak processes:

- $W + jets \rightarrow e\nu + jets$;
- $W + \gamma \rightarrow e\nu + \gamma$;
- $Z + jets \rightarrow ee + jets \quad \text{or} \quad \nu\nu + jets \quad \text{or} \quad \tau\tau + jets$;
- $Z + \gamma \rightarrow ee + \gamma \quad \text{or} \quad \tau\tau + \gamma$;
- $t\bar{t} \rightarrow ee + \not{E}_T + X$;
- $WZ \rightarrow (e\nu)(ee)$;
- $WZ + jets \rightarrow (e\nu)(ee) + jets$;
- $ZZ \rightarrow (ee)(\nu\nu)$;
- Drell-Yan.

The first category involves backgrounds with fake photons and fake $\not{E}_T$ due to mis-measurement, the second involves backgrounds with photons and $\not{E}_T$ both fake and real.

Since photons are produced in both types of processes (and perhaps from yet undiscovered new physics), the idea of this analysis is to count the number of events in the total di-photon sample (inclusive of all physical processes known and unknown) and subtract the QCD and Electroweak contributions. In the sections below we will deal with exactly that accounting for the three samples in question (inclusive, QCD and Electroweak).

7.1 Di-photon Events

For the inclusive high-p_T di-photon sample selection cuts used in this analysis were described in Section 5.3. Nontheless we will mention them again:

- Require "scone" reconstruction algorithm for EM objects;
- Require EM objects in the Central Calorimeter, $|\eta_d| < 1.1$;
- Require EM objects with $EM_{iso} < 0.15$, $EM_{fract} > 0.90$, $\chi^2_{HMx7} < 15.0$.

Recall that η_d is the detector η of the object defined in Section 3.3 and the definitions of the variables EM_{iso}, EM_{fract}, and χ^2_{HMx7} are given in Section 4.2. Additionally to require high-p_T objects, we set a cut of $E_T > 20$ GeV for EM cluster which is also the trigger cutoff at L3 for some of the triggers. As we described in Section 4.5, the quality of the primary vertex reconstruction and the correct jet reconstruction affect the quality of the $\not\!\!E_T$ determination. To minimize the effect of non-Gaussian tails on the $\not\!\!E_T$ resolution due to catastrophic mis-measurement and wrong primary vertex selection, two more topological cuts are significant:

- The azimuthal opening angle between the direction of $\not\!\!E_T$ and the leading jet should be less than 2.5 radians;
- The azimuthal opening angle between the direction of $\not\!\!E_T$ and either photon should be at least 0.5 radians.

The justification for these cuts comes from the fact that SUSY originated $\not\!\!E_T$ and $\not\!\!E_T$ originating from background have completely different angle distributions with respect to the leading jet. A SUSY signal tends to have a uniform opening angle distribution, while the background is highly peaked at π. This is because it comes mainly from the jet mis-measurement, as can be seen in Figure 7.2 which comes from a QCD sample described in the next section. The $\not\!\!E_T$ distribution for these events is shown in Figure 7.3 while Table 7.1 shows event counts for different $\not\!\!E_T$ regions.

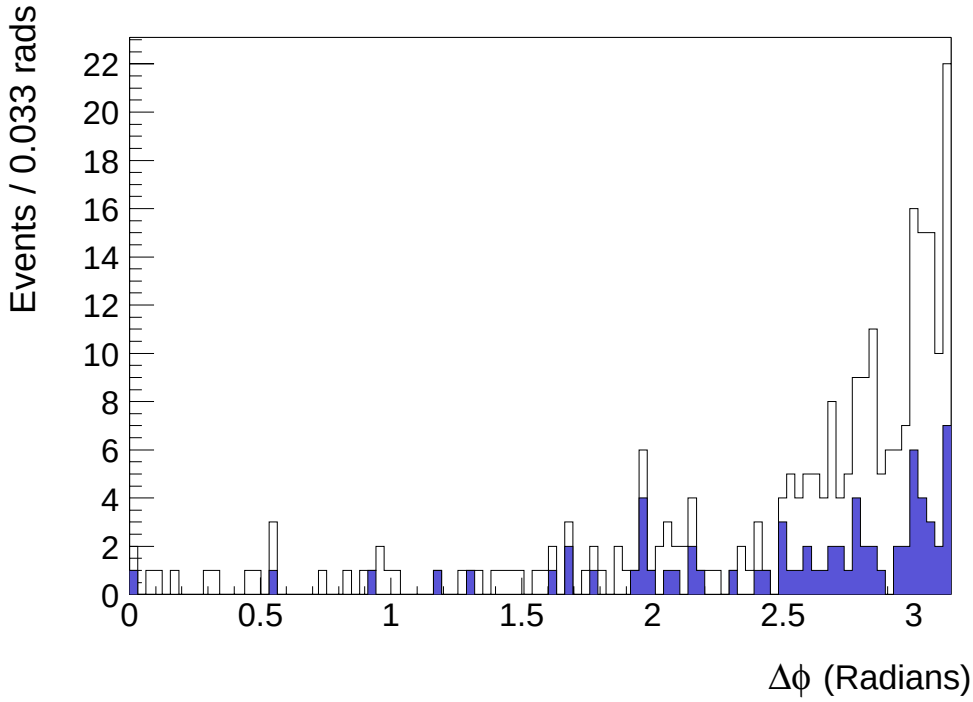

Figure 7.2: Azimuthal opening angle between the direction of $\not\!\!E_T$ and the leading jet for events with $\not\!\!E_T > 25$ GeV and $\not\!\!E_T > 35$ GeV (QCD sample).

	Total events	$\not\!\!E_T$ < 15 GeV	> 20 GeV	> 30 GeV	> 40 GeV	> 45 GeV	> 50 GeV	> 55 GeV
$\gamma\gamma$	1909	1800	34	6	2	1	1	1
$e\gamma$	889	782	70	34	15	10	5	4
QCD	18437	17379	343	73	27	22	15	11
QCD BG to $\gamma\gamma$			35.5 ± 2.1	7.6 ± 0.9	2.8 ± 0.5	2.3 ± 0.5	1.5 ± 0.4	1.1 ± 0.3
QCD BG to $e\gamma$			15.4 ± 1.0	3.3 ± 0.4	1.2 ± 0.2	1.0 ± 0.2	0.7 ± 0.2	0.5 ± 0.2
$e\gamma$ total			54.6 ± 8.4	30.7 ± 5.8	13.8 ± 3.8	9.0 ± 3.2	4.3 ± 2.2	3.5 ± 2.0
$e\gamma$ BG to $\gamma\gamma$			3.7 ± 0.6	2.1 ± 0.4	0.9 ± 0.3	0.6 ± 0.2	0.3 ± 0.1	0.2 ± 0.1
Total BG to $\gamma\gamma$			39.2 ± 2.2	9.7 ± 1.0	3.7 ± 0.6	2.9 ± 0.5	1.9 ± 0.4	1.4 ± 0.4

Table 7.1: The event counts in the $\gamma\gamma$, $e\gamma$ and QCD samples, and determination of the total background to diphoton sample.

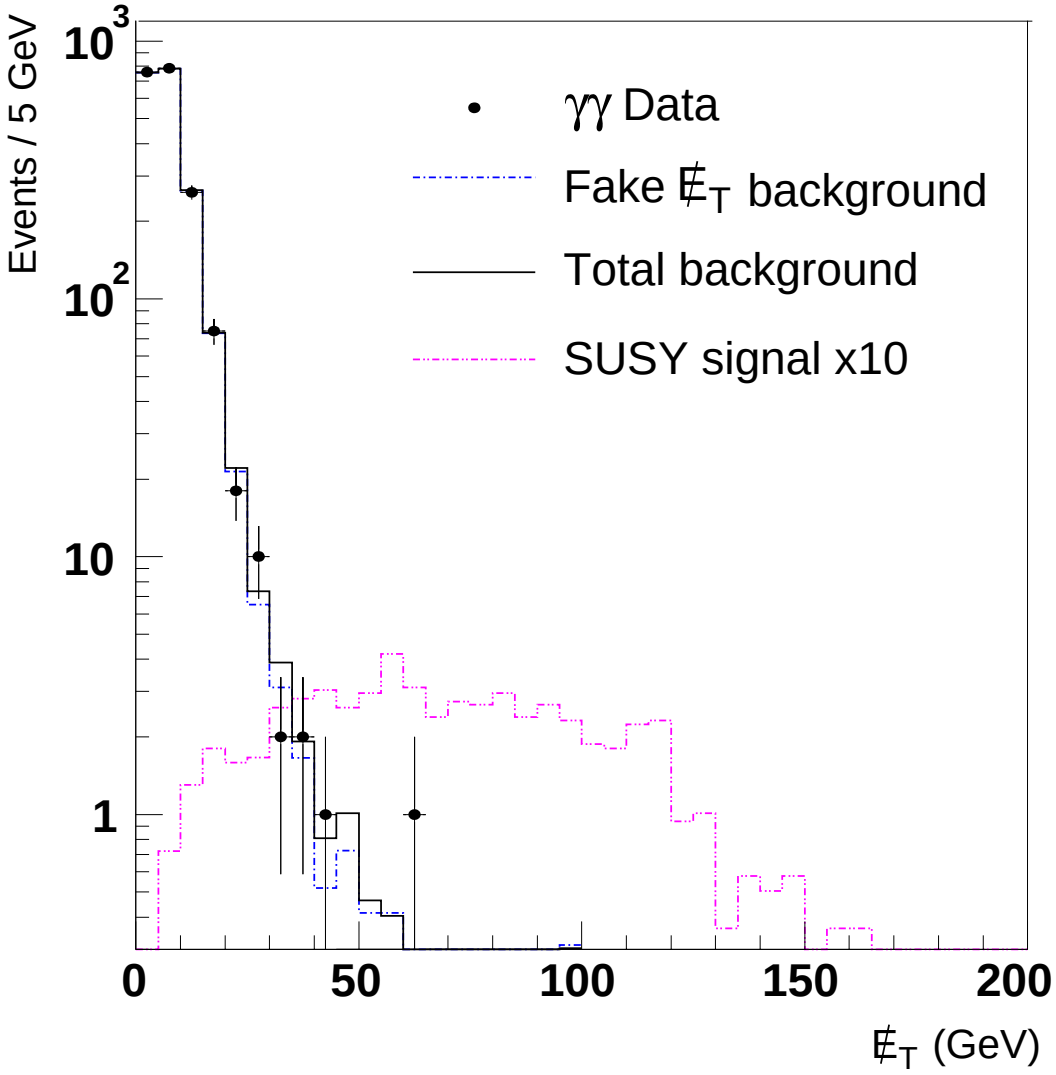

Figure 7.3: $\not\!\!E_T$ distribution in the diphoton sample after all cuts (points). Red histogram is QCD background, blue histogram is the total estimated background. Purple histrogram shows ten times the contribution expected from the SUSY point #13 of Table 6.1.

7.2 QCD Background Events

As mentioned in the beginning of this Chapter, QCD background comes from either direct di-photons or photons plus jets. Another background that has the same signature as QCD, is the Drell-Yan (DY) process that produces electron-positron pairs that can be mis-identified as photons. To estimate this contribution from Drell-Yan, we suppress the lepton aspect, by requiring a track matching veto. Drell-Yan events have no inherent $\not\!\!E_T$, therefore after the track matching veto the remainder are just fake photon pairs, that look exactly like QCD events, therefore will automatically be accounted for when QCD background is calculated. The track matching veto also suppresses electroweak backgrounds with true $\not\!\!E_T$, since they involve at least one electron.

To measure QCD background, we assume that $\not\!\!E_T$ resolutions should be very similar for events with di-photons or events with photons and jets faking photons. The justification for this comes from the fact that in order for a jet to fake a photon, it has to fragment into a leading π^0 before it reaches the electromagnetic calorimeter. If it doesn't, then the hadronic jet can easily be distinguished from the electromagnetic one. Therefore we can obtain an estimate of the QCD background by requiring the same cuts as for the di-photon sample but with at least one EM cluster passing inverted photon ID cuts, *i.e.,* it has the same isolation and EM fraction cuts as a certified EM object but fails the $HMx7$ cut. In order to estimate the total QCD background, we assume that all low $\not\!\!E_T$ di-photon events are coming from QCD sources, and use the measured shape to predict QCD background at high values of $\not\!\!E_T$. Our QCD sample is attained by starting with the same dataset as for di-photons as well as similar selections. The requirements for photon candidates were:

- Require EM objects with $HMx7 > 20$ and $HMx8 < 200$;
- Require EM objects with $EM_{iso} < 0.15$, $EM_{fract} > 0.90$.

The resulting QCD sample is comprised of 18437 events. We then choose a low $\not\!\!E_T$ region, defined by $\not\!\!E_T < 15$ GeV then normalizing this low $\not\!\!E_T$ QCD sample to the di-photon distribution we can predict the QCD background rates for high $\not\!\!E_T$. Estimates obtained with the process outlined above are shown in Table 7.1 and plotted in Figure 7.2.

7.3 Electoweak Background Events

For the electroweak background contribution the yield can be measured using an $e\,\gamma$ sample. This sample will have also contributions from QCD, which can be subtracted exactly in the same fashion as the ones in the di-photon sample. The dataset $e\,\gamma$ sample is based on the same sample that the di-photon is extracted from. Using the same selections as for di-photons except that in this case exactly one of the EM objects is required to have a track match and to satisfy electron track isolation criterion. There are 889 events passing this selection with the majority of them coming from QCD processes and DY. After subtracting the QCD contribution to this sample, the remaining electron-photon contribution to the di-photon sample was found by simply multiplying the observed number of electron-photon events by the ratio of the following probabilities:

1. Probability for an electron to be identified as a photon (i.e., $1 - \epsilon_{trk}$);

2. Probability as an electron to obtain background estimate in the di-photon sample (i.e., ϵ_{trk}).

In other words the number of the observed electron-photon events is by multiplied by $(1-\epsilon_{trk})/\epsilon_{trk}$, where ϵ_{trk} is the track matching efficiency. Figure 7.4 shows the $\not\!\!E_T$ for the electron-photon sample and the relevant events yields can be found in Table 7.1.

As mentioned before, the two main Standard Model processes contributing to high $\not\!\!E_T$ are $W + jets \rightarrow e\nu + jets$ and $W + \gamma \rightarrow e\nu + \gamma$. A cross-check was done to verify that we can describe the excess of electron-photon events at high $\not\!\!E_T$ over the QCD background by the two processes above. For the $W + \gamma$ process we use Monte Carlo simulated events generated with PYTHIA [83]. These events (as in the case of SUSY signal) were processed through full detector simulation and normalized to the luminosity of our sample ($263\,pb^{-1}$). The contribution from $W + jets$, was more complicated and it was found from data. This is done by relaxing the ID cuts on the photon, thus creating an electron plus EM object sample (see Figure 7.5). Assuming that the excess of events over the QCD sample is dominated by $W + jets$ events, we then determine the contribution of such events to the electron-photon sample, by multiplying the number of observed $W + jets$ events by the probability that a jet will be reconstructed as an EM object and also pass photon ID cuts.

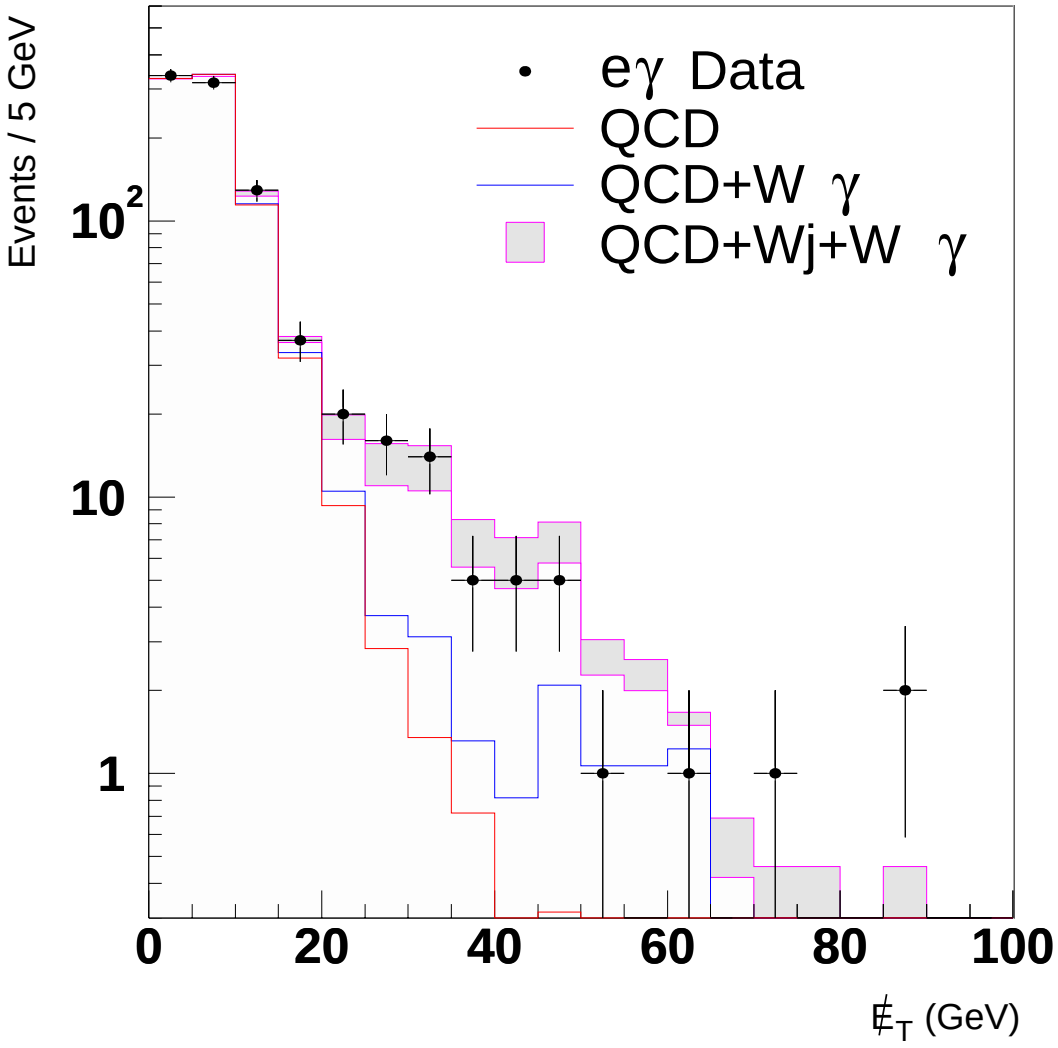

Figure 7.4: $\not\!\!E_T$ distribution in the electron-photon sample after all cuts (points).

In general this probability depends on the trigger requirements. The reason being, is that for EM triggers at L3, there are filters for the selection of EM objects different for each trigger. To determine this photon fake rate, we select a sample of events with $\not\!\!E_T < 15$ GeV and two EM objects. One of these EM objects must have $HMx7 > 100$, no track match, and the sum of all track p_T, in a cone of 0.4 around the object must be greater then 2 GeV. Then by choosing three different types of triggers:

- Single EM Triggers (EM_MX_SH and EMx_SHT_20);
- Di-EM Triggers with tight shape cuts (2EM_HI_SH and EMx_2SH8);
- Di-EM Triggers with loose shape cuts (2EM_HI and EMx_2L15_SH15).

the probability of the second EM objects to pass the photon ID cuts was determined. These probabilities are shown in Figure 7.6, from which we can take the photon fake rate to be 0.185 ± 0.045. Once this is done the contributions from $W + \gamma$ and $W + jets$ are shown in the Figure 7.4 with blue histogram and shaded band respectively.

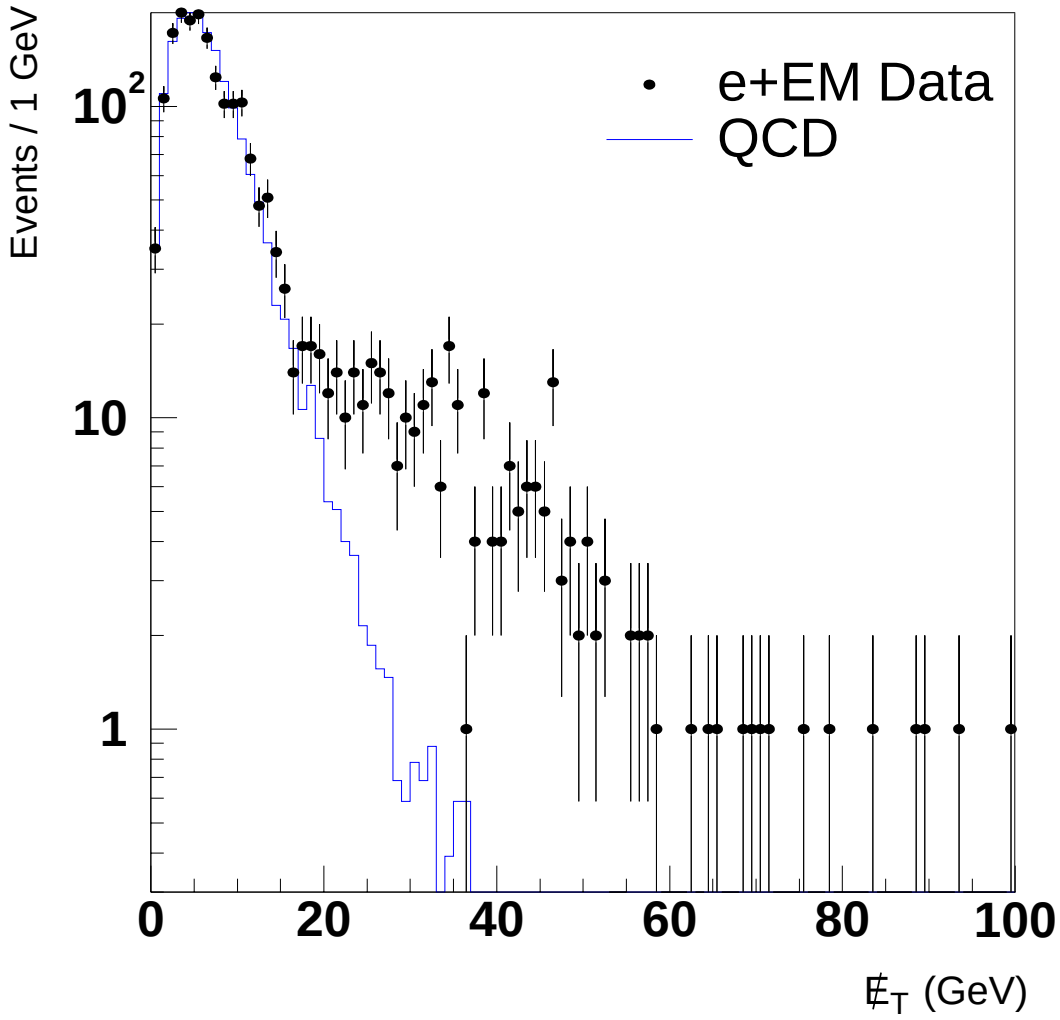

Figure 7.5: $\not\!\!E_T$ distribution in the electron plus EM object sample after all cuts (points).

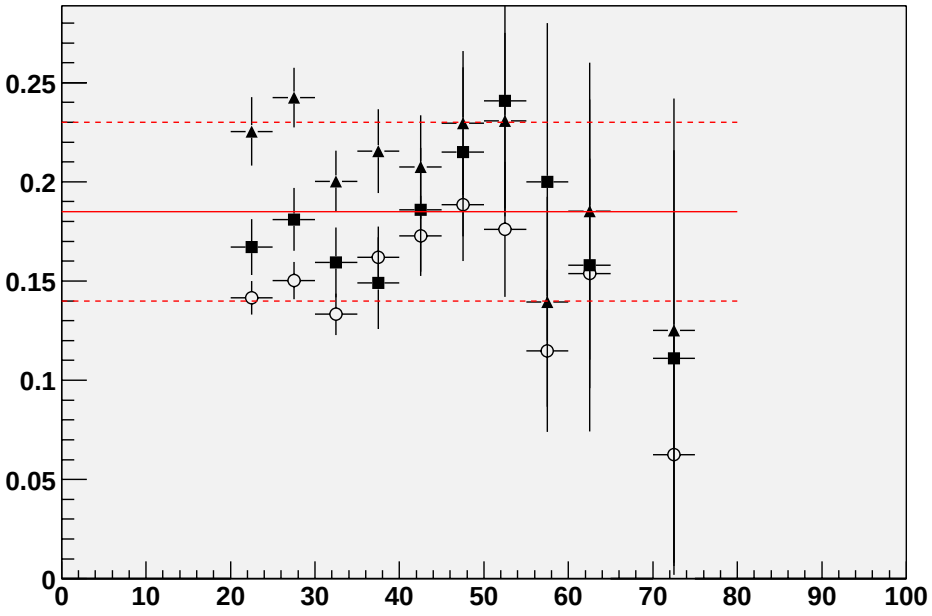

Figure 7.6: Probability for a jet reconstructed as an EM object to pass photon ID cuts for events passing single EM (triangles), tight di-EM (squares) and loose di-EM (circles) triggers.

Chapter 8

Optimization and Limits

From the results of the previous chapter it's clear that the observed number of events for the signature under study is in a good agreement with the Standard Model predictions. Therefore, since no evidence for signal is found, we proceed with setting a limits on the parameters of the model, which will be translated into lower limits on SUSY particle masses.

In the next sections the method for optimizing the analysis cuts will be discussed along with the limit setting procedure for the optimally determined cuts.

8.1 Cut Optimization

Optimizing the cuts for an analysis is a general subject that goes beyond the scope of this dissertation; therefore only the relevant methods for this analysis will be discussed following the reasoning described in [98]. Generally speaking, "optimizing" an analysis means that given many possible choices of sets of cuts, we have to select one based on a "reasonable preference criterion". In most of the cases the complexity of the optimization process originates from determining what constitutes a "reasonable preference", or in other words, which set of cuts is more *significant*. This determination depends on the analysis objective (*i.e.,* discovery vs. limit setting [98]), and also depends on the particular field of study [99]. In every case we want to be as un-biased as possible on the choice of the most significant set of cuts.

To define a significance criterion, a mapping S from the set $\mathcal{C}$ of all possible sets of cuts, to the real numbers must be devised. This mapping has to have the property that for any two sets of cuts C_1 and C_2, the set of cuts C_1 is better than the set of cuts C_2 if and only if $S(C_1) > S(C_2)$. Since our goal is to make an un-biased significance criterion we have to look for, and associate, the significance with a parameter of our analysis that we want to maximize. For this analysis an appropriate choice would be the parameter Λ of the model in study (having dimensions of mass), since it also determines all the other masses of the SUSY particles. Since this analysis is a counting experiment on the $\not\!\!E_T$ spectrum, we choose a set of cuts on one variable, $\not\!\!E_T$. Having defined the variables of interest, we now devise a measure[1] of significance. Suppose that for a given cut in $\not\!\!E_T$, the number of expected background events passing the cut is $b(\not\!\!E_T)$, then assuming Poisson statistics for the background we have:

$$P\left(k,\, b(\not\!\!E_T)\right) \;=\; \frac{e^{-b}\cdot b^k}{k!}\,, \tag{8.1}$$

where k is the number of data events passing the $\not\!\!E_T$ cut. Suppose also that the number of the expected signal events passing the $\not\!\!E_T$ cut is $s(\Lambda, \not\!\!E_T)$ (which also depends on the Λ), and $\Lambda^{95\%}$ is the 95% confidence level (C.L) limit we can set for Λ. It is obvious that $\Lambda^{95\%}$ must depend on the expected background and signal event counts and also on the background fluctuation k; therefore in general we have:

$$\Lambda^{95\%} \;=\; \Lambda^{95\%}\big(k,\, b(\not\!\!E_T),\, s(\Lambda, \not\!\!E_T)\big)\,. \tag{8.2}$$

Since the above value of $\Lambda^{95\%}$ depends on the number k (background fluctuation), we can account for all possible values of k by simply taking the average of Eq. 8.2 using the probability defined in Eq. 8.1 and take the result as a measure of the significance associated with the chosen $\not\!\!E_T$ cut:

$$S(\Lambda, \not\!\!E_T) = \left\langle \Lambda^{95\%} \right\rangle = \sum_{k=0}^{\infty} P\left(k,\, b(\not\!\!E_T)\right) \Lambda^{95\%}\big(k,\, b(\not\!\!E_T),\, s(\Lambda, \not\!\!E_T)\big)\,. \tag{8.3}$$

[1]The term "measure" is used here loosely, and not with it's mathematical meaning. Significance is not a measure function in the formal mathematical sense.

Using the above expression we calculate [98] the significance $S(\Lambda, \not\!\!E_T)$ for a chosen $\not\!\!E_T$ cut, which is shown in Figure 8.1 for the SUSY point 20 of Table 6.1. As can be seen from the figure, the

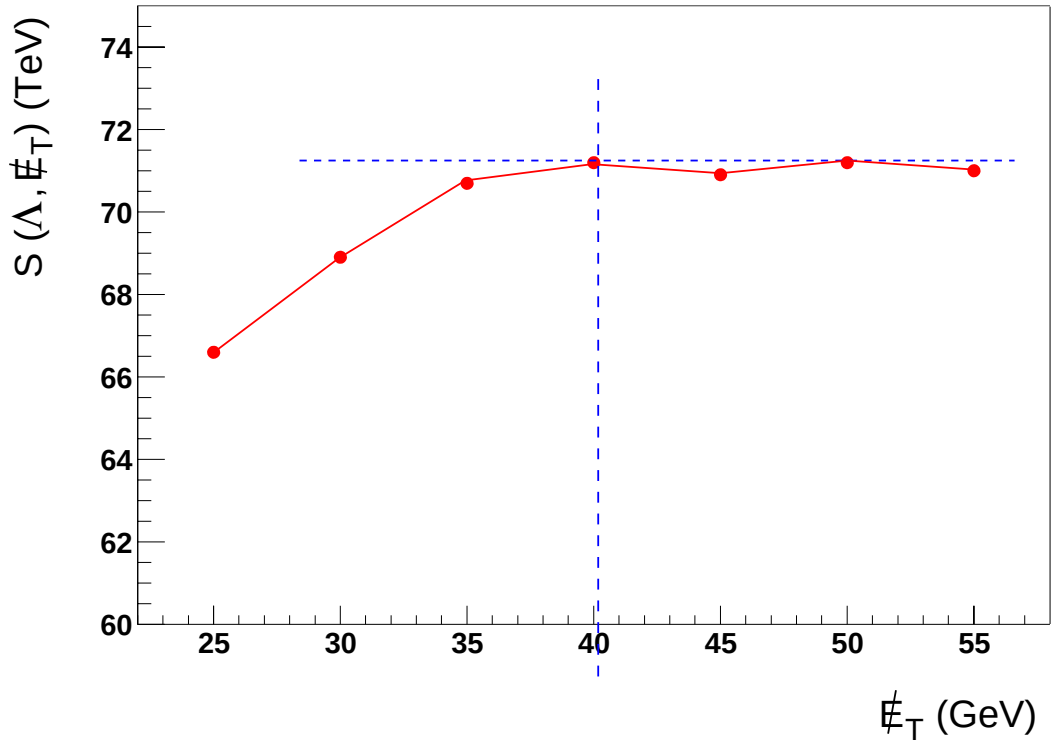

Figure 8.1: Expected limit on Λ vs. cut on $\not\!\!E_T$.

significance is leveling off at a certain value of $\not\!\!E_T$; this value is then chosen as the "optimal" cut for $\not\!\!E_T$. This process is repeated for all SUSY points of interest (values of Λ), and the minimum of the optimal cuts in $\not\!\!E_T$ can be chosen. This optimal cut was determined to be at $\not\!\!E_T = 40$ GeV, independent of the SUSY point.

8.2 Limits Setting

Having set the optimal cut on $\not\!\!E_T$ to be used in this analysis, we proceed with setting limits for the masses of the model in study. In DØ there is an accepted procedure for setting limits based on Bayesian approach [100, 101]. In this section we briefly outline the idea of this method.

8.2.1 Bayes' Theorem

Bayes' theorem [102], is essentially an application of the conditional probabilities formula that states:

$$P(\mathcal{A}\ and\ \mathcal{B}) \;=\; P(\mathcal{A} \mid \mathcal{B}) \cdot P(\mathcal{B}), \tag{8.4}$$

where $\mathcal{A}$ and $\mathcal{B}$ are two stochastic variables of our sample space, $P(\mathcal{B})$ is the probability for the variable $\mathcal{B}$ to occur, and $P(\mathcal{A} \mid \mathcal{B})$ is the *conditional* probability for the variable $\mathcal{A}$ to occur given that $\mathcal{B}$ already occurs. Since there is no distinction between variables $\mathcal{A}$ and $\mathcal{B}$ the above expression can be re-stated as:

$$P(\mathcal{A}\ and\ \mathcal{B}) \;=\; P(\mathcal{B} \mid \mathcal{A}) \cdot P(\mathcal{A}), \tag{8.5}$$

Bayes' theorem follows from 8.4 and 8.5 by equating the right-hand sides:

$$P(\mathcal{A} \mid \mathcal{B}) \;=\; P(\mathcal{B} \mid \mathcal{A}) \cdot \frac{P(\mathcal{A})}{P(\mathcal{B})}. \tag{8.6}$$

Equation 8.6, strictly proven in the context of *Probability Theory*, is extended as the definition of *Subjective Probability* in the context of *Bayesian Statistics*, by applying it also in statements described as "un-scientific" in the frequentist approach. For example, given the fact that usually the evolution on both Theory and Experiment are tightly intertwined, the above expression is used as a means to experimentally check proposed theories:

$$P(Theory \mid Result) \;=\; P(Result \mid Theory)\frac{P(Theory)}{P(Result)}. \tag{8.7}$$

In the following, Bayes theorem will be used in the context of subjective probability, on other words Eq. 8.7 will be used.

8.2.2 Limits Calculation

For counting experiments (as is the case of new particle searches), given the signal cross section σ, the signal efficiency ϵ, the total integrated luminosity $\mathcal{L}$ and the number of the expected background events b (for the optimal $\not\!\!E_T$ chosen cut), we can determine the probability of observing k events as:

$$P\left(k \,|\, b, \epsilon, \sigma, \mathcal{L}\right) \;=\; \frac{e^{-(b+\epsilon\sigma\mathcal{L})}(b+\epsilon\sigma\mathcal{L})^{k}}{k!}\,. \tag{8.8}$$

The above expression corresponds to the term $P\left(Result \,|\, Theory\right)$ on the right-hand side of Eq. 8.7. What we are interested in for an experiment is the left-hand side of Eq. 8.7, and in order to find that, we have to assign the remaining probabilities of the expression (*prior probabilities*). Although in general these probabilities can be correlated, we usually ignore the correlation of the signal cross section σ with the others, and therefore factorize the prior into a product of independent priors:

$$P\left(Theory\right) \;\propto\; P\left(\sigma\right)P\left(b, \epsilon, \mathcal{L}\right), \tag{8.9}$$

where the factorization is done up to a multiplicative constant. Using Eq. 8.7, 8.8, and 8.9 we get:

$$P\left(b, \epsilon, \sigma, \mathcal{L} \,|\, k\right) \;\propto\; \frac{e^{-(b+\epsilon\sigma\mathcal{L})}\cdot(b+\epsilon\sigma\mathcal{L})^{k}}{k!}P\left(\sigma\right)P\left(b, \epsilon, \mathcal{L}\right), \tag{8.10}$$

where the multiplicative constant is determined by normalizing the above probability. The above expression can be written in the form of probability densities:

$$\rho\left(b, \epsilon, \sigma, \mathcal{L} \,|\, k\right) \;\propto\; \frac{e^{-(b+\epsilon\sigma\mathcal{L})}\cdot(b+\epsilon\sigma\mathcal{L})^{k}}{k!}\rho\left(\sigma\right)\rho\left(b, \epsilon, \mathcal{L}\right). \tag{8.11}$$

In order to set limits we are interested in the conditional probability density of σ given that we observe k events, $\rho\left(\sigma \,|\, k\right)$, therefore we remove the other parameters by integrating over them:

$$\rho\left(\sigma \,|\, k\right) \;=\; \int_0^\infty d\mathcal{L}\int_0^1 d\epsilon\int_0^\infty db\rho\left(b, \epsilon, \sigma, \mathcal{L} \,|\, k\right). \tag{8.12}$$

These parameters are often called *nuisance parameters*. Using this expression we set an upper limit on the cross section specified at some level of confidence, in this analysis this C.L is 95%:

$$0.95 \;=\; \int_0^{\sigma(95\%)} d\sigma\rho\left(\sigma \,|\, k\right). \tag{8.13}$$

It has to be noted here that the above calculation has to be repeated for every value Λ of the model (and for the optimal $\not\!\!E_T$ cut), so that the dependence $\sigma^{95\%}(\Lambda)$ will be deduced. The limit on Λ (and therefore the masses of the particles) is then easily set by the requirement:

$$\sigma^{95\%}(\Lambda) \;=\; \sigma^{Theory}(\Lambda). \tag{8.14}$$

Using the above described method, limits found and are shown in Table 6.1 and in Figures 8.2, 8.3, and 8.4 for this Snowmass model line E and the two other model lines.

For the Snowmass model line E, the limit is $\Lambda > 79.6$ TeV at 95% C.L., or in terms of gaugino masses, $m_{\chi_1^0} > 107.7$ GeV and $m_{\chi_1^+} > 194.9$ GeV. The chargino mass limit for the model line with $N_5 = 1$ and $tan\beta = 5$ is 191.6 GeV, and for the model line with $N_5 = 2$ and $tan\beta = 5$ is 196.0 GeV.

These are the most restrictive limits on this class of GMSB models today. The results have been accepted for publication in the Phys. Rev. Lett.

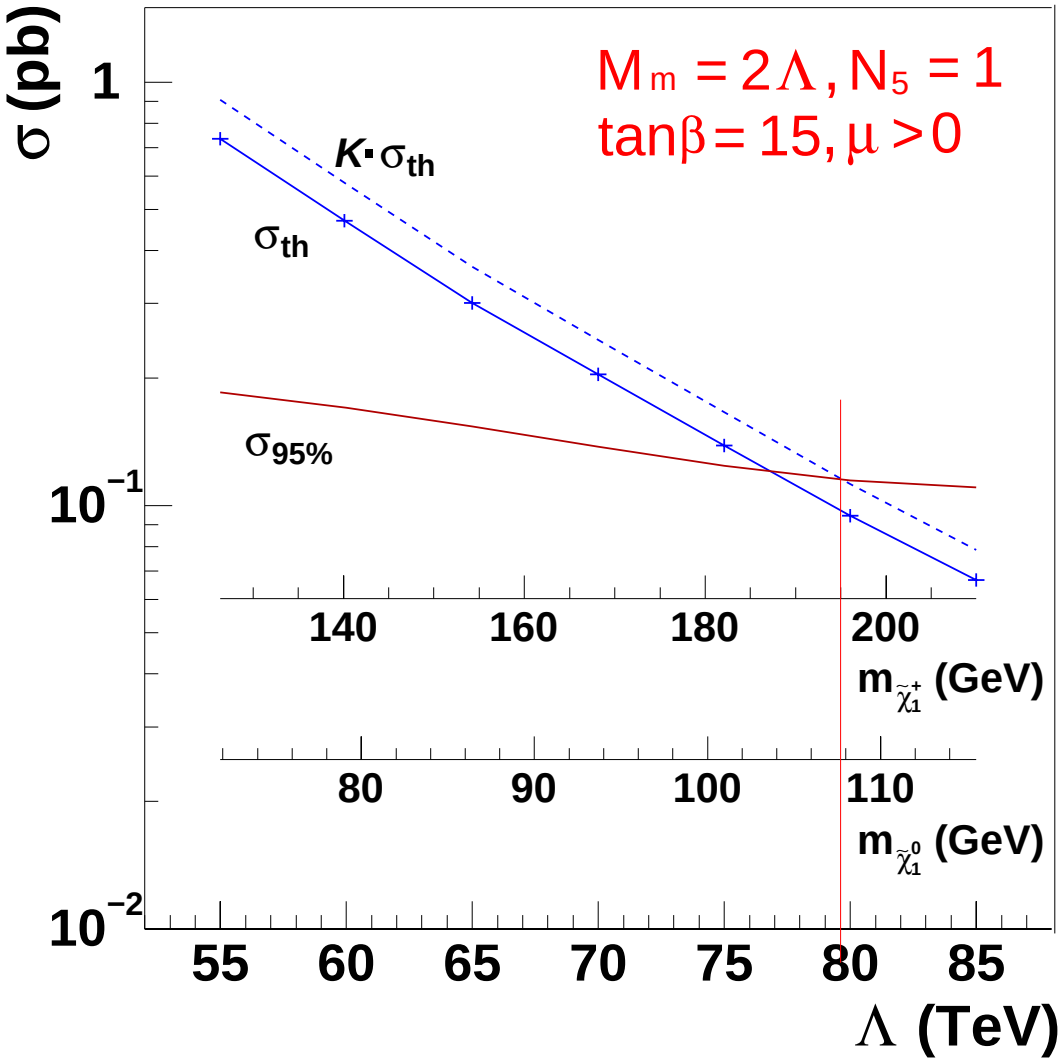

Figure 8.2: Snowmass model line E cross section vs. Λ in LO (blue solid line), multiplied by K-factor (blue dashed line) and the 95% C.L. limits (brown solid line).

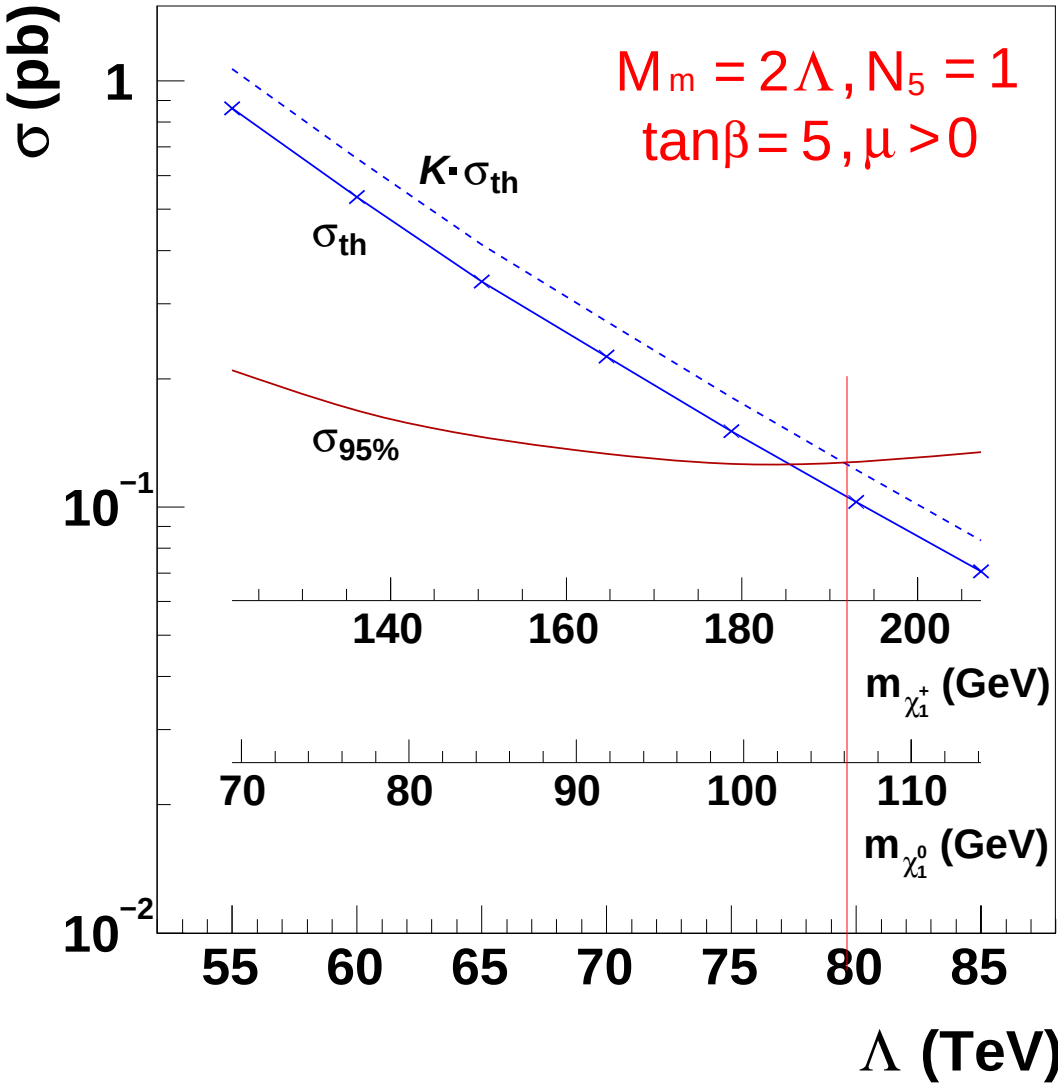

Figure 8.3: GMSB SUSY cross section vs. Λ in LO (blue solid line), multiplied by K-factor (blue dashed line) and the 95% C.L. limits (brown solid line).

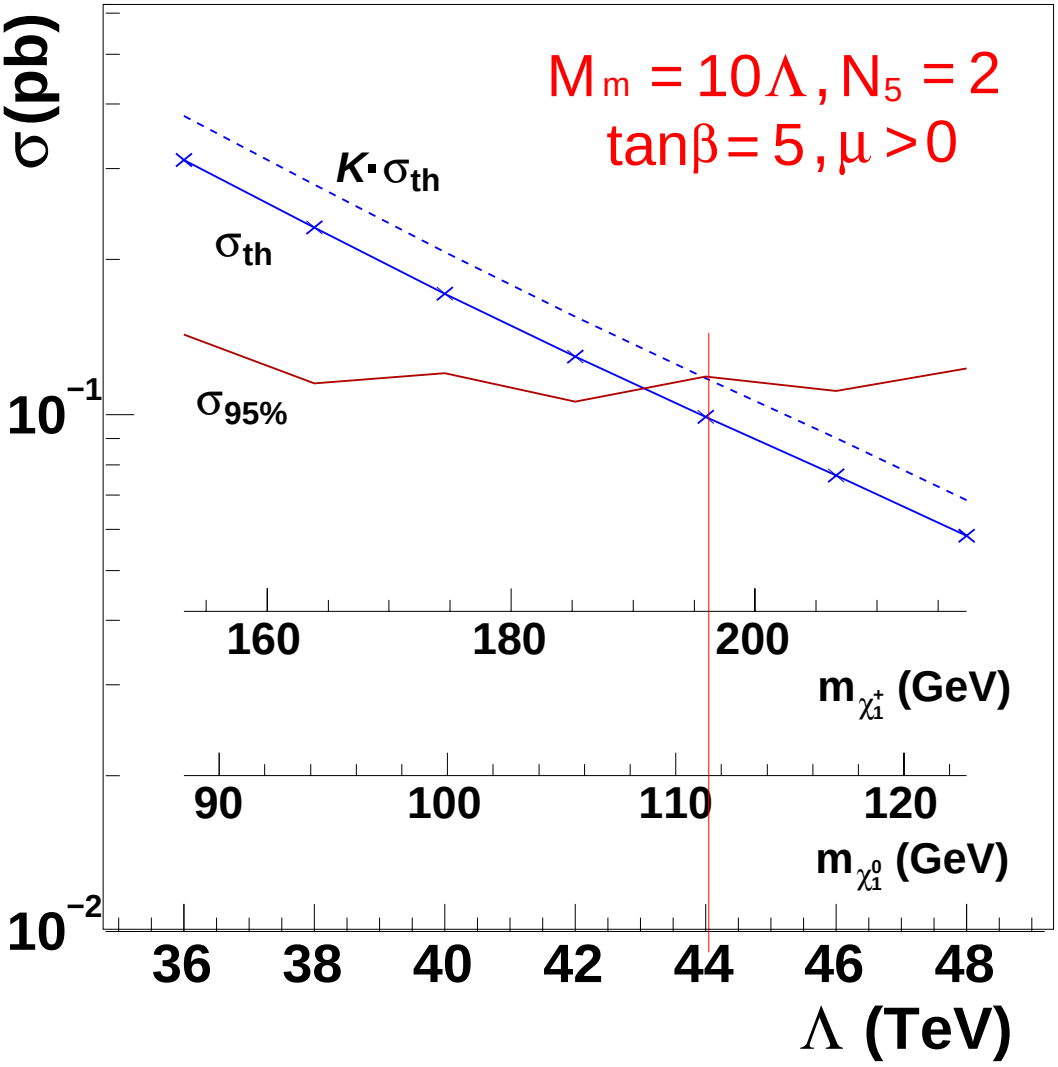

Figure 8.4: GMSB SUSY cross section vs. Λ in LO (blue solid line), multiplied by K-factor (blue dashed line) and the 95% C.L. limits (brown solid line).

Chapter 9

Conclusions

This thesis describes the search for GMSB SUSY in the di-photon and large missing transverse energy channel, with 263 pb^{-1} of data collected by the DØ Experiment at the Fermilab Tevatron Collider, between April 2002 and March 2004.

No excess of events above the Standard Model background prediction is found, for all $\not\!\!E_T$ explored. From the observed number of events, lower limits (for the Snowmass model line E) have been set at the 95% C.L. for masses of the lightest neutralino and chargino. The results of this analysis set a lower limit of 107.7 GeV for the neutralino mass and 194.9 GeV for the chargino mass, which currently are the most stringent limits for this class of models.

Bibliography

[1] S.L Glashow, Nucl. Phys. **22** 579 (1961);

S. Weinberg, Phys. Rev. Lett. **19** 1264 (1967);

A. Salam, *Elementary Particle Theory*, ed. N. Svartholm (Almquist and Wiksells, Stockholm, 1969) p.367.

[2] G. Arnison *et al.*, (UA1 Collaboration), Phys. Lett. **B126** 398 (1983);

Phys. Lett. **B129** 273 (1983);

[3] P. Bagnaia *et al.*, (UA2 Collaboration), Phys. Lett. **B129** 310 (1983);

Z. Phys. **C24** 1 (1984).

[4] G. Landsberg, Ph.D Thesis, SUNY at Stony Brook, (1994) (Unpublished).

[5] B. Abachi *et al.* (DØ Collaboration), Phys. Rev. Lett. **74** 2632 (1995).

[6] F.Abe *et al.* (CDF Collaboration), Phys. Rev. **74**, 2626 (1995).

[7] R. Genik II, Ph.D Thesis, Michigan State University (1998) (Unpublished).

[8] M. Kaku, *Quantum Field Theory*, Oxford University Press, 1993.

[9] P.W. Higgs, Phys. Rev. Lett. **12** 508 (1964);

Phys Rev. **145** 1156 (1966);

F. Englert and R. Brout, Phys. Rev. Lett. **13** 321 (1964);

G.S. Guralnik, C.R. Hagen, and T.W.B. Kibble, Phys. Rev. Lett. **13** 585 (1964);
T.W.B. Kibble, Phys. Rev. **155** 1554 (1967).

[10] V.D. Barger and R.J.N. Phillips, *Collider Physics*, Addison-Wesley, 1988.

[11] G. Kane, *Modern Elementary Particle Physics*, Updated Edition, Perseus Books, Reading Massachusetts, 1993, p.100.

[12] S. Dawson, hep-ph/9612229, 1997.

[13] J. Wess and J. Bagger, *Supersymmetry and Supergravity*, (Princeton University Press, Princeton, N.J. 1983);
P. Fayet and S. Ferrara Phys. Rep. **32** 249 (1977).

[14] Steven Weinberg, *The Quantum Theory of Fields, Volume III: Supersymmetry*, Cambridge University Press, 2000.

[15] P. Fayet, Phys. Lett. **69B**, 489 (1977); G. Farrar and P. Fayet, Phys. Lett. **76B**, 575 (1978).

[16] J. Ellis et al., Nucl. Phys. **B238**, 453 (1984).

[17] G.F. Giudice, and R. Rattazzi, Phys. Reports **322**, 419 (1999).

[18] For a review and guide to the literature, see J.F. Gunion and H.E. Haber, in Perspectives on Supersymmetry, ed. G.L. Kane (World Scientific, Singapore, 1998) pp.235-255.

[19] http://www.totse.com/en/fringe/fringe_science/tevatron.html

[20] B. Abachi *et al.*, (DØ Collaboration), Nucl. Instr. and Methods **A338** 185 (1994).

[21] Design Report, The DØ Experiment at the Fermilab $\bar{p}p$ Collider, November 1984.

[22] Abid M. Patwa, Ph.D. Thesis, SUNY at Stony Brook (2002) (Unpublished).

[23] A.R. Baden, *Jets and Kinematics in Hadronic Collisions*, January 1997

[24] J. Ellison, For the DØ Collaboration, The DØ Detector Upgrade and Physics Program, hep-ex/0101048, 2001.

[25] http://www-d0.fnal.gov/runcoor/DAQ/Tutorials/2003/2003-02-18_Kajfasz_SMT-01.ppt, http://www-d0.fnal.gov/runcoor/DAQ/Tutorials/2003/2003-02-18_Kajfasz_SMT-02.ppt

[26] *DØ Silicon Tracker Technical Design Report*, DØ Note 2169.

[27] *The DØ Upgrade. The Detector and Its Physics*, the DØ Collaboration, July 30, 1996.

[28] *Silicon Detector*, talk by R. Lipton at Fermilab Lecture Series.

[29] DØ Collaboration, Calorimeter Electronics Upgrade for Run2, Technical Design Report, V1.7, May 6, 1998; http://www-d0.fnal.gov/~d0upgrade/calelec/intro/tdr/tdr17.pdf

[30] Stilianos Kesisoglou, Talk at the DPF2000 Conf. on New Detector Technologies (for the DØ Collaboration), Columbus OH, August 9-12, 2000. http://www.physics.ohio-state.edu/dpf2000/Dpftalks/Detector/kesisoglou_16.ps.gz

[31] Stilianos Kesisoglou, Proceedings of the DPF2000 Conf. on New Detector Technologies, Columbus OH, August 9-12, 2000. International Journal of Modern Physics A, *Vol. 16*, No. supp01C (2001) 1087-1090 (World Scientific). http://www.physics.ohio-state.edu/dpf2000/Dpfpapers/Detector/kesisoglou_16.ps.gz

[32] S.Choi, W.Cooper, F.Fast, Yu.Gershtein, H.Jostlein, E.Kajfasz, S.Kesisoglou, G.Landsberg, A.Melnitchouk, *SMT Barrel Assembly*, DØ Internal note 3849.

[33] http://hep.brown.edu/users/SiDet/welcome.html

[34] D. Adams *et al.*, Fermilab-Conf-94/318-E, presented at DPF'94

[35] M. Adams *et al.*, *Design Report of the Central Preshower Detector for the DØ Upgrade*, DØ note 3014.

[36] R. Fruhwirth *et al.*, it Data Analysis Techniques for High-Energy Physics , second edition (Cambridge University Press, 2000) pp.185, 186, 188, 192, 194-210.

[37] W. Guryn, Proceedings of the Second International Conf. on Calorimetry in High Energy Physics, Capri, Italy, October 14-18, 1991.

[38] Manufacturing Sciences Corp., Oak Ridge, TN.

[39] Brian Lauer,Ph.D Thesis, Iowa State University (1997) (Unpublished).

[40] P. Demine, Ph.D. Thesis, Universite Joseph Fourier - Grenoble 1 - U.F.R. de Physique, (2002) (Unpublished).

[41] S.J. Wimpenny *et al., Nucl. Instrum. Methods,* **A279**, 107-113 (1989)

[42] P. Franzini *et al., Nucl. Instrum. Methods,* **A289**, 438-445 (1990)

[43] A.L. Spadafora *et al., Nucl. Instrum. Methods,* **A315**, 279-284 (1992)

[44] H. Aihara *et al., IEEE Trans. Nucl. Sci.,* **38**(2), 398-402 (1991)

[45] http://www-d0.fnal.gov/runcoor/DAQ/2003-01-24_Begel_Luminosity.ps

[46] C.-C.Miao, R.Partridge, Study of the Run II Luminosity Monitor Counter Design, DØ Internal Note 3319, 1998.

[47] A.Lo,C.-C.Miao, R.Partridge, Luminosity Monitor Technical Design Report, DØ Internal Note 3320, 1997.

[48] C.-C.Miao, the DØ Run II Luminosity Monitor, Nucl. Phys. Proc. Suppl., **78**, 342-347 (1999).

[49] http://www-bdnew.fnal.gov/operations/lum/lum.html

[50] A. Brandt *et al.*, *A Forward Proton Detector at DØ*, FERMILAB-Pub-97/377, 1997.

[51] Michele Petteni, Ph.D Thesis, Imperial College, London, (2003).

[52] http://d0.phys.washington.edu/~haas/d0/l3/sci2002.pdf

[53] http://www-d0.fnal.gov/runcoor/DAQ/Tutorials/2003/2003-01-27_Chapin_L3DAQ.pdf

[54] Review of Particle Physics, Part 1, PDG, Phys. Rev. **D66** 010001-98, 010001-89, 010001-271 (2002).

[55] S. Eidelman *et al.,* Phys. Lett. B **592**, p.167 (2004)

[56] S. Eidelman *et al.,* Phys. Lett. B **592**, pp.170-171 (2004)

[57] H. Weidkamp, DiplomArbeit, Rhein-Westf Tech. Hochschule Aachen (1984).

[58] G. Bernardi, B. Olivier, B. Knuteson, M.Strovink, *NADA: A New Event by Event Hot Cell Killer*, DØ Note 3687, 1999.

[59] S.Protopopescu, *EMReco Algorithms*
http://www-d0.fnal.gov/d0dist/dist/releases/p14.06.01/emreco/doc/emreco_classes.ps

[60] Laurent Duflot and Melissa Ridel, *The CellNN algorithm: cell level clustering in the D0 calorimeter*, DØ Note 3923, 2001.

[61] F. Beaudette and J.-F. Grivaz, *The Road Method (an algorithm for the identification of electrons in jets)*, DØ Note 3976, 2002.

[62] http://www-d0.fnal.gov/Run2Physics/cs/d0correct/d0correct.html

[63] http://www-d0.fnal.gov/Run2Physics/cs/index.html

[64] S. Crépé-Renaudin, *Energy corrections for geometry effects for electrons in Run II*, Internal Note 4023 (2002).

[65] J. Womersley, EM Calorimeter Calibration for the DØ Upgrade, DØ Internal Note 2377.

[66] S. Abachi et al.(DØ Collaboration) Phys. Rev. Lett. 78, 3640 (1997); B. Abbott et al.(DØ Collaboration), Phys. Rev. D 57, 3817 (1998).

[67] B. Abbott et al.(DØ Collaboration), Phys. Rev. Let. 81, 524 (1998).

[68] D. Cutts, G. Landsberg, Contribution to the BTMSSM Working Group of the Run II SUSY/Higgs Workshop at Fermilab, [arXiv:hep-ph/9904396]

[69] G. Landsberg, *EMVTX package*, DØ Note in preparation.

[70] D.Soper *et al.*, Recommendation from Les Houches 1999 Jet Definition Group. Letter to J.Blazey; http://niuhep.physics.niu.edu/blazey/jet_alg/les_houches.ps

[71] B.Abbott *et al.*, Fixed Cone Jet Definitions in DØ and R_{sep}, FERMILAB-Pub-97/242-E.

[72] http://www-d0.fnal.gov/phys_id/jes/d0_private/jes.html

[73] http://www-d0.fnal.gov/Run2Physics/cs/d0correct/d0correct.html

[74] Jets and $\not\!\!E_T$ ID Group
http://www-d0.fnal.gov/~d0upgrade/d0_private/software/jetid/jetid.html

[75] Adams D., *Finding Tracks*, DØ Note 2958, 1996

[76] Ariel Schwartzman, Meenakshi Narian, *Vertex Fitting by means of the Kalman Filter techinque*, DØ Note 3907, 2001.

[77] B. Knuteson, M. Strovink, B. Olivier, U. Bassler, F. Fleuret, G. Bernardi, *The missing transverse energy resolution of an event*, DØ Note 3629, 1999.

[78] Bruce Knuteson, Mark Strovink, *The missing transverse energy resolution of an event*, DØ Note 3629, 1999.

[79] Bruce Knuteson, Mark Strovink, *The missing transverse energy resolution of an event*, DØ Note 4254, 2003.

[80] http://www-d0.fnal.gov/phys_id/luminosity/data_access/

[81] http://www-d0.fnal.gov/phys_id/luminosity/data_access/lm_access/doc/

[82] EM ID Certification Results
http://www-d0.fnal.gov/phys_id/emid/d0_private/certification/welcome.html

[83] http://www.thep.lu.se/tf2/staff/torbjorn/Pythia.html

[84] http://www.phy.bnl.gov/~isajet/

[85] T. Sjostrand, L. Lonnblad and S. Mrenna, *PYTHIA 6.2: Physics and manual,* arXiv:hep-ph/0108264.

[86] J. Botts, J. G. Morfin, J. F. Owens, J. w. Qiu, W. K. Tung and H. Weerts [CTEQ Collaboration], *CTEQ parton distributions and flavor dependence of sea quarks,* Phys. Lett. B **304**, 159 (1993) [arXiv:hep-ph/9303255].

[87] J. Pumplin, D. R. Stump, J. Huston, H. L. Lai, P. Nadolsky and W. K. Tung, *New generation of parton distributions with uncertainties from global QCD analysis,* JHEP **0207**, 012 (2002) [arXiv:hep-ph/0201195].

[88] http://cteq.org

[89] http://www-d0.fnal.gov/computing/MonteCarlo/generator_tools/susy_tools.html

[90] Y. Fisyak, J. Womersley, DØ GEANT Simulation of the Total Apparatus Response, DØ Internal Note 3191, 1997.

[91] GEANT - Detector Description and Simulation Tool, CERN, Geneva, 1993.

[92] http://www-d0.fnal.gov/computing/MonteCarlo/simulation/d0sim.html

[93] http://www-d0.fnal.gov/computing/trigsim/trigsim.html

[94] http://zippy.physics.niu.edu/modellines.html ;

[95] http://zippy.physics.niu.edu/modellineE.html

[96] Beenakker *et. al.* , hep-ph 9906298

[97] Yurii Maravin: Photon ID Studies. D0 Note in preparation.

[98] Bruce Knuteson, *Algorithms for Computing Significance*, DØ Note 3345, 1997.

[99] James T. Linnemann, *Measures of Significance in HEP and Astrophysics*, PHYSTAT2003, SLAC, Stanford, California, September 8-11, 2003.

[100] I. Bertram, G.Landsberg, J.Linnemann, R.Partridge, M.Paterno, H.B.Prosper, *A Recipe for the Construction of Confidence Limits*, DØ note 3476, 1999.

[101] J. Linnemann, M. Paterno and H.B. Prosper *Calculating Confidence Limits*, DØ note 4491, 2004.

[102] Bayes, T. 1764. *An Essay Toward Solving a Problem in the Doctrine of Chances*, Philosophical Transactions of the Royal Society of London **53**, 370-418